Fabrication and Optical Characterization of Metamaterials and Nano-Antennas

Von der Fakultät für Mathematik und Physik der Universität Stuttgart
zur Erlangung der Würde eines Doktors der
der Naturwissenschaften (Dr. rer. nat.)genehmigte Abhandlung

vorgelegt von
Hongcang Guo
aus Hebei, V. R. China

Hauptberichter:	Prof. Dr. Harald Giessen
Mitberichter:	Prof. Dr. Martin Dressel
Tag der mündlichen Prüfung:	3. September 2008

4. Physikalisches Institut der Universität Stuttgart
2008

Zusammenfassung

In dieser Arbeit wurden die optischen Eigenschaften von Metamaterialien und optischen Nano-Antennen untersucht. Die Proben wurden durch Elektronenstrahllithographie und anschließendes Trockenätzen hergestellt. Die lineare Transmission und Reflektion wurden mit einem Fouriertransformations-IR-Spektrometer gemessen. Außerdem wurden numerische Simulationen mit der Methode der Finiten Integration durchgeführt.

Split-Ring-Resonatoren (SRR) sind vielversprechende Bauelemente für Metamaterialien mit negativer Permeabilität. Durch experimentelle und numerische Untersuchung der Schichtdicken abhängigkeit der optischen Resonanzen von SRR-Metamaterialien konnten wir zeigen, dass das Plasmonen-Modell die Resonanz eines SRRs im optischen Spektralbereich wiedergibt. Wir haben gezeigt, dass die Resonanz eines SRR durch die eines Nanodraht mit äquivalenter Gesamtlänge gut beschrieben wird. Außerdem liefert das Plasmonen-modell in Kombination mit dem Konzept der Hybridisierung ein einfaches Modell für das Verständnis der optischen Eigenschaften gekoppelter Systeme, wie z.B. Doppel-Split-Ring-Resonatoren.

Optische Nano-Antennen stellen ein interessantes optisches System dar, da sie im Bereich ihrer Resonanz das elektrische Lichtfeld sehr stark verstärken und die Lichtenergie in einem sehr kleinen Raumbereich eingeschlossen wird. In dieser Arbeit werden die optischen Eigenschaften einer Slot-Antenne untersucht, wobei die Bowtie-Slot-Antenne als repräsentatives Design gewählt wird. Periodische Anordnungen von Bowtie-Slot-Antennen in einem dünnen Metallfilm konnten experimentell hergestellt und charakterisiert werden. Die Abhängigkeit der Resonanzeigenschaften von der geometrischen Form der Antenne konnten anhand numerischer Simulationen untersucht werden. Dabei kann man im optischen und infraroten Spektralbereich zwei Resonanzen unterscheiden, die sich im Hinblick auf die Abhängigkeit von der Antennengeometrie komplementär verhalten. Darüberhinaus wurde die Materialabhängigkeit der Resonanzen von Bowtie-Slot-Antennen untersucht.

Abstract

In this thesis, we have investigated the optical properties of metamaterials and optical nano-antennas. The structures were fabricated with electron beam lithography and subsequent dry etching process. The linear transmission and reflection of these structures were measured with an Fourier transform infrared spectrometer. We also performed numerical simulations with a finite integration time domain algorithm.

Split-ring resonators (SRRs) are promising building blocks for negative permeability metamaterials. By investigating the thickness dependence of the optical resonances of split-ring resonator metamaterials experimentally and numerically, we have demonstrated that the plasmonic model describes well the resonance behavior of SRRS in the optical regime. We have shown that the resonance of an SRR can be described by that of a cut-wire with an equivalent total length. We have also shown that combining with the hybridization concept, the plasmonic model offers a simple picture to understand the optical properties of coupled system such as double SRRs.

Optical nano-antennas have attracted a great deal of attention due to their strong field enhancement and field confinement at resonance. In this thesis, we have investigated the optical properties of slot antennas using the bowtie slot antenna as a representative design. We demonstrated experimental results of bowtie slot antenna arrays in a thin metal film. Assisted by the numerical simulation tools, the resonance properties of bowtie slot antennas have been discussed in the framework of geometry dependence. We showed that two distinct types of resonances can be supported by bowtie slot antennas in the near infrared and visible spectral range, and they show a complementary behavior with respect to geometry dependence. We also investigated the effect of metal properties on the resonances of bowtie slot antennas.

Publications

Part of this work have been published in the scientific journals or presented in the international conferences:

- H. C. Guo, T. Meyrath, T. Zentgraf, N. Liu, L. Fu, H. Schweizer, and H. Giessen, *Optical resonances of bowtie slot antennas and their geometry and material dependence,* Optics Express, **16,** 7756 (2008).
- H. C. Guo, N. Liu, L. Fu, T. P. Meyrath, T. Zentgraf, H. Schweizer, and H. Giessen, *Resonance hybridization in double split-ring resonator metamaterials,* Optics Express, **15,** 12095 (2007).
- H. C. Guo, N. Liu, L. Fu, H. Schweizer, S. Kaiser, and H. Giessen, *Thickness dependence of the optical properties of split-ring resonator metamaterials,* Phys. stat. sol. (b) **244,** 1256 (2007).
- H. C. Guo, T. Zentgraf, T. Meyrath, N. Liu, L. Fu, H. Schweizer, and H. Giessen, *Two Distinct Types of Resonances in Optical Bowtie Slot Nanoantennas,* CLEO/QELS 2008 in San Jose, California (USA).
- H. C. Guo, N. Liu, T. Zentgraf, T. Meyrath, L. Fu, H. Schweizer, and H. Giessen, *Optical properties of bowtie slot antennas,* First International Congress on Advanced Electromagnetic Materials in Microwaves and Optics 2007, Rome (Italy).

Additional scientific publications which are not presented in this thesis:

- H. C. Guo, D. Nau, A. Radke, X. P. Zhang, J. Stodolka, X. L. Yang, S. G. Tikhodeev, N. A. Gippius, and H. Giessen, *Large-area metallic photonic crystal fabrication with interference lithography and dry etching*, Appl. Phys. B **81,** 271 (2005).
- X. P. Zhang, B. Sun, R. H. Friend, H. C. Guo, D. Nau, and H. Giessen, *Metallic photonic crystals based on solution-processible gold nanoparticles,* Nano Lett. **6,** 651 (2006).

- X. P. Zhang, B. Sun, H. C. Guo, N. Tetreault, H. Giessen, and R. H. Friend, *Large-area two-dimensional photonic crystals of metallic nanocylinders based on colloidal gold nanoparticles,* Appl. Phys. Lett. **90,** 133114 (2007).
- H. Schweizer, L. Fu, H. Graebeldinger, H. C. Guo, N. Liu, S. Kaiser, and H. Giessen, *Longitudinal capacitance design for optical left-handed metamaterials*, Phys. stat. sol. (b) **244,** 1243 (2007).
- N. Liu, H. C. Guo, L. Fu, H. Schweizer, S. Kaiser, and H. Giessen, *Electromagnetic resonances in single and double split-ring resonator metamaterials in the near infrared,* Phys. stat. sol. (b) **244,** 1251 (2007).
- L. Fu, H. Schweizer, H. C. Guo, N. Liu, and H. Giessen, *Analysis of metamaterials using transmission line models,* Appl. Phys. B **86,** 425 (2007).
- N. Liu, H. C. Guo, L. Fu, S. Kaiser, H. Schweizer, and H. Giessen, *Realization of three-dimensional photonic metamaterials at optical frequencies,* Nature Mater. **7,** 31 (2008).
- N. Liu, H. C. Guo, L. Fu, H. Schweizer, S. Kaiser, and H. Giessen, *Plasmon hybridization in stacked cut-wire metamaterials,* Advanced Materials, **19,** 3628 (2007).
- X. Zhang, B. Sun, H. C. Guo, and H. Giessen, *Self-assembly of gold nanoparticles through annealing in the fabrication of square lattices of nanocylinders,* OSA topical conference on nanophotonics 2007, Zhejiang (China).
- N. Liu, H. C. Guo, L. Fu, H. Schweizer, H. Giessen, *Stacking of split-ring resonator metamaterials in the optical regime,* First International Congress on Advanced Electromagnetic Materials in Microwaves and Optics 2007, Rome (Italy).
- H. Giessen, T. Zentgraf, N. Liu, H. C. Guo, H. Schweizer, T. P. Meyrath, and L. Fu, *Coupling and losses in metamaterials,* Progress in Electromagnetics Research Symposium (PIERS) 2007, Beijing (China).
- H. Giessen, T. Zentgraf, C. Rockstuhl, C. Etrich, H. C. Guo, N. Liu, T. Meyrath, H. Schweizer, S. Kaiser, J. Kuhl, and F. Lederer, *Radiative and Nonradiative Decay of Near-Infrared Excitations in Split-ring Resonator Metamaterials,*, Photonic Metamaterials: From Random to Periodic, OSA Topical Meeting 2006, Grand Bahama Island (USA).

- T. Zentgraf, C. Rockstuhl, H. C. Guo, C. Etrich, I. Loa, K. Syassen, J. Kuhl, F. Lederer, and H. Giessen, *Magnetic and Electronic Resonances for Different Meatamaterial Resonator Geometries,* QELS 2006, Long Beach (USA).

- H. Giessen, T. Zentgraf, C. Rockstuhl, C. Etrich, H. C. Guo, N. Liu, T. Meyrath, H. Schweizer, S. Kaiser, J. Kuhl, and F. Lederer, *Radiative and Non-radiative Decay of Near-Infrared Excitations in Split-Ring Resonator Metamaterials,* EOS Topical Meeting on Molecular Plasmonic Devices 2006, Engelberg (Switzerland).

- B. Winzek, V. Emelianov, A. Radke, H. C. Guo, D. Nau, and H. Giessen, *Photonic crystals with polymer waveguides for microforce detection,* SPIE International Congress on Optics and Optoelectronics 2005, Warsaw (Poland).

Contents

1 Introduction

The optical properties of metallic nano-structures have attracted tremendous research interest since the work of Mie [1] for small particles and Ritchie [2] for flat interfaces. Such structures are able to support coherent electron oscillations, commonly known as surface plasmon polaritons (SPPs), which can lead to electromagnetic field confinement on the surface of metallic structures. Much effort has been paid to study the fundamental physics of such systems [3, 4].

More recently, the development of nano-fabrication and nano-characterization techniques together with quantitative electromagnetic simulations tools has led to a resurgence of interest in this field [5]. Nano-fabrication techniques such as electron-beam lithography, focused ion beam etching, and self-assembly provide the possibility of producing optical devices on a sub-100-nm scale. Nano-characterization techniques such as dark field and near-field optical microscopy make single nano-structure and sub-wavelength resolution measurements possible. Numerical simulation tools using finite difference time domain algorithms, and finite integrate time domain algorithms, have been used to calculate the near field distributions of nano-structures illustrating their optical properties. Nowadays, SPPs attract the attention of a wide spectrum of scientists, ranging from physicists, chemists, and material scientist to biologists.

The field enhancement of metallic nano-structures has been used to manipulate light-matter interactions and enhance nonlinear phenomena. Metallic nano-particles on the sub-wavelength scale are widely used in surface-enhanced Raman spectroscopy [6]. Now even a single molecule can be detected with the assistance of the field enhancement of metallic nano-particles [7, 8]. The enhanced field associated with SPPs makes them suitable for use as sensors, and commercial systems have been already developed for sensing biomolecules [9]. Recently, it has been demonstrated that metallic nano-structures can be utilized as artificial atoms to build metamaterials with desired optical parameters [10]. By properly designing metallic structures, sub-wavelength resolution imaging has been demonstrated [11].

In this thesis, two variants of metallic nano-structures have been investigated.

One is metallic split ring resonators (SRRs), which are promising building blocks for metamaterials with negative permeability. The other is bowtie slot antennas, which show a stronger field enhancement and confinement compared with other conventionally shaped slot antennas. The fundamental physics of optical resonances for both systems has been studied, and the feasibility of potential applications has been reviewed.

Optical properties of metallic nano-particles have been intensively studied since Mie's work [1]. It indicated that the bulk properties of metals are modified when they are structured on a nanometer scale. The optical properties of metallic nano-particles strongly depend on the dielectric functions of bulk metals. In Chapter 2, we will discuss the the dielectric functions of bulk silver and gold. The free electron contribution from the Drude model and the deep level electron contribution from interband transitions will be presented. Then the surface plasmon excitation in the metal/dielectric interface and optical properties of metallic nano-particles are described. Following the overview of the enhanced transmission of nano-aperture arrays and single nano-apertures, the fundamentals of antennas and primary studies on optical antennas will be discussed.

After the experimental methods and simulation techniques presented in Chapter 3, we will address the experimental and numerical studies on SRRs in Chapter 4. SRRs were first proposed in the microwave regime to achieve magnetic response in artificial metamaterials. Much effort has been paid to shift the resonance frequency of the SRRs into the optical regime. We will show that the resonance frequency of an SRR can be shifted to a higher frequency by increasing the thickness of the metal. The equivalent cut-wire model based on plasmonic explanation is proposed to interpret our experimental observations, since the standard LC circuit model [12] indicates a thickness independence of the resonances of SRRs. Additionally, we investigate the resonance properties of double SRRs by combining a hybridization concept with the plasmonic model. Our study offers a simple and intuitive method for understanding the optical responses of coupled systems in metamaterials and provides insight for the design of specific resonance properties.

The investigations presented in Chapter 5 show a comprehensive investigation of optical properties of bowtie slot antennas. Optical antennas show a large potential for near-field scanning optical microscopy (NSOM) [13], nano-lithography [14], and manipulating the emission of single emitters [15], etc. All of these potential applications depend on two characteristics of the optical antennas: field enhancement and field confinement. The field enhancement and confinement of antennas are strongly

resonance dependent [16, 17]. We first show results from experimental investigation of the optical properties of bowtie slot antenna arrays in a thin gold film. Then the period and substrate effects on the resonances of bowtie slot antennas will be presented. Following the discussion on the geometric dependence of the resonances of bowtie slot antennas, the resonance dependence on metal properties is described. This study acts as a guide to the design and optimization of slot antennas for specific resonance frequencies and characteristics.

2 Theoretical background

This chapter will give a short overview of the linear optical properties of metallic nano-structures, especially structures composed of noble metals such as gold and silver. We will first have a discussion of bulk noble metal optical properties based on the Drude model. The properties of these metals are fundamentally important for dealing with the complex optical phenomena of metallic nano-structures. Then, the optical properties of low-dimensional metallic systems such as metallic surfaces, nano-particles, and nano-apertures will be presented. It will be shown that the dielectric constants of bulk metals play an important role for the linear optical properties of metallic nano-structures. In the final section, the fundamentals of antennas and some primary studies on optical antennas are discussed.

2.1 Optical properties of bulk metals

Metals such as aluminium, gold, and silver are characterized by a high electrical and thermal conductivity, and a high reflectivity in the visible spectral range. All of these distinct properties result from the electron configuration and the particular band structure of the metals [18]. The linear responses of metals to electromagnetic waves are described by their dielectric function $\epsilon(\omega)$, which can be written as complex expression $\epsilon(\omega) = \epsilon^{'}(\omega)+i\epsilon^{''}(\omega)$. For noble metals such as gold and silver, the valence bands are completely filled and $\epsilon(\omega)$ is mainly governed by the electron transitions within the partially filled conduction bands. However, in the energy range where interband transitions occur, the contribution of electrons from deep levels has also to be taken into account.

2.1.1 Dielectric functions of free electron metals

The dielectric functions of free-electron metals are described by the Drude-Lorentz-Sommerfeld model [4], in which the macroscopic response of the metal is determined by multiplying the effect of a single free electron to the external force by the number of electrons. The response of a free electron of mass m_e and charge e to an external

electric field $\boldsymbol{E} = \boldsymbol{E}_0 e^{i\omega t}$ is described by the following equation:

$$m_e \frac{\partial^2 r}{\partial t^2} + m_e \gamma \frac{\partial r}{\partial t} = e\boldsymbol{E}_0 e^{-i\omega t}, \tag{2.1}$$

where γ denotes the damping constant. The solution of Eq. (2.1) gives the induced dipole moment of a free electron $\boldsymbol{p} = e\boldsymbol{r}_0$ and the polarization $\boldsymbol{P} = n\boldsymbol{p}$, with n being the number of electrons per unit volume. For simplicity, we consider an isotropic medium in which $\boldsymbol{P} \parallel \boldsymbol{E}$, then the dielectric function $\epsilon(\omega)$ can be written as

$$\epsilon(\omega) = 1 + P/(\varepsilon_0 E). \tag{2.2}$$

Thus, the dielectric function of a system of n free electrons per unit volume can be expressed as

$$\epsilon = 1 - \frac{\omega_p^2}{\omega^2 + i\gamma\omega} = 1 - \frac{\omega_p^2}{\omega^2 + \gamma^2} + i\frac{\omega_p^2 \gamma}{\omega(\omega^2 + \gamma^2)}, \tag{2.3}$$

where $\omega_p = (ne^2/\varepsilon_0 m_e)^{1/2}$ is the Drude plasma frequency, γ is related to the electron mean free path l by $\gamma = \upsilon_F/l$, where υ_F is the Fermi velocity. For $\omega \gg \gamma$ as in the case of noble metals gold and silver in the near infrared and visible range, the real and imaginary part of $\epsilon(\omega)$ for free-electron metals can be simplified as

$$\epsilon^{'}(\omega) = 1 - \frac{\omega_p^2}{\omega^2},\ \epsilon^{''}(\omega) = \frac{\omega_p^2}{\omega^3}\gamma, \tag{2.4}$$

It is common to express the dielectric function $\epsilon(\omega)$ in term of susceptibility χ as $\epsilon(\omega) = 1 + \chi(\omega)$. For free electron metals in the Drude-Sommerfeld model, the susceptibility is denoted as

$$\chi_{DS} = -\frac{\omega_p^2}{\omega^2 + i\gamma\omega}. \tag{2.5}$$

Figure 2.1 shows the experimental dielectric function real part $\epsilon^{'}(\omega)$ and imaginary part $\epsilon^{''}(\omega)$ for solid gold and silver [19]. The Drude-Sommerfeld model has been used to fit the experimental values with free parameters $\hbar\omega_p = 8.6$ eV and $\hbar\gamma = 0.08$ eV for gold and $\hbar\omega_p = 9.2$ eV and $\hbar\gamma = 0.016$ eV for silver, respectively. Qualitatively a good agreement between experiment and theory is obtained for energies below about 2.0 eV for gold and 3.9 eV for silver, where $\epsilon(\omega)$ is mainly dominated by free electron behavior. Above these energies, $\epsilon(\omega)$ is governed by interband transitions due to the deep level electrons, and the Drude-Sommerfeld model is no longer valid.

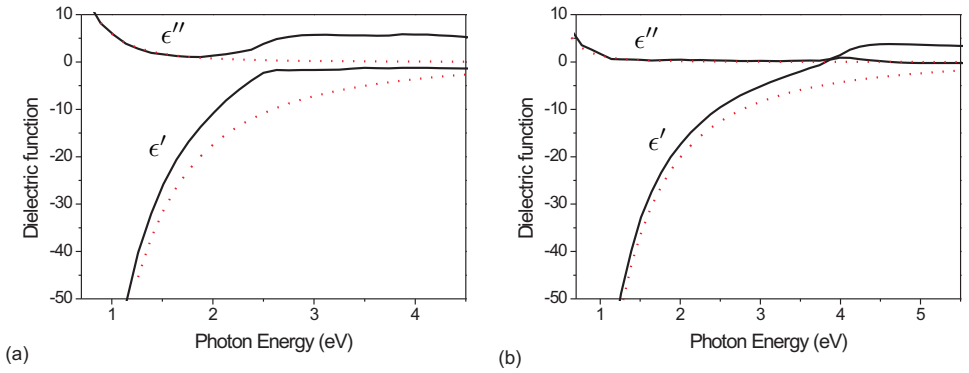

Figure 2.1: Dielectric functions $\epsilon'(\omega)$ and $\epsilon''(\omega)$ of for bulk gold (a) and silver (b). Experimental measurement values by Johnson and Christy [19] and theoretical fitting values with the Drude-Sommerfeld model are shown by solid curves and dotted curves, respectively.

2.1.2 Influence of interband transitions

For noble metals such as gold and silver, the electrons in deeper levels contribute to their dielectric function as well. The interband transition of the electrons gives an additive complex contribution $\chi_{IB} = \chi'_{IB} + i\chi''_{IB}$ to the susceptibility [4, 20]. The linear optical response due to the interband transitions is normally described by the band structure model of the solid state. Based on the electric-dipole approximation for electron-photon interaction Hamiltonian of direct transitions, χ_{IB} is given by the band structure $E(k)$ and transition matrix elements M_{if} between initial (i) and final (f) states as [21]:

$$\chi_{IB} = \frac{8\hbar^2\pi e^2}{m_{eff}^2} \sum_{i,f} \int_{BZ} \frac{2dk}{(2\pi)^2} |\boldsymbol{e}M_{if}(k)|^2 \cdot \left\{ \frac{1}{[E_f(k) - E_i(k)][(E_f(k) - E_i(k))^2 - \hbar^2\omega^2]} + i\frac{\pi}{2\hbar^3\omega^2}\delta[E_f(k) - E_i(k) - \hbar\omega] \right\}$$

Here m_{eff} denotes the effective mass due to the coupling of free electrons to the ion core, the integral is over the Brillouin zone, $\boldsymbol{e}$ is the unit vector along the direction of the electric field, and $E_i(k)$ and $E_f(k)$ denote the initial and final electron energy levels.

The imaginary part χ''_{IB} of the interband transition susceptibility describes the direct energy dissipation and becomes large for the frequencies where the interband

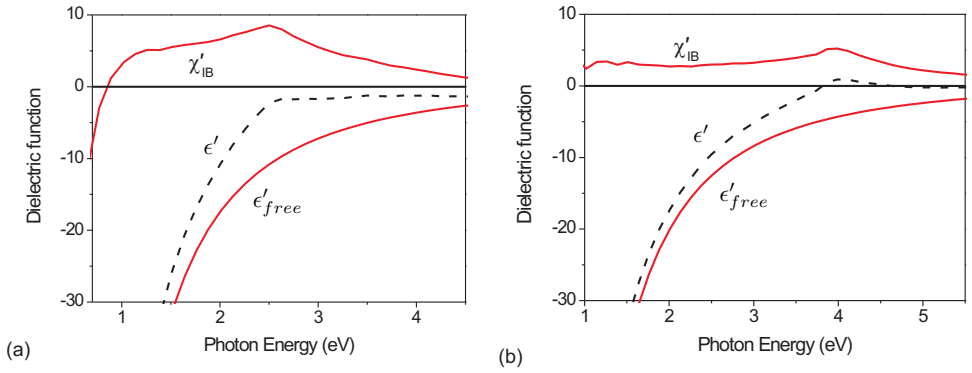

Figure 2.2: The decomposition of the experimental values of ϵ' of gold (a) and silver (b) into free electron contribution ϵ'_{free} and interband transition contribution χ'_{IB}.

transitions occur. The real part χ'_{IB} plays an important role at smaller frequencies as well. The important consequence in the above discussions is that independent optical excitation processes in the metal result in a modified complex dielectric function $\epsilon(\omega) = 1 + \chi_{DS}(\omega) + \chi_{IB}(\omega)$, which determines all optical properties of metals around the visible region including the optical absorption. Figure 2.2 depicts the decomposition of measured $\epsilon'(\omega)$ into the Drude free electron contribution ϵ'_{free} and the interband transition contribution χ'_{IB}.

2.1.3 Skin depth of metals

The dielectric function is directly linked to the complex index of refraction by

$$n(\omega) = n_r(\omega) + i\kappa(\omega) = \sqrt{\epsilon' + i\epsilon''}, \tag{2.6}$$

which describes the propagation of electromagnetic waves through the bulk materials. The wavelength λ of the propagating wave in a medium is related to the wavelength λ_0 in vacuum by $\lambda = \lambda_0/n_r$. The damping of an electromagnetic wave in the direction of propagation is described by the imaginary part κ. An electromagnetic waves impinging on a metal surface has a finite penetration depth due to energy dissipation. This can be simply explained from the dielectric functions. Assuming a plane wave propagating in the x direction, the electric field can be written as

$$\boldsymbol{E} = \boldsymbol{E}_0 e^{i(\boldsymbol{k}x - \omega t)}, \tag{2.7}$$

where $\boldsymbol{k}$ is the wave vector within the metal with $|\boldsymbol{k}| = (\omega/c)(n_r + i\kappa)$ and c is the light velocity in vacuum. Thus, the electric field within the metal can be rewritten

as

$$\boldsymbol{E} = \boldsymbol{E}_0 e^{i\omega(xn_r/c-t)} e^{-x/\delta}, \tag{2.8}$$

with

$$\delta = \frac{c}{\omega\kappa} = \frac{\lambda}{2\pi\kappa}. \tag{2.9}$$

where δ is the skin depth, which determines the attenuation of the electric field. The absorption coefficient κ can be derived from Eq. 2.6 as

$$\kappa = \sqrt{-\frac{\epsilon'}{2} + \frac{1}{2}\sqrt{\epsilon'^2 + \epsilon''^2}}. \tag{2.10}$$

Metals are generally characterized by large values of κ in the optical regime, and the electromagnetic waves are strongly damped within several tens of nanometers inside the metal. For example, gold and silver have skin depths of 31 nm and 24 nm, respectively, for a photon energy of 2 eV [4].

2.2 Surface plasmons

Surface plasmons are electromagnetic surface waves propagating along a metallic surface or on metallic films [2, 22]. Figure 2.3(a) shows a schematic view of surface plasmons at the interface between a metal and a dielectric medium. They are collective charge oscillations at the metal surface and induce electromagnetic fields with components parallel and perpendicular to the boundary. The waves are bound to the surface due to the evanescent character of the fields. The field distribution along the surface can be described as

$$E = E_0^{\pm} e^{i(k_x x \pm k_z z - \omega t)} \tag{2.11}$$

with a '+' sign for $z > 0$ and a '-' sign for $z < 0$. The imaginary k_z causes the exponential decay of the field in the z direction, as schematically shown in Fig. 2.3(b). The eigenfrequency ω of the surface plasmons is directly connected with the wave vector k_x, which is defined by the dispersion relation [3, 5]

$$k_x = \frac{\omega}{c}\left(\frac{\epsilon_m \epsilon_d}{\epsilon_m + \epsilon_d}\right)^{1/2}, \tag{2.12}$$

where ϵ_m and ϵ_d are the dielectric constants of the metal and the dielectric medium, respectively. With the assumption of real ϵ_d, and $\epsilon_m'' < |\epsilon_m'|$, the complex $k_x = k_x' + ik_x''$ can be written as

$$k_x' = \frac{\omega}{c}\left(\frac{\epsilon_m' \epsilon_d}{\epsilon_m' + \epsilon_d}\right)^{1/2}. \tag{2.13}$$

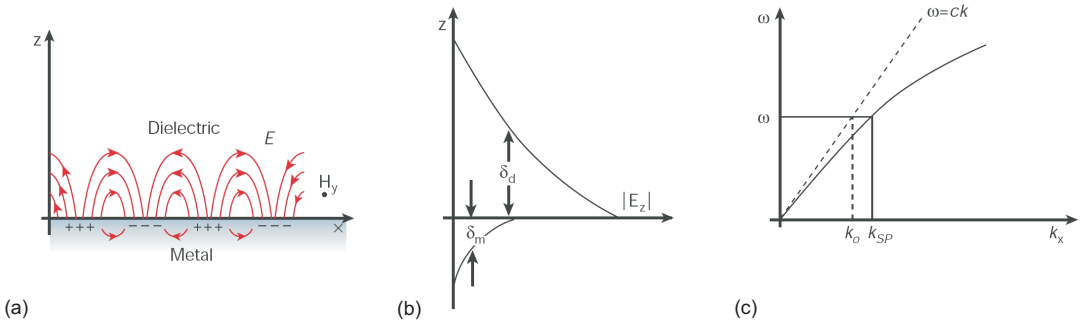

Figure 2.3: (a) Schematic diagram of the charges and the electromagnetic fields of surface plasmons propagating on a surface in the x direction. (b) The exponential decay of the field E_z with the distance away from the surface. (c) The dispersion relation of a surface plasmon mode. In order to couple light and surface plasmons, the momentum mismatch must be overcome.

$$k_x^{''} = \frac{\omega}{c}\left(\frac{\epsilon_m^{'}\epsilon_d}{\epsilon_m^{'}+\epsilon_d}\right)^{3/2}\frac{\epsilon_m^{''}}{2(\epsilon_m^{'})^2}. \tag{2.14}$$

For real $k_x^{'}$, one needs $\epsilon_m^{'} < 0$ and $|\epsilon_m^{'}| > \epsilon_d$, which can be fulfilled in a metal. $k_x^{''}$ determines the internal absorption. Figure 2.3(c) shows the dispersion relation of surface plasmons at the air/metal interface. One can see that the surface plasmon modes always lie beyond the light line, therefore, the surface plasmons are nonradiative and can not transform into light. To excite the surface plasmons with light, a special light-plasmon coupler is needed to overcome the momentum mismatch.

The wave vectors k_{zm} and k_{zd} of surface plasmons are imaginary due to the relations $\omega/c < k_x$, and $\epsilon_m^{'} < 0$. Therefore, normal to the surface, the field amplitude of the the surface plasmons decreases exponentially as $\exp(-|k_{zi}||z|)$. The penetration depth of the electric field can be written as

$$\delta_i = \frac{\lambda}{2\pi}\left(\frac{\epsilon_m^{'}+\epsilon_d}{\epsilon_i^2}\right)^{1/2}, \tag{2.15}$$

where $i = d$ is for the medium with ϵ_d and $i = m$ for the medium with ϵ_m. Figure 2.3 (b) shows the exponential decay of the field $|E_z|$ on the both side of the surface.

Due to the imaginary vector $k_x^{''}$, the intensity of surface plasmons propagating along a smooth surface decreases as $e^{-2k_x^{''}x}$. The length L_{SP} after which the intensity decreases to $1/e$ is given by

$$L_{SP} = (2k_x^{''})^{-1}. \tag{2.16}$$

The surface plasmon propagation length sets the upper size limit for any photonic circuit based on surface plasmons.

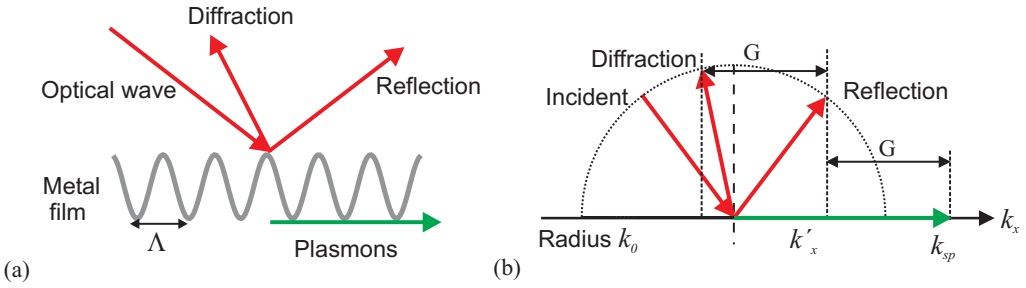

Figure 2.4: (a) The grating coupler used to excite surface plasmons. (b) Wave vector diagram of the input coupler. k_0 is the wave vector of incident light, k_{sp} of the surface plasmons, and $G = 2\pi/\Lambda$, where Λ is the grating constant.

When a metal film is embedded in a dielectric medium and the film thickness is comparable to the penetration depth of the surface plasmons, the interaction between the surface plasmons guided by the two interfaces can not be neglected. This interaction leads to a thickness-dependent dispersion relation. For detailed information, see refs [23, 24, 25].

Generally, the generation of surface plasmons at a metal-dielectric interface requires a matching of the parallel wave vector component of the excitation field with that of the surface plasmons. Experimentally two methods have been developed to bypass this technical problem: attenuated total reflection and grating coupling [3].

When the light ($k_0 = \omega/c$) hits a grating with a grating constant Λ at an incident angle θ, its component in the surface can have wave vectors $k_0 \sin\theta \pm mG$ with m an integer and $G = 2\pi/\Lambda$. Surface plasmons will be excited when the following relationship is fulfilled:

$$k_x = k_0 \sin\theta \pm mG = k_0 \sqrt{\frac{\epsilon_m}{\epsilon_m + 1}} = k_{SP}, \tag{2.17}$$

where 1 is the dielectric constant of vacuum. Figure 2.4 shows a grating coupler and its k-vector diagram. The incoming wave with $k_0 \sin\theta$ is transformed into surface plasmons by the addition of $\Delta k = G$. The resonance is observed as a minimum in the reflection of the light.

When the light is reflected from a metal surface covered by an optically dense medium, e.g., a quartz cylinder (Fig. 2.5), the momentum projection on the surface can be written as

$$k_x = \sqrt{\epsilon_d}\frac{\omega}{c}\sin\theta_0. \tag{2.18}$$

Surface plasmons on the interface of air/metal can be excited when the dispersion

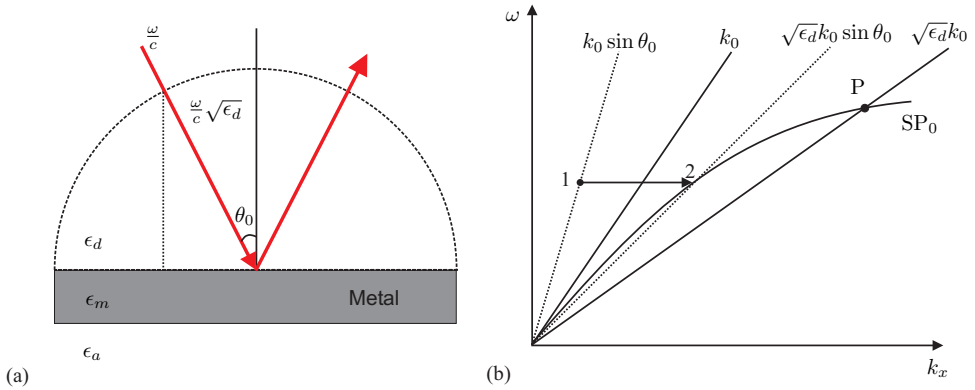

Figure 2.5: (a) Reflection of light at a metal surface ($\epsilon_m(\omega)$). The medium above the metal is a dielectric medium (ϵ_d) as glass or quartz; below the metal is air or a vacuum (ϵ_a). (b) Wave vector diagram in ATR method. SP_0: Dispersion of surface plasmons at metal/air interface.

relation

$$k_x = \sqrt{\epsilon_d}\frac{\omega}{c}\sin\theta_0 = k_0\sqrt{\frac{\epsilon_m}{\epsilon_m + 1}} = k_{SP} \tag{2.19}$$

is fulfilled, where ϵ_d and ϵ_m are the dielectric constants of the dielectric medium and the metal, respectively. The corresponding wave vector diagram is shown in Fig. 2.5(b). The excitation is recognized as an attenuated total reflection (ATR) intensity. Two different ATR configurations have been used to excite surface plasmons: Otto configuration and Kretschmann-Raether configuration.

The Otto configuration [26] is depicted in Fig. 2.6(a), the dielectric prism(ϵ_p) is separated from a half metal surface(ϵ_m) by an air or dielectric slit (ϵ_d) at a distance d, which is in the order of $\lambda_0/\sqrt{\epsilon_p}$. When the light is reflected at the boundary of the prism, the evanescent field can couple with the surface plasmons on the interface of air and metal.

Besides the Otto-configuration, the Kretschmann-Raether configuration [27] is used to excite surface plasmons on thin metal films. As shown in Fig. 2.6(b), the metal film ϵ_m with a thickness of several tens of nanometers is in contact with the prism ϵ_d. The electromagnetic field decays exponentially inside the film and excites the surface plasmons on the interface of the metal and air.

It is worthwhile to mention that surface plasmons can be excited via any rough surface (corrugated surface, grating, etc.), and the strong electromagnetic field is built up at the surface [3]. The reverse process can take place also: Surface plasmons propagating along the metal-dielectric interface can be transformed into photons via

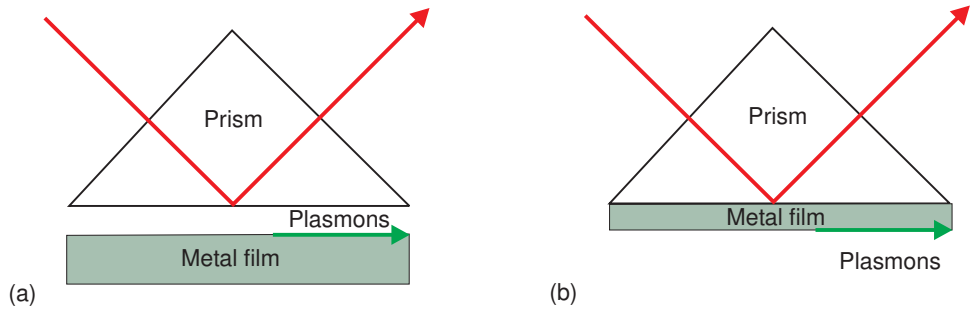

Figure 2.6: (a) Otto configuration. The dielectric or air lies between the prism and the metal surface. (b) Kretschmann-Raether configuration. The metal film is in contact with the prism.

the roughness of the surface, so that the surface plasmon field becomes radiative and a strong light emission results. These processes are significant in experiments and have been applied for the enhanced light emission from rough or sinusoidal surfaces, the photoemission enhanced by surface plasmons, strong Ramman scattering, or the generation of second harmonics in the strong surface plasmon field.

2.3 Optical properties of metallic nano-particles

Metallic nano-particles have attracted a lot of interest since they show unique optical properties. The optical response of a metal particle depends strongly on the size and material properties. The general solution of the scattering of electromagnetic radiation by spheres within the framework of electrodynamics was given by Mie in 1908 [1].

Commonly, the optical properties are expressed in terms of an extinction cross section, which is related to the intensity loss $\Delta I(z)$ of a parallel beam of incident light. Following the Lambert-Beer law, we have

$$\Delta I_{ext}(z) = I_0(1 - e^{N\sigma_{ext}z}), \tag{2.20}$$

where σ_{ext} is the extinction cross section of a single particle and N is the number density of particles. Intuitively, extinction depends only the scattering amplitude in the forward direction. However, the derivation shows that the extinction is the interference between the incident and forward scattered light [28]. From energy conservation point of view, the extinction is the combined effect of absorption and scattering with

$$\sigma_{ext} = \sigma_{abs} + \sigma_{sca}. \tag{2.21}$$

2.3.1 Spherical particle scattering

Within Mie's theory, the extinction and scattering cross sections can be obtained by expanding the involved fields into series of partial waves in various spherical symmetries as [1, 28]:

$$\sigma_{ext} = \frac{2\pi}{|\boldsymbol{k}|^2} \sum_{L=1}^{\infty} (2L+1) Re\{a_L + b_L\}, \tag{2.22}$$

$$\sigma_{sca} = \frac{2\pi}{|\boldsymbol{k}|^2} \sum_{L=1}^{\infty} (2L+1)(|a_L|^2 + |b_L|^2), \tag{2.23}$$

where a_L and b_L are the scattering coefficients, the summation index L is determined by the order of the partial waves that are described by vector spherical harmonic functions of the electric and magnetic fields.

Mie's theory solves the single spherical particle diffraction problem. The solution is mainly determined by the dielectric function $\epsilon(\omega)$ of the particle, the size of the particle, and the dielectric function of the surrounding medium. $\epsilon(\omega)$ may differ from $\epsilon_{bulk}(\omega)$ in the case of small particles, where the intrinsic size effects come into play. However, the intrinsic size effects become important only for the particles with $R \leq 10$ nm, and the material dielectric functions vary as a function of the particle size written $\epsilon(\omega) = \epsilon(\omega, R)$. As for larger particles with $R \geq 10$ nm, extrinsic size effects dominate the optical spectral properties, and the material dielectric functions are radius independent as $\epsilon(\omega) = \epsilon_{bulk}(\omega)$ [4].

Figure 2.7(a) shows the calculated extinction of single spherical gold nano-particles in dependence of the particle diameter d based on Mie's theory. The dielectric constant of gold is taken from experimental measured values for bulk gold [19], and the particles are embedded in a material with a refractive index $n_{med} = 1.33$. The diameter of the gold particle d is increased from 20 nm to 80 nm in steps of 20 nm. Each spectrum shows a clean resonance in the visible spectral range, and with the increasing size of the particle, the maximum of the resonance shifts to a longer wavelength. Due to the resonance shifts, the colors of the gold nano-particles are clearly changed [29]. Figure 2.7(b) illustrates The color change of gold nano-particles with size variation.

Although Mie's theory describes the spectral response of small particles quite well, it was not until 60 years later that the physical insight into material properties of Mie's theory was proposed [30, 31]. The Mie resonance was interpreted as collective plasmon oscillations of different multipole orders in analogy to the bounded gaseous plasma oscillations. The order of partial waves in Mie's solution gives the order of

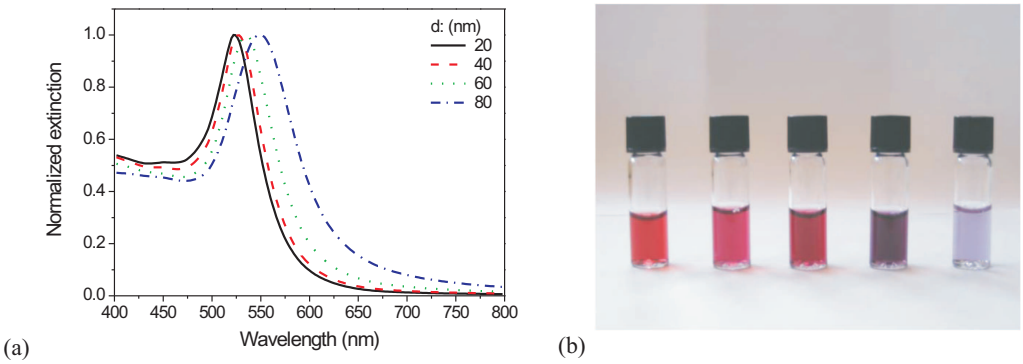

Figure 2.7: (a) Calculated extinction spectra of gold nanoparticles in various sizes. The surrounding medium is assumed to have a refractive index of $n = 1.33$. (b) The color of gold particle solutions with diameters 12, 18, 30, 40 and 72 nm (from left) [29].

spherical multipole excitations in the particle. Far away from the particle, the waves are identical to waves coming from equivalent point multipoles. Both electric and magnetic multipoles are due to electronic excitations and depend on the dielectric function.

2.3.2 Electrostatic approximation

Mie's theory gives the exact solution of the scattering of electromagnetic radiation by spheres, however, for particles with a size much less than the wavelength ($R << \lambda$), the *electrostatic approximation* gives a good estimate as well. When a metal particle is placed in a electric field, surface polarization will be induced as shown in Fig. (2.8). With the correct boundary conditions, the electric field inside the metal particle can be written as [4, 32]

$$E_i = E_0 \frac{3\epsilon_d}{\epsilon_m + 2\epsilon_d}, \tag{2.24}$$

where ϵ_d is the dielectric function of the surrounding medium. With the definition of the dipole moment $\boldsymbol{p} = \epsilon_d \alpha \boldsymbol{E}_0$, the static polarizability of the sphere can be written as

$$\alpha = 4\pi\varepsilon_0 R^3 \frac{\epsilon_m - \epsilon_d}{\epsilon_m + 2\epsilon_d}. \tag{2.25}$$

This solution is also valid to small metallic spheres in an oscillating electromagnetic field in the quasi-static regime, where the electromagnetic field is characterized by a time dependence but no *spatial* dependence. Thus the metallic spheres interact with a spatially uniform field. For the frequency dependent dielectric function of

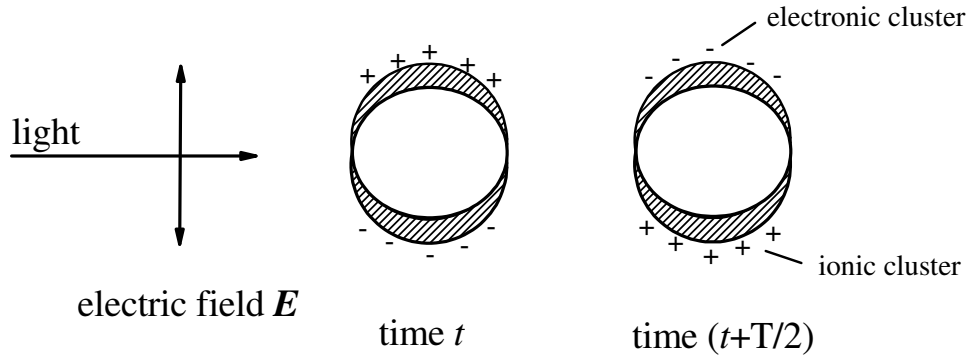

Figure 2.8: A dipolar surface plasmon excitation in a spherical particle by the electric field of the incident light. The frequency of the light wave is $\nu = 1/T$

the metal $\epsilon_m(\omega) = \epsilon_m^{'}(\omega) + i\epsilon_m^{''}(\omega)$, a strong resonance will occur whenever $|\epsilon_m + 2\epsilon_d|$ is at a minimum. In the case of $\epsilon_m^{''}(\omega) \ll 1$ or a small frequency dependence of $\partial\epsilon_m^{''}/\partial\omega$, the resonance frequency is determined by

$$\epsilon_m^{'} = -2\epsilon_d. \tag{2.26}$$

For free electron metals, with Eq. (2.4) and $\epsilon_d = 1$, the metal sphere resonance frequency is defined as

$$\omega_1 = \frac{\omega_p}{\sqrt{3}}. \tag{2.27}$$

ω_1 is interpreted as the classical surface plasmon frequency. At this frequency, the displacement of the negative charges due to an external electric field gives rise to polarization charges at the cluster surface, which produce a linear restoring force to drive the conduction electrons in the cluster acting like an oscillator system, as shown in Fig. 2.8.

2.3.3 Non-spherical particles

Mie's theory only provides an exact solution for the scattering and absorption phenomena of spherical particles. For elliptical particles, the scattering was normally solved within the electrostatic approximation approach [4, 28]. Since this approach is limited in the quasi-static regime, the formulation is restricted for small ellipsoids, and any retardation effects will be neglected. The extinction cross section can be obtained by calculating the polarizability of the elliptical particles.

For an ellipsoid as shown in Fig. 2.9, it is defined by three principle axes a, b, and c as

$$\frac{x^2}{a^2} + \frac{y^2}{b^2} + \frac{z^2}{c^2} = 1. \tag{2.28}$$

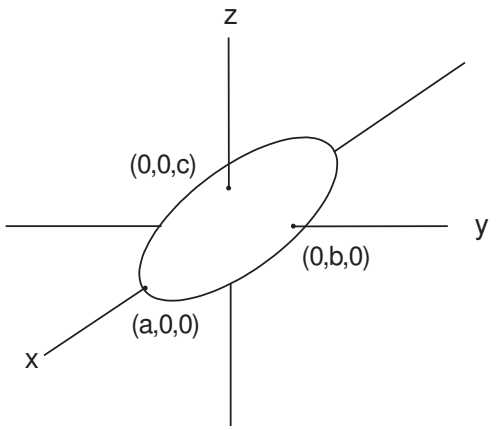

Figure 2.9: Ellipsoidal particle with semi-axes $a > b > c$.

When the principle axes of the particle are aligned along coordinate axes, its polarization $\boldsymbol{P}$ connects to the external field $\boldsymbol{E}$ with a second-order tensor polarizability $\hat{\alpha}$ by the definition $\boldsymbol{P} = \epsilon_d \hat{\alpha} \boldsymbol{E}$ in the form of

$$\begin{pmatrix} p_x \\ p_y \\ p_z \end{pmatrix} = \epsilon_d \begin{pmatrix} \alpha_x & 0 & 0 \\ 0 & \alpha_y & 0 \\ 0 & 0 & \alpha_z \end{pmatrix} \begin{pmatrix} E_x \\ E_y \\ E_z \end{pmatrix}, \tag{2.29}$$

where ϵ_d is the dielectric constant of the surrounding medium. The electric polarizability α_i for the field direction parallel to the principle axis i is given by

$$\alpha_i = \varepsilon_0 \frac{\epsilon_m(\omega) - \epsilon_d}{\epsilon_d + L_i(\epsilon_m(\omega) - \epsilon_d)} \frac{4\pi}{3} abc, \tag{2.30}$$

where L_i $(i = a, b, c)$ are the geometrical depolarization factors determined by the shape of the particle as

$$L_i = \frac{abc}{2} \int_0^\infty \frac{dq}{(r_i^2 + q)\sqrt{(a^2 + q)(b^2 + q)(c^2 + q)}}. \tag{2.31}$$

Here r_i are the semi-axes a, b, and c. The geometrical factors are related by

$$L_a + L_b + L_c = -abc \int_0^\infty \frac{d}{dq} \frac{1}{f(q)} dq = 1, \tag{2.32}$$

leaving only two of them independent. Similar to the spherical particle case, three optical resonances are determined by setting the denominator of Eq. (2.30) to zero. In the case of a small imaginary part $\epsilon_m''(\omega)$, the resonance position can be approximately estimated by

$$\epsilon_m'(\omega) = \epsilon_d \left(1 - \frac{1}{L_i}\right). \tag{2.33}$$

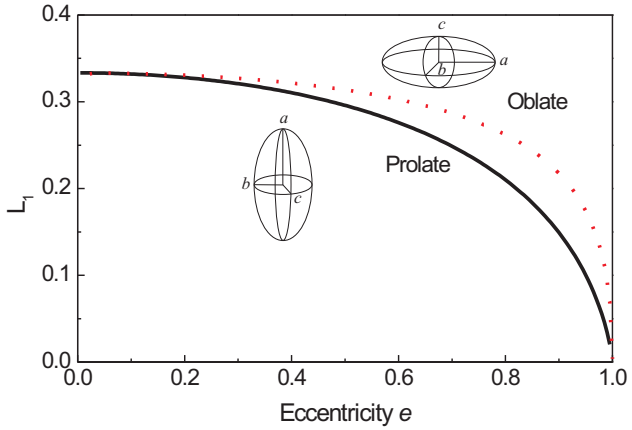

Figure 2.10: Geometric depolarization factors of spheroids.

For spheroids, i.e., ellipsoids which have two of three axes with equal lengths, the geometrical depolarization factor can be expressed as a function of the eccentricity $e = \sqrt{(a^2 - c^2)}/a$. For prolate spheroids ($a > b = c$ and $L_2 = L_3$)[28]:

$$L_1 = \frac{1 - e^2}{e^2}\Big(-1 + \frac{1}{2e}\ln\frac{1 + e}{1 - e}\Big). \tag{2.34}$$

For oblate spheroids ($a = b > c$ and $L_1 = L_2$),

$$L_1 = \frac{g(e)}{2e^2}\Big[\frac{\pi}{2} - \tan^{-1} g(e)\Big] - \frac{g(e)^2}{2},\ g(e) = \Big(\frac{1 - e^2}{e^2}\Big)^{1/2}. \tag{2.35}$$

Figure 2.10 shows the of depolarization L_1 of spheroids as a function of the eccentricity e. Basically, the axial ratio (c/a) of the spheroid determines its resonance position.

It should be stressed that, different from Mie's theory, only dipole mode can be excited for spheres and ellipsoids in the quasi-static approximation. For both spherical and ellipsoidal particles, the negative value of $\epsilon_m^{'}(\omega)$ is required to obtain a resonance and this is fulfilled by the metals below the plasma frequency ω_{pl}.

At resonance, the local field of metallic nano-particles is orders of magnitude enhanced with respect to the incident field. This fact has been applied in experiments of photon-enhanced chemical reactions [33] and surface-enhanced Raman scattering (SERS) [6, 7, 8]. This field enhancement is also sensitive to the refractive index of the medium that surrounds the particles. The resonance spectrum shift of nano-particle plasmons is used in biomolecular recognition etc [34].

2.4 Nanoapertures in metal films

As the complementary structures of nano-particles, nano-apertures in the sub-wavelength scale in metal films also exhibit excellent optical properties such as enhanced transmission and sub-diffraction resolution imaging. The enhanced transmission of sub-wavelength nano-apertures in metal films was first discovered in a hole array in an optically opaque metal film [35]. The mechanism of such enhanced transmissions was explained as surface-plasmon related due to the periodicity. However, recently it was demonstrated that the transmission properties of the sub-wavelength aperture arrays are strongly influenced by the shape of the apertures [36]. Moreover, the enhanced transmission was also demonstrated in single nano-apertures [37] and aperiodic arrays of nano-apertures [38]. In order to apply the enhanced transmission properties of sub-wavelength apertures, it is important to understand the fundamental physical mechanisms.

2.4.1 Nano-aperture arrays

The enhanced transmission of sub-wavelength apertures was first discovered in periodic hole arrays in optically thick metallic films [35, 39]. Figure 2.11 shows the SEM image of a typical hole array and the corresponding transmission spectrum. Several peaks are observed in the visible and near-infrared spectral range. By comparing the spectral positions with the period and the symmetry of the array, the enhanced transmission effect was concluded to benefit from the surface plasmon excitation due to the periodicity. A two dimensional aperture array with lattice constant a_0 can act as a grating and provide wave vector components $2\pi m/a_0$ along the x axis, and $2\pi n/a_0$ along the y axis, with m and n being integers. At normal incidence, surface plasmons can be excited when the following condition is matched:

$$k_{sp} = \sqrt{m^2 + n^2}(2\pi/a_0). \tag{2.36}$$

With Eq. 2.19, the transmission peak position λ_{max} can be estimated in a first approximation by:

$$\lambda_{max} = \frac{a_0}{\sqrt{m^2 + n^2}} \sqrt{\frac{\epsilon_m \epsilon_d}{\epsilon_m + \epsilon_d}}. \tag{2.37}$$

The surface plasmon model has explained the experimental observation of the transmission spectra of sub-wavelength hole arrays.

However, this approximation is limited to the circularly shaped aperture arrays. When the aperture shape is altered from circular to rectangular, the transmission spectra of the arrays will change dramatically. Klein *et al.* [36, 40] demonstrated

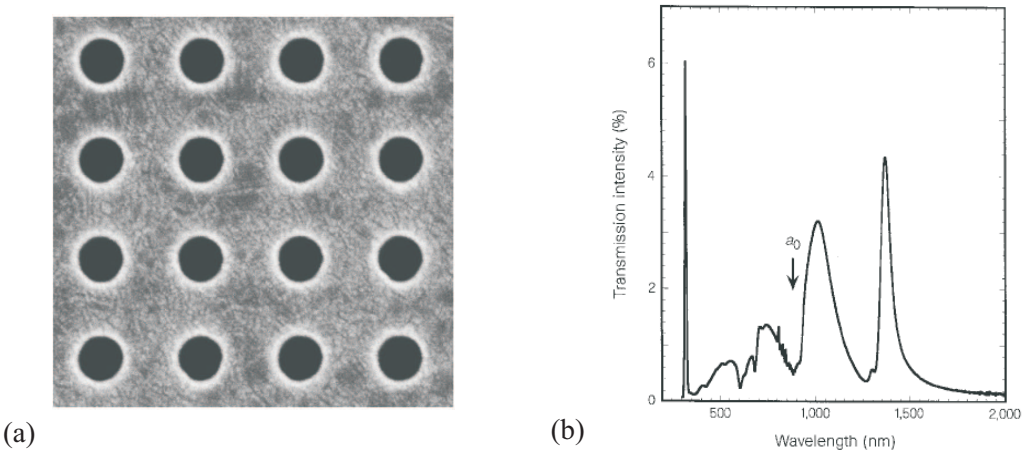

Figure 2.11: (a) SEM micrograph images of the subwavelength cylindrical hole arrays with period $a_0 = 0.9$ μm, hole diameter $d = 150$ nm, and film thickness $t = 200$ nm. (b) Zeroth-order transmission spectrum of the hole array [35].

experimentally that aperture shapes also play an important role in the enhanced transmission. Figure 2.12 presents the measured transmission spectra for the three different sub-wavelength aperture arrays with the incident light polarized perpendicular to the long axis of the holes. The transmissivity changes dramatically when the aperture shape varies. For each spectrum, (1,0), (1,1), and (2,0) order maxima corresponding to the surface plasmon excitation are observed at slightly longer wavelengths with respect to the corresponding minima. The peak value of each order maximum increases when the shape of the aperture is altered from circular to rectangular. Moreover, the transmission peaks of the rectangular aperture array shift to longer wavelengths when the aspect ratio (long axis/short axis) of the aperture is increased. This behavior can not be explained merely in terms of surface plasmons, as the film thickness and the periodicity were kept constant.

The transmissivity of rectangular holes also shows a strong polarization dependence [40, 41]. The changes in transmissivity for the rectangular holes with respect to the circular holes are attributed to the existence of a *shape resonance*. It was postulated that this shape effect was the result of localized surface plasmons. However, most studies with periodic hole arrays indicated that periodicity may dominate the transmission properties of nanoholes [41, 42]. Moreover, enhanced transmission has been demonstrated in aperiodic hole arrays in metal films [38, 43]. The roles of the shape resonance and surface plasmon excitation are not clearly understood yet.

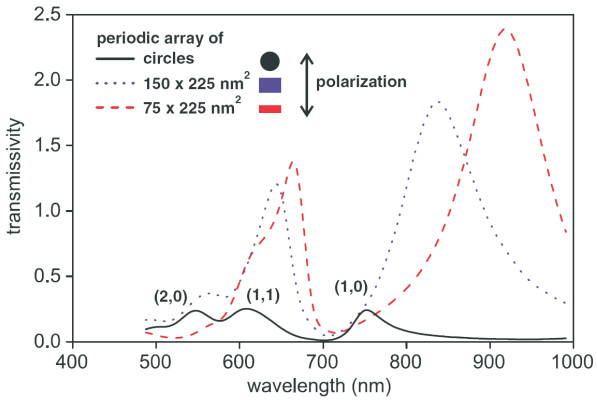

Figure 2.12: Transmission spectra of three different aperture shape arrays. Circular apertures have a diameter of 190 nm, rectangular apertures have dimensions of 150 nm × 225 nm and 75nm × 225 nm. All the aperture arrays are fabricated in a 200 nm thick gold film which are deposited on a glass substrate. All the arrays are arranged in a square lattice with an equal period of 425 nm [36].

2.4.2 Single nano-apertures

In addition to the sub-wavelength aperture arrays, individual nano-apertures [37, 41, 44] also show unique optical properties such as achieving sub-diffraction limit light spots, strong field enhancement, and high power throughout. Nano-apertures in optically thick metal films can behave as waveguides. Their transmission properties are strongly influenced by the cut-off wavelengths of the waveguides. It has been demonstrated that C shaped apertures [45] and bowtie shaped apertures [46] have the capability to provide high power throughout with sub-diffraction resolution light spots, compared to the regular shape apertures with the same areas.

Different from the circular and square apertures, the transmissivity and near-field optical spot resolution of the irregular shape apertures shows a strong polarization dependence [45, 46]. Figure 2.13 shows a schematic of the four types of apertures: the C-shaped aperture, the square and rectangular apertures with the same area, and the small square aperture which has the same small feature size of the C-shaped aperture. When the apertures are patterned on an optically opaque gold film, they show different transmission capability in the visible range. Figure 2.14 shows the transmission pattern taken with a digital camera when illuminating the white light through the aperture arrays under the microscope. The transmission characteristics of the various apertures are straightforwardly observed from the color and brightness of the transmitted light [45].

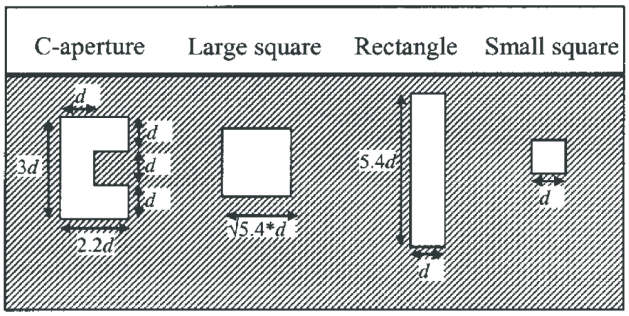

Figure 2.13: Schematic of sub-wavelength apertures in various shapes: the C-shaped aperture, the square and rectangle aperture with the same area, and the small square aperture which has the same feature size as the C-shaped aperture [45].

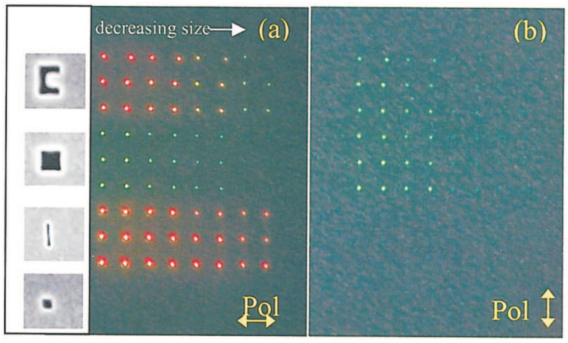

Figure 2.14: Transmission pattern taken through microscope eyepiece of the different shaped apertures under (a) horizontal and (b) vertical polarization. Left side shows the SEM images of example apertures. Each group of three rows was fabricated with the same shape [45].

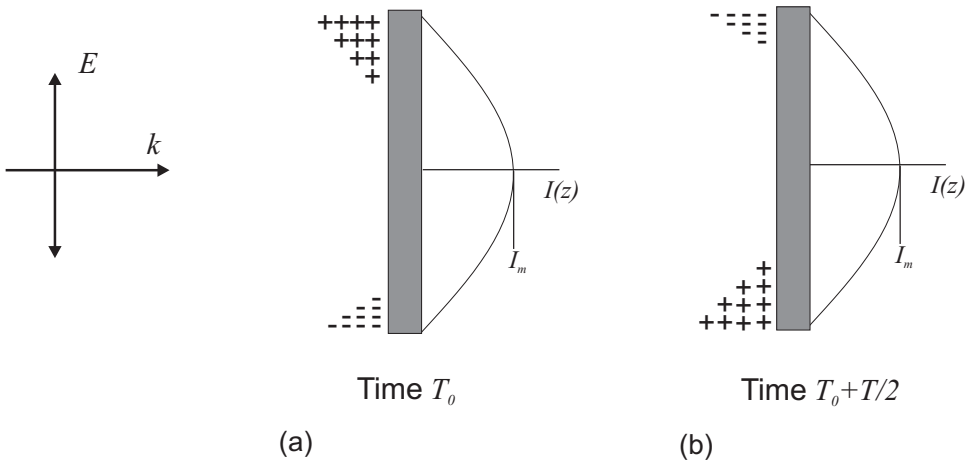

Figure 2.15: Current distribution of an optical dipole antenna under the external field excitation. Time-varied electric field $E = E_0 \cos(\omega t + \phi_0)$ at the instant $t = T_0$ reach maximum amplitude, where $\omega = 2\pi/T$ is the frequency of the incident light. The corresponding charge distribution and the induced current for $t = T_0$ and $t = T_0 + T/2$ are shown in (a) and (b).

Most current investigations on the individual apertures are focused on the transmission dependence on the aperture shape variation by keeping the aperture area constant. However, as mentioned in the aperture array case, the localized surface plasmons of individual apertures are strongly geometry dependent. In Chapter 5, we show that the transmission properties of the hole arrays are mainly determined by the localized resonances of the individual holes. The period only plays an important role in the transmission spectra when it is comparable with the resonance wavelength of the individual aperture.

2.5 Optical nanoantennas

Nanostructures composed of noble metals with typical dimensions comparable to the wavelength of light can often support optical resonances due to the collective charge oscillation excitation. They are commonly called plasmon polariton excitation [4]. For a metallic cut-wire as shown in Fig. 2.15, time-varied external electric fields can induce current distributions which are similar to those of a half-wave dipole antenna in radio frequency range. At resonance, metallic nano-structures show similar behaviors as antennas. In nano-optics, such structures are generally referred to optical nano-antennas [47].

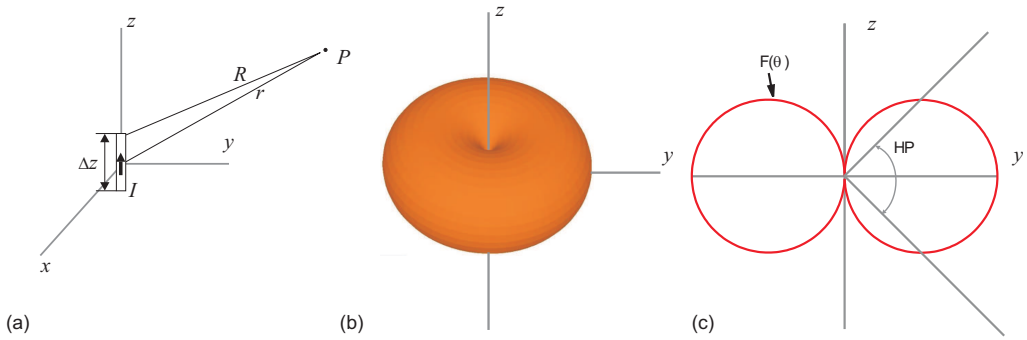

Figure 2.16: (a) An ideal dipole with uniform current I in length Δz, $\Delta z << \lambda$ and $R \approx r$. (b) The radiation pattern from an ideal dipole. (c) E-plane radiation pattern polar plot of E_θ.

2.5.1 Fundamentals of antennas

Generally an antenna is a device that provides a means of radiating or receiving electromagnetic waves. More specifically, an antenna can provide a transition from a guided wave on a transmission line to a free space wave, and *vice versa* in the receiving case. Thus, information can be transferred between different locations without any intervening structures. Most antennas are reciprocal devices and behave the same as transmitters as well receivers. In the receiving mode, antennas act to collect incoming waves and direct them to a common feed point where a transmission line is attached. In some cases, antennas focus radio waves just as lenses focus optical waves. Most antennas have directional characteristics, which means that the electromagnetic power density is radiated from a transmitting antenna with intensity that varies with angle around the antenna.

Antennas are normally evaluated with antenna performance parameters [16]: Radiation pattern $\mathrm{F}(\theta, \phi)$, directivity D, gain G, polarization, impedance Z_A, etc. In the following, we will give an overview of the definitions of these parameters.

The *radiation pattern* gives the angular variation of radiation at a fixed distance from an antenna when the antenna is transmitting. Figure 2.16 shows an example of the normalized field pattern from an ideal dipole. As shown in Fig.2.16(a), the current amplitude I of an ideal dipole is uniform along the element length Δz. With Maxwell's equations, one can obtain the general field expression of an ideal dipole

as

$$H = \frac{I\Delta z}{4\pi} i\omega \left(1 + \frac{1}{i\beta r}\right) \frac{e^{-i\beta r}}{r} \sin\theta\hat{\phi}, \tag{2.38}$$

$$E = \frac{I\Delta z}{4\pi} i\omega\mu \left[1 + \frac{1}{i\beta r} - \frac{1}{(\beta r)^2}\right] \frac{e^{-i\beta r}}{r} \sin\theta\hat{\theta} + \frac{I\Delta z}{2\pi}\eta \left[\frac{1}{r} - i\frac{1}{\beta r^2}\right] \frac{e^{-i\beta r}}{r} \cos\theta\hat{r}, \tag{2.39}$$

where $\beta = \omega\sqrt{\mu\epsilon} = 2\pi/\lambda$. If βr is large ($\beta r >> 1$ or $r >> \lambda$), then the above equations can be written as

$$\begin{aligned} E &= \frac{I\Delta z}{4\pi} i\omega\mu \frac{e^{-i\beta r}}{r} \sin\theta\hat{\theta}, \\ H &= \frac{I\Delta z}{4\pi} i\beta \frac{e^{-i\beta r}}{r} \sin\theta\hat{\phi}. \end{aligned} \tag{2.40}$$

These are the field components of an ideal dipole at large distances away from the dipole. With the definition of the Poynting vector, one can obtain the complex power flux density out of a sphere of radius r surrounding the ideal dipole as:

$$\begin{aligned} S &= \frac{1}{2} E \times H^* \\ &= \frac{1}{2}\left(\frac{I\Delta z}{4\pi}\right)^2 \omega\mu\beta \frac{sin^2\theta}{r^2}\hat{r}, \end{aligned} \tag{2.41}$$

which is a real quantity and radially directed. Thus, the total power flowing out through a sphere of radius r surrounding the ideal dipole can be written as

$$\begin{aligned} P_f &= \int\int S \cdot ds = \frac{1}{2}\left(\frac{I\Delta z}{4\pi}\right)^2 \omega\mu\beta \int_0^{2\pi} d\phi \int_0^{\pi} sin^3\theta d\theta \\ &= \frac{\omega\mu\beta}{12\pi}(I\Delta z)^2. \end{aligned} \tag{2.42}$$

This flowing power indicates the dissipated power that travels away from the source and is referred to as radiated power. Correspondingly, the fields in Eq. 2.40 are called radiation fields. The larger distance region from an antenna is called far-field region, where all power is radiated power.

For distances in the range of $\beta r << 1$ or $r << \lambda$, only the terms with the largest inverse powers of r dominate the fields and Eq. 2.39 can be rewritten as

$$\begin{aligned} H' &= \frac{I\Delta z e^{-i\beta r}}{4\pi r^2} \sin\theta\hat{\phi}, \\ E' &= -i\eta \frac{I\Delta z}{4\pi\beta} \frac{e^{-i\beta r}}{r^3} \sin\theta\hat{\theta} + i\eta \frac{I\Delta z}{2\pi\beta} \frac{e^{-i\beta r}}{r^3} \cos\theta\hat{r}, \end{aligned} \tag{2.43}$$

where η is the intrinsic impedance of the medium and defined as $\eta = \sqrt{\mu/\epsilon}$. These fields are referred to as the near fields of the antenna. H' varies as $1/r^2$ and is equivalent to the induction field of a short steady or slowly oscillating current. E' varies as $1/r^3$ and is equivalent to the field of an electrostatic or quasi-static dipole with charges of $+q$ and $-q$ spaced Δz apart. With E' and H', the Poynting vector of these near fields can be defined as

$$\begin{aligned} S' &= \frac{1}{2}[E'_\theta H'^*_\phi \hat{r} - E'_r H'^*_\phi] \\ &= -\frac{i\eta}{2\beta}\left(\frac{I\Delta z}{4\pi}\right)^2 \frac{1}{r^5}(\sin\theta^2\hat{r} - \sin\theta\hat{\theta}). \end{aligned} \tag{2.44}$$

This power density vector is imaginary and corresponds to standing waves rather than travelling waves associated with radiation. Note from Eq. 2.43 that the electric field E' is in phase-quadrature with the magnetic field H', which indicates that energy is interchanged between these fields with time.

The power density associated with radiation exists everywhere and passes through the near field. For an ideal dipole, both radiation power density and near-field power density reach a maximum at 90°, and at the distance $r_0 = \lambda/2\pi$ they are equal. For the region from the antenna to r_0, the reactive field dominates over the radiative fields. This region is called the reactive near-field of the antenna. For the region with a distance large from the antenna, the radiated power density dominates, and it is called the far field region.

The concept of field regions introduced for an *ideal dipole* can be generalized to *any* finite antenna of maximum extent l. The distance to the far field r_{ff} is defined as

$$r_{ff} = \frac{2l^2}{\lambda}. \tag{2.45}$$

This is usually a sufficient condition for antennas operating at higher frequencies. However, the more general far field conditions are defined as follows:

$$\begin{aligned} r &> \frac{2l^2}{\lambda} \\ r &\gg l \\ r &\gg \lambda \end{aligned} \tag{2.46}$$

In the far field, the radiation pattern is independent of distance. The zone interior to r_{ff} is called the near field, which is divided into two subregions: reactive near field region and radiating near field region. In reactive near field region, reactive field dominates over the radiative field. While in radiating near field, the radiation fields dominate and the angular field distribution depends on distance from the antenna.

The far field is normally characterized by the angular distribution around the antenna, which is referred to as the radiation pattern. Figure 2.16(b) and (c) show the radiation from an ideal dipole. It is common to normalize the field expression to its maximum value $E_\theta(\max)$. For a z-directed source that has only a θ-component of $\boldsymbol{E}$, the normalized field pattern $F(\theta, \phi)$ is defined as

$$F(\theta, \phi) = \frac{E_\theta}{E_\theta(max)}, \tag{2.47}$$

where $E_\theta(max)$ is the maximum value of the magnitude of E_θ over a sphere of radius r. Thus, the normalized field pattern has the form:

$$F(\theta) = \sin\theta. \tag{2.48}$$

The directional properties of the radiation of an antenna are also described by another form of radiation pattern, the power pattern, which gives the angular dependence of the power density. The normalized power pattern is defined as

$$P(\theta, \phi) = |F(\theta, \phi)|^2. \tag{2.49}$$

Figure 2.17 shows a typical power pattern polar plot of an antenna in linear units. There are several lobes. The main lobe is the one containing the direction of maximum radiation. There are also some lobes smaller than the main lobe, which are called minor lobes. The width of the main beam is described by half-power beamwidth HP, which is the angular separation of the points where the main beam of the power pattern equals one-half the maximum value.

The *directivity* of an antenna expresses the ratio of the radiation density in a certain direction to the average radiation intensity, which is defined as

$$D(\theta, \phi) = \frac{U(\theta, \phi)}{U_{ave}}. \tag{2.50}$$

Here $U(\theta, \phi)$ is the power radiated in a given direction per unit solid angle, and U_{ave} is equivalent to the radiation intensity $U(\theta, \phi)$ that an isotropic source with the same radiated power P would radiate. Figure 2.18 illustrates the concept of directivity. If the radiation power is distributed isotropically over all of space, the radiation intensity would have a maximum value equal to its average value as shown in 2.18 (a), in which $U_m = U_{ave}$. Thus, the directivity of this isotropic pattern is unity. However, the distribution of the radiation intensity $U(\theta, \phi)$ of an real antenna is different from the isotropic pattern and is shown in 2.18(b), in which the maximum radiation intensity is reached in the direction $(\theta_{max}, \phi_{max})$ with a value

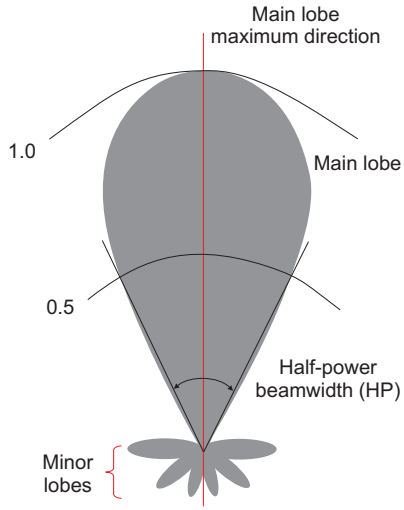

Figure 2.17: A typical power pattern polar plot of an antenna.

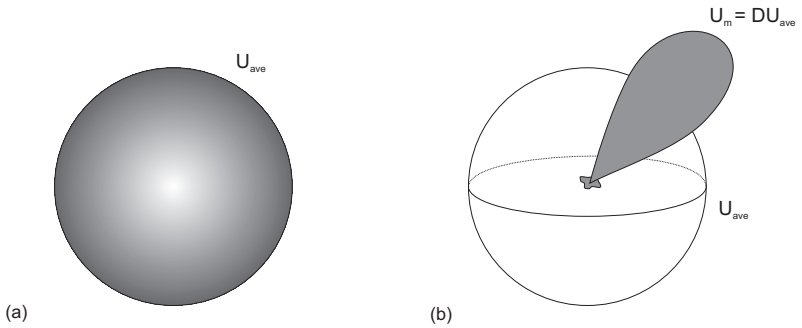

Figure 2.18: Illustration of directivity. (a) Radiation intensity distributed isotropically. (b) Radiation intensity from an actual antenna.

of $U_m = DU_{ave}$. By directing the radiated power P in a preferred direction, the radiation intensity in that direction can be increased with a factor of D over what it would be if the same radiated power had been isotropically radiated.

Gain G describes how efficiently the antenna transforms available power at its input terminals to radiated power together with its directive properties. Generally, it is described as the function of maximum directivity D and radiation efficiency e_r of the antenna as

$$G = e_r D. \tag{2.51}$$

The radiation efficiency e_r is used to describe the losses of the input power of the antenna, which is defined as

$$e_r = \frac{P}{P_{in}}. \tag{2.52}$$

Polarization describes the vector nature of electric fields radiated in a given direction by an antenna when transmitting. The polarization of waves radiated by an antenna will vary with direction. Usually, the polarization of an antenna remains relatively constant over its main beam, and is described by the polarization on the main beam peak. However, the polarization of the radiation from minor lobes can differ greatly from that of the main beam. A straight wire antenna radiates a wave with linear polarization parallel to the wire.

The *input impedance* is the impedance presented by the antenna at its terminals. It can be influenced by other antennas or nearby objects. Generally input impedance is composed of real and imaginary parts:

$$Z_A = R_A + iX_A. \tag{2.53}$$

The input resistance R_A represents two types of power dissipations: radiation losses and ohmic losses. The input reactance X_A represents the power stored in the near field of the antenna. As a consequence of reciprocity, the impedance of an antenna is identical during reception and transmission.

At resonance, the reactive losses due to the reactance X_A can be neglected. The average dissipated power of an antenna includes radiative and ohmic losses and is given by

$$P_{in} = P + P_{ohmic}, \tag{2.54}$$

$$\frac{1}{2}R_A|I_A|^2 = \frac{1}{2}R_r|I_A|^2 + \frac{1}{2}R_{ohmic}|I_A|^2, \tag{2.55}$$

where R_r is defined as the radiation resistance of an antenna referred to the input terminals as

$$R_r = \frac{2P}{|I_A|^2}. \tag{2.56}$$

R_{ohmic} is resistance associated with ohmic losses and defined as

$$R_{ohmic} = \frac{2P_{ohmic}}{|I_A|^2} = \frac{2(P_{in} - P)}{|I_A|^2}. \tag{2.57}$$

The relative amount of input power dissipated by radiation and ohmic losses determines the efficiency of an antenna. Based on Eq.2.52 and 2.55, the efficiency can be rewritten as

$$e_r = \frac{P}{P + P_{ohmic}} = \frac{R}{R + R_{ohmic}}. \tag{2.58}$$

In microwave frequency regime, for wire antennas, the skin depth $\delta = \sqrt{2/\omega\mu\sigma}$ is much smaller than the conductor radius. Thus, the ohmic resistance for a antenna

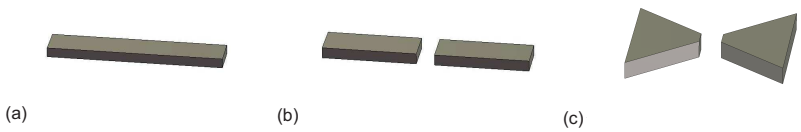

Figure 2.19: Schematic of optical antenna designs. (a) Resonant metallic bar. (b) Metallic dimer. (c) Metallic bow-tie.

of length L that carries an axially uniform current can be approximate as

$$R_{ohmic} \approx \frac{L}{2\pi a} R_s, \tag{2.59}$$

where a is the wire radius and R_s the surface resistance:

$$R_s = \sqrt{\frac{\omega\mu}{2\sigma}}. \tag{2.60}$$

We will show in Chapter 5 that the surface resistance of metals also plays an important role in the transmission efficiency of slot antenna arrays, although metals behave differently at optical frequencies.

2.5.2 Antennas at optical frequencies

At optical frequencies, the optical radiation is generally manipulated by redirecting the wavefronts with mirrors and lenses. However, due to the diffraction limit, the incident light field can not be localized into dimensions much smaller than the wavelength. In order to overcome this obstacle, the antenna concept is extended into optical frequencies. Optical antennas have many foreseeable applications such as high-resolution microscopy and spectroscopy [13], nanolithography [14], and manipulating the emission of single emitters [15].

Currently, most optical antenna research concerns planar structures on glass substrates. Due to the limitation of current nano-fabrication technology, only simple designs from the radio frequency range are considered at optical frequencies [17, 48, 49]. Figure 2.19 shows some typical antenna designs at optical frequencies. They include resonant metallic bars of various shape and size, as well as various metallic gap structures such as dimers and bow-ties.

The most promising properties of optical antennas are based on their potential to confine and enhance electromagnetic field [17, 47, 50]. When the incident plane wave illuminates optical antennas, the electromagnetic field can be confined to the vicinity of the antenna with orders of magnitude of intensity enhancement. The dimensions of localized optical fields are mainly determined by the antenna feature

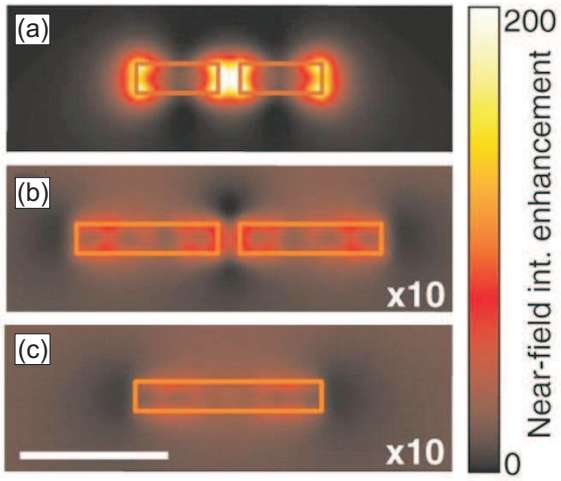

Figure 2.20: Calculated near field intensity enhancement factor of optical antennas. (a) and (c) Out of resonance. (b) at resonance. Scale bar, 200 nm [17].

size. The intensity magnitude of the field is determined by the resonance properties of the antenna. This concept was first demonstrated in the GHz range [51] and then extended into optical frequencies [52]. In GHz range, it has been shown that with a resonant bow-tie antenna, the electric field could be confined into a dimension of $\lambda/10$ with a high transmission efficiency. At optical frequencies, numerical calculations have shown that nano-dipole antennas have similar effects. As shown in Fig 2.20 (b), with a 250 nm long dipole antenna the electric field can be confined in a sub-100 nm scale in the vicinity of the antenna [17]. At the resonance wavelength of 830 nm light illumination, the field intensity is 200 times higher than that of an evanescent field in the absence of the antenna. The field enhancement is strongly resonance dependent. As depicted in Fig. 2.20 (a) and (c), out of the resonance, the field enhancement of antennas is nearly invisible.

2.5.3 Resonances of optical wire antennas

At radio frequencies, the resonance wavelengths of antennas are mainly determined by the electrical length of the antenna. Since metals behave as near perfect conductors at radio frequencies, the electrical lengths of the antennas are nearly the same as the geometric lengths of the antenna [16]. As shown in Fig. 2.21, the resonance wavelength of a dipole antenna and a loop antenna can be described as $\lambda_d = 2l$ and $\lambda_l = 2c$, respectively, where l is the length of the dipole antenna, and c the circumference of the loop antenna.

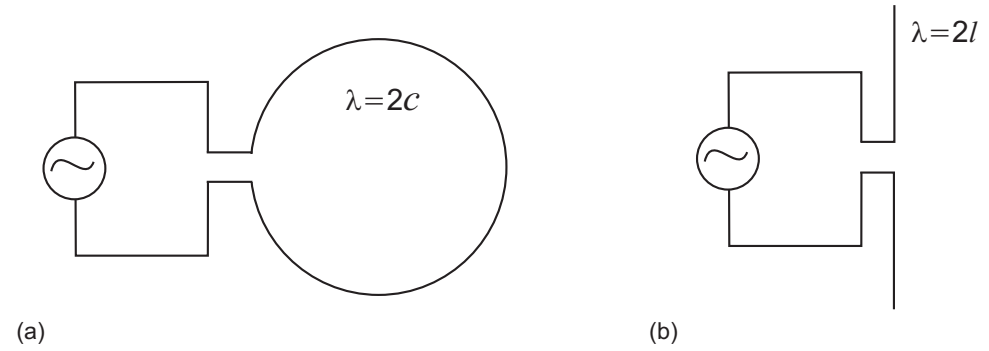

Figure 2.21: Resonance wavelengths of two basic antennas. (a) For a loop antenna, the resonance wavelength is twice of the circumference of the loop c. (b) The resonance wavelength of a dipole antenna is twice of the length of the antenna l.

At optical frequencies, the simple wavelength scaling of antennas breaks down because the properties of metals strongly deviate from that of perfect electric conductors. Experimental and theoretical studies showed that the fundamental resonance wavelength of a nano-dipole antenna is considerably longer than the double length of the antenna [17, 47, 53]. However, Novotny recently showed that the resonance wavelength of a nanorod dipole antenna can be described as a linear function of the length of the antenna, by taking the metal properties and the antenna geometry into account [49]. For simple dipole antennas that made of linear segments of a Drude model metal as shown in Fig. 2.22, an effective wavelength corresponds to the one in the radio frequency regime at $\lambda_{eff} = n_1 + n_2[\lambda/\lambda_p]$, where n_1 and n_2 are coefficients that depend on antenna geometry and material properties, and λ_p is the plasma wavelength of the metal in the Drude model. The assumption is that the antenna has a radius $R \ll \lambda$. This model has shown good agreement with numerical simulations and represented an intuitive picture for understanding the resonance behavior of optical antennas. As shown in Fig. 2.23, the resonance wavelength of the nanorod made of silver and aluminum shows a linear dependence on the length of the nanorod.

In contrast to these wire-types of antennas, slot antennas have the advantage of robustness and greater control of the radiation pattern. Moreover, slot antennas show an even stronger field enhancement when compared to the normal wire antenna. In Chapter 5, we will discuss the resonant behavior of optical slot antennas in detail.

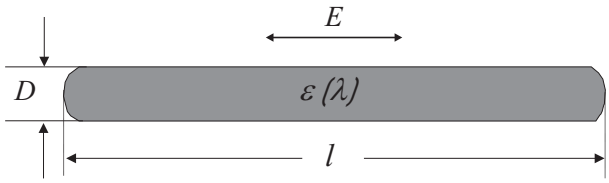

Figure 2.22: A single nanodipole antenna by a metal rod. Incident light with wavelength λ induces surface polarization. At resonance wavelength, a standing surface charge wave can be excited.

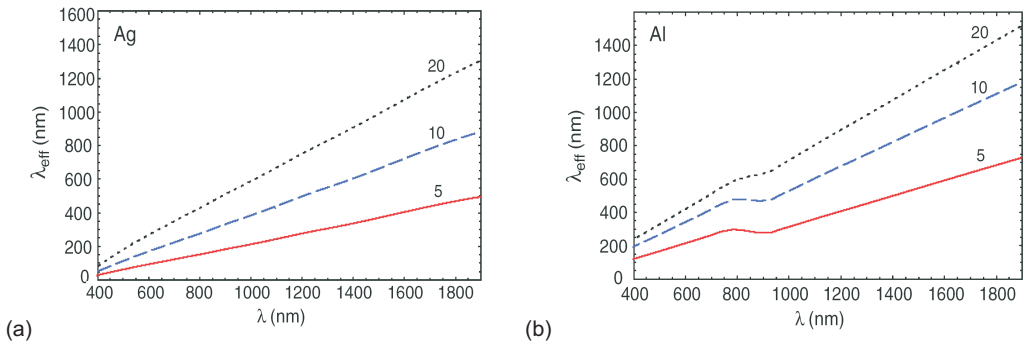

Figure 2.23: Resonance wavelength of nanorods made of silver and aluminum show a linear dependence on the length of the rod. Different curves are for the rods with different diameters [49].

3 Experimental and numerical simulation methods

In this chapter, experimental techniques related to the nano-structure fabrication in this work are described. After an overview of various fabrication techniques, an optical characterization method is introduced. We will give a short introduction to the numerical simulation method used in our work. A useful overview of nano-fabrication technologies can be found in Ref. [54].

3.1 Nanofabrication

In order to fabricate metallic nano-structures on substrates for optical characterization, several processes are need. Here we will give an introduction to thin film deposition, etching, and electron beam lithography, which are the main nano-fabrication techniques used in our work.

3.1.1 Thin film deposition

There are several methods used to deposit materials in the form of dielectric or metallic films on substrates; vacuum evaporation is the typical method used for our experiments. The principle of vacuum evaporation is simple, the substrate and the coating material are both placed in an evacuated enclosure, some distance apart. The coating material is then heated to its melting point, so that it evaporates. Sufficient thermal energy is supplied to enable individual atoms to escape from the surface of the molten material, since there are no intervening gas molecules. These atoms travel in a straight line towards the substrate where they adhere to the surface.

Several methods may be used to melt the evaporant. Fig. 3.1(a) shows the resistive heating, in which the evaporant is loaded in boat shaped crucible made of tungsten (W), through which a large dc current is passed. Many metals may be evaporated very successfully using resistive heating. However some metal evaporants

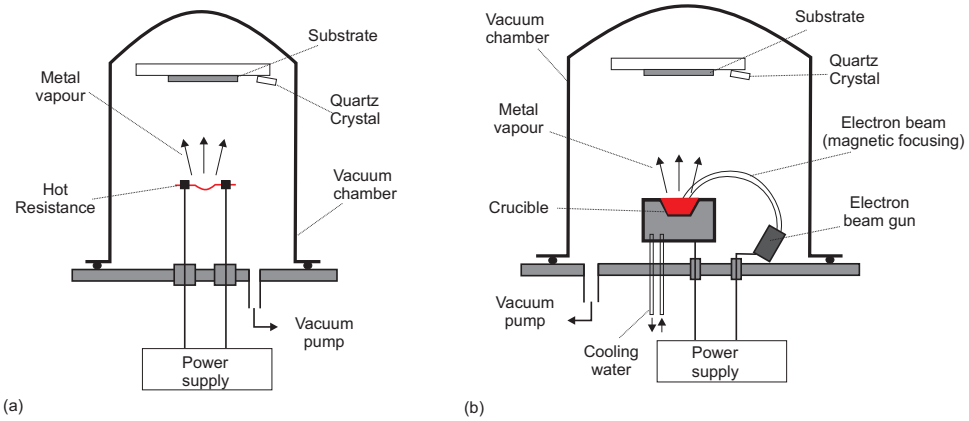

Figure 3.1: Schematic diagram of vacuum evaporators. (a) Thermal evaporator and (b) electron gun beam evaporator.

have high melting points, and are extremely reactive when molten. This may lead to the contamination of the film by impurities. Similarly, many dielectrics have even higher melting points and also very poor thermal conductivity. In this case, electron beam heating as shown in Fig. 3.1(b) could be a suitable alternative, where a hot wire filament is used as a thermionic electron emitter. A charged aperture above the filament then accelerates the electrons in the vertical direction while simultaneously limiting them to a roughly collimated beam. A magnetic field is oriented perpendicular to the direction of the electron beam, so the beam is bent into an arc and targets a water-cooled crucible containing the evaporant. Now heated by the kinetic energy of the electrons rather than by direct contact with a hot body, the problems described above are eliminated.

In the vacuum evaporator, the evacuated enclosure was held at a pressure of about 10^{-6} Torr, higher pressures result in oxide formation during the evaporation of metal films. The sample is held face down over the evaporant by a support frame, and evaporation takes place upwards. The thickness of the film is monitored by allowing the simultaneous coating of a small quartz crystal, which is arranged as a part of an oscillator circuit. Changes in the resonant frequency of the circuit may then be related to the mass-loading of the crystal, and hence to the thickness of the coating. Due to the direct flight line of atoms from the evaporant to the substrate, evaporation cannot be used to coat any features of the surface topology that lie in the shadow region.

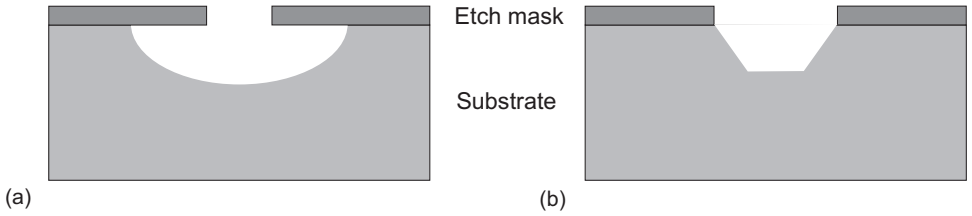

Figure 3.2: (a) Isotropic wet etching. The etchant etches the material away in all directions with the same rate. (b) Anisotropic wet etching of Si. The bottom of the cavity is a $\langle 100 \rangle$ plane and the sides are $\langle 111 \rangle$ planes.

3.1.2 Etching

In micro- and nano-fabrication, etching refers to a process by which material is removed from the substrate or from any layer of material on the substrate. There are two major types of etching processes: dry etching and wet etching.

Wet Etching is an etching process that utilizes liquid chemicals or etchants to remove materials from the wafer to transfer the specific patterns defined by photoresist masks into the substrate. Materials not covered by these masks are 'etched away' by the chemicals while those covered by the masks are left nearly intact.

Wet etching is generally isotropic, which leads to large 'under-cut' when etching thick films [Fig. 3.2(a)]. However, some wet etchants etch crystalline materials at very different rates depending upon which crystal face is exposed. In single-crystal materials, this effect can allow for very high anisotropy. As shown in Fig. 3.2(b), a cavity with a trapezoidal cross-section is created by the anisotropic wet etching on a silicon wafer. The etchant etches silicon along preferred crystallographic directions. When creating very small features in thin metal films with wet etching, one may encounter the isotropic etching problem since the undercutting will be at least equal to the film thickness.

In contrast to wet etching, *dry etching* does not utilize any liquid chemicals or etchants to remove the materials. It is generally performed in the gas phase, mostly assisted by a plasma. There are two major etching mechanisms: physical etching and chemical etching.

In physical etching, the materials are removed by momentum transfer. The impacting of incident ions on the target results in a series of collisions, and atoms from the target may be ejected. Physical etching can etch any material and is anisotropic. Typical examples of purely physical dry etching techniques are physical sputtering and ion beam etching. Figure 3.3 shows a schematic of ion beam etching (IBE) system. IBE uses an energetic, broad beam, collimated and highly directional ion

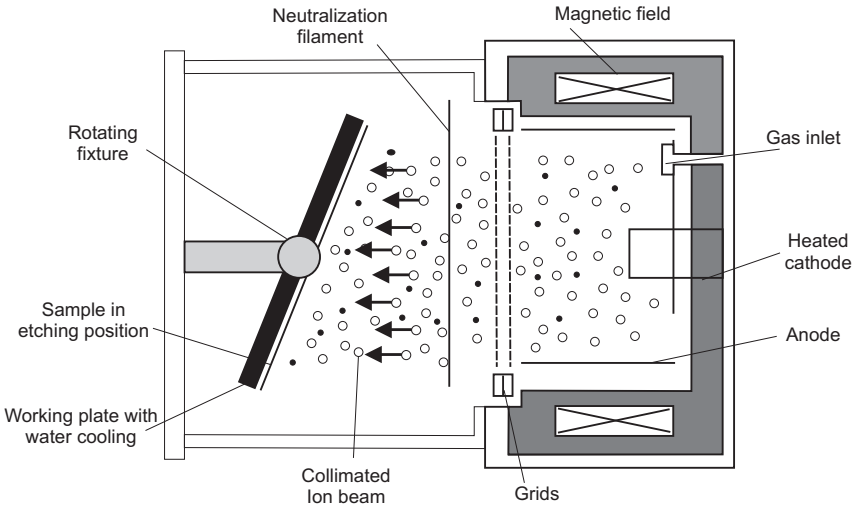

Figure 3.3: Schematic of an IBE system. Argon ions within a plasma formed by an electrical discharge are accelerated by a pair of optically aligned grids. The highly collimated beam is focused on a tilted workplate that rotates during the milling operation. A neutralization filament prevents the buildup of positive charge on the workplate. The magnetic field provides cycloidal electron path to increase ionization.

source to physically mill materials from a substrate, which is mounted on a rotating fixture with adjustable tilt angle. The ion sources used are gridded-ion sources of the Kaufman type and are typically neutralized with an independent electron source. The highly collimated, directional ion flux allows for anisotropic etching of any material. The ability to modify the angle of the substrate allows to minimize the redeposition of materials on overlying masks. Although physical etching provides a good pattern transfer with anisotropic etching, a non-erodible mask is required due to the poor selectivity. Physical etching can introduce a high degree of damage to the substrate since the process can etch 'anything'.

In chemical etching, species generated in the plasma react with the target and form volatile products. This etching mechanism is similar to wet etching and the etching is generally isotropic, which leads to a poor pattern transfer. However, chemical etching can be highly material selective with suitable choice of chemistry. Presently, plasma etching is mainly used for removing the photoresist using O_2-based plasmas.

The most commonly used method for etching is the combination of physical etching and chemical etching. A typical example of this technique is reactive ion beam etching (RIBE), which combines the purely physical character of sputtering with the chemical nature of plasma etching. With simultaneous bombardment of a substrate by both energetic ions and chemically reactive molecules or atoms, the material can

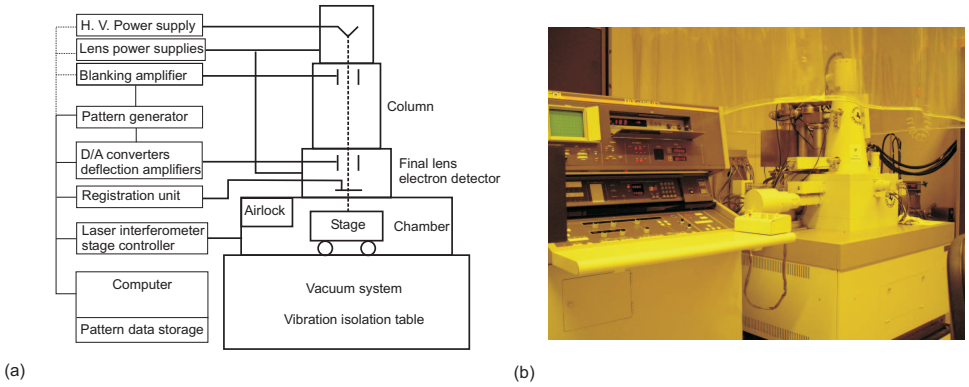

Figure 3.4: (a) A block diagram of a typical electron beam lithography. (b) The picture of JEOL JBX 5DII (U) electron beam lithography system used in our experiment.

be etched in a fast rate with anisotropic etching. RIBE is almost identical to IBE except that reactive ions are incorporated in whole or in part into the etching ion beam. This has the advantage such as high anisotropy, good pattern definition, low damage, and a high degree of good selectivity for underlying layers.

3.1.3 Electron beam lithography

Electron beam lithography (EBL) is a specialized technique for creating the extremely fine patterns often required in the modern electronics and nano-optics. This technique consists of scanning a beam of electrons across a surface covered with a sensitive resist film, thereby depositing energy in the desired pattern. Since EBL provides a high resolution and controlled design of patterns, it has become a standard method for fabricating nano-structured planar samples. Provided that bulk fabrication is not required, the disadvantage of long serial writing time does not play a significant role. Figure 3.4(a) shows a block diagram of a typical electron beam lithography tool. The column is responsible for forming and controlling the electron beam. Figure 3.4(b) shows a picture of the EBL system used in our fabrication.

In order to transfer the photoresist pattern into a metal film, lift-off or dry etching processes are used after the EBL direct writing. In our work, metallic nanostructures are obtained by e-beam lithography and a subsequent dry etching process. Figure 3.5 depicts a schematic diagram of the fabrication process. In (a), a gold film is deposited onto a quartz substrate by the electron-gun evaporation. In order to enhance the adhesion between the gold film and the substrate, a 3-nm thick

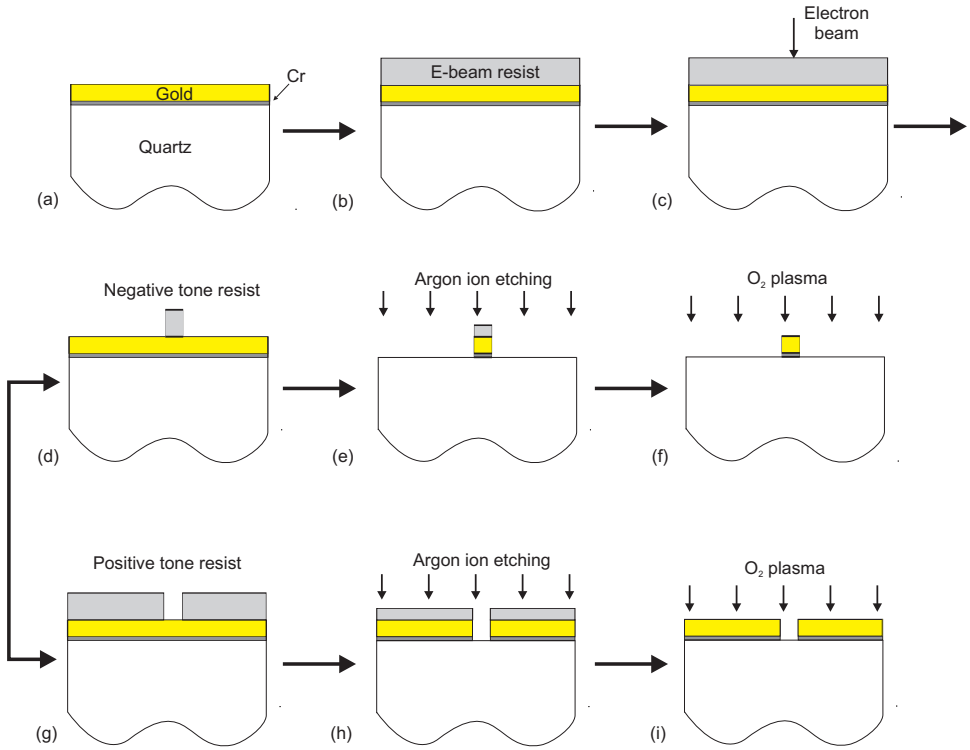

Figure 3.5: Schematic of electron beam lithography and dry-etching process. (a) Deposition of chromium and gold by the electron gun evaporation. (b) Spin coating of photoresist. (c) Pattern writing by the electron beam, (d) Photoresist development, (e) and (h) Argon ion-beam etching to remove unwanted materials, (f) and (i) Oxygen plasma treatment to remove the residual photoresist.

chromium is first evaporated on the substrate. Then, depending on the structure design, negative or positive photoresist is spin coated onto the gold coated quartz substrate, as shown in (b). The resist is exposed in the desired areas by the electron beam (c). For the negative tone photoresist, polymer chains cross-link together after the electron beam exposure, which renders them less soluble in the developer. The exposed area will stay on the substrate after the development (d). As for the positive tone photoresist, bonds in the long polymer chains are broken by the energetic electrons, which increases the solubility of these areas in a developer. The exposed area will be washed away during the development process (g). Subsequently, Ar ion-beam etching is performed [(e) and (h)] with the photoresist pattern as the etching mask. The final step is the photoresist mask removing by oxygen plasma sputtering [(f) and (i)].

When the electron beam strikes the resist, many of the electrons experience small-angle forward scattering, which tends to enlarge the initial beam size. As the elec-

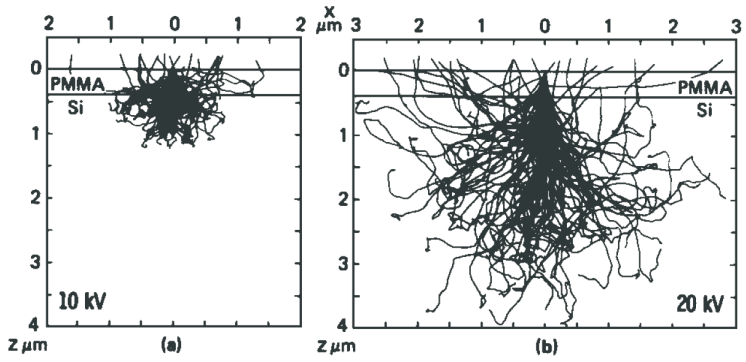

Figure 3.6: Monte Carlo simulation of free path of electron in the PMMA on Si substrate (a) at low 10 kV and (b) high 20 kV.

trons penetrate through the resist into the substrate, some of them undergo large-angle scattering events leading to backscattering, in which these electrons return back through the resist in a region far from the desired exposure. This causes additional exposure in the resist and is known as the electron beam proximity effect. During this process the electrons are continuously slowed down, producing a cascade of low voltage electrons called secondary electrons. Figure 3.6 shows Monte Carlo simulations of electron scattering in PMMA on a Si substrate [55]. The energy deposition profile in the resist can be described as the combination of forward and backscattered electron distributions and is typically modelled as a sum of two Gaussian distributions. The proximity function $f(r)$ that describes the radial distribution of energy deposition in the resist for a point exposure is given by [56]

$$f(r) = \frac{1}{\alpha^2\pi(1+\eta)}[e^{-r^2/\alpha^2} + \frac{\eta\alpha^2}{\beta^2}e^{-r^2/\beta^2}], \tag{3.1}$$

where α describes the distribution of the finite incident beam as well as the forward scattering of electrons in the resist, β accounts for the electron backscattering from the substrate, and η the parameter related to the ratio of the backscattered exposure to the forward scattering exposure. In order to compensate this proximity effect, dose-testing processes are required for the desired structure designs.

For high resolution structure fabrication, a thin photoresist film and a high acceleration voltage of the electron beam is preferred. As the split-ring resonators and bowtie slot antennas which we study in this work have sub-100 nm feature sizes, diluted photoresists are used to achieve the thin films. The acceleration voltage of the electron beam is 50 kV. For SRR structures, a negative photoresist (AR-N 7500.18, Allresist GmbH) is diluted with photoresist thinner (AR 300-12, Allresist GmbH) at a volume ratio of 1:3. A 95 nm thick photoresist is obtained at spin coating speed

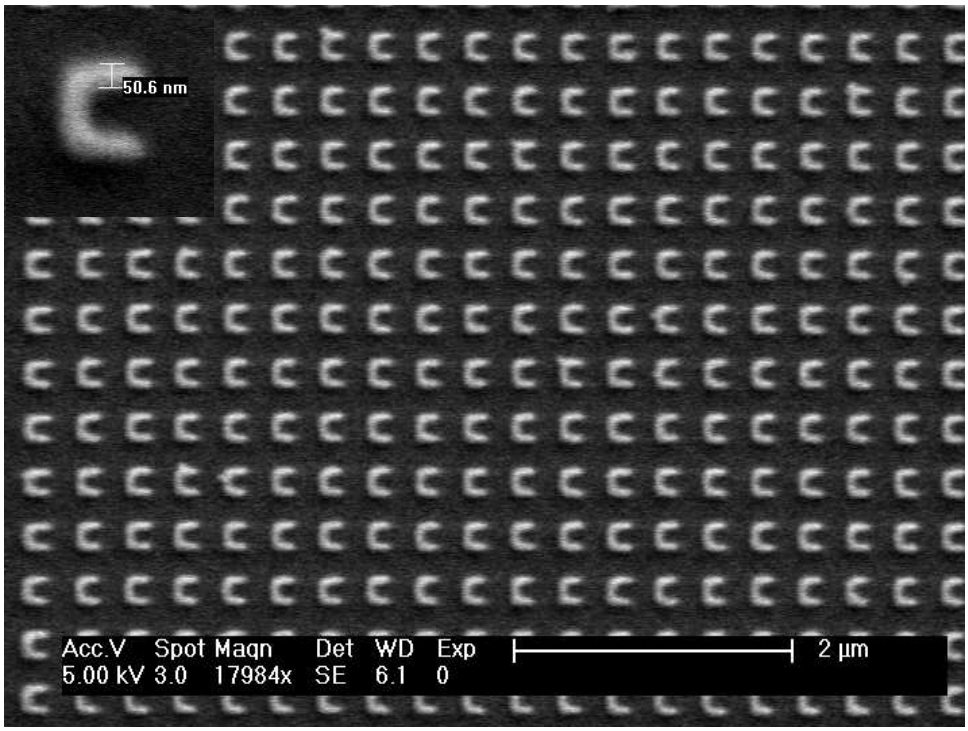

Figure 3.7: Electron micrograph of an SRR array fabricated via electron-beam lithography and subsequent dry etching. The inset shows magnified image.

7000 rpm for 45 s. The SRR structures in the photoresist films are transferred into the gold film by an Ar^+ IBE etching process. For bowtie slot antennas, we change to positive resist (poly(methylmethacrylate), commonly known as PMMA, Allresist GmbH) in order to shorten the electron beam writing time. Similarly, diluted 1.5% 950K PMMA is used for spin coating in order to get a photoresist film thickness of 100 nm. The photoresist patterns are transferred into metal films by the IBE dry etching as well. The typical structure size is around 100 μm $\times$ 100 μm for easier optical characterization. An example of a metamaterial consisting of a periodic arrangement of SRRs fabricated in our experiments is shown in Fig. 3.7.

3.2 Optical measurements

The primary instrument used for optical characterization is a commercial Fourier transform infrared spectrometer (Bruker IFS 66v/S with IR microscope). With the help of the microscope, the transmission and reflection spectra can be measured for very small areas. With various apertures in the light path, the diameter of measurement area can range from 20 μm up to 250 μm and is chosen according to

the sample size. The light source is a tungsten halogen lamp, which can be used from the visible to the near-infrared. For the shorter wavelength range (400 nm - 1.2 μm) a calcium-fluoride beam splitter and a silicon diode detector are used; for the longer wavelength regime (900 nm - 5 μm) one has to switch to a calcium-fluoride beam splitter and a liquid-nitrogen-cooled mercury cadmium tellurium (MCT) detector. A thallium bromo-iodide polarizer was used to obtain linearly polarized light in both spectral regions. The advantage of this Fourier-transform instrument lies in the broad accessible spectral range and in the possibility to characterize extremely small samples.

3.3 Numerical simulation techniques

We have used the commercial software package CST Microwave Studio [57] to numerically calculated the optical properties of metallic nano-structures. CST Microwave Studio is a general-purpose electromagnetic simulator based on the Finite Integration Technique (FIT). This numerical method provides a universal spatial discretization scheme, applicable to various electromagnetic problems ranging from static field calculations to high frequency applications in the time or frequency domain. Different from most numerical methods, FIT discretizes the following integral form of Maxwell's equations, rather than the differential forms [57]:

$$\oint_{\partial A} \overrightarrow{E} \cdot d\overrightarrow{s} = -\int_A \frac{\partial \overrightarrow{B}}{\partial t} \cdot d\overrightarrow{A} \qquad \oint_{\partial A} \overrightarrow{H} \cdot d\overrightarrow{s} = -\int_A (\frac{\partial \overrightarrow{B}}{\partial t} + \overrightarrow{J}) \cdot d\overrightarrow{A}, \tag{3.2}$$

$$\oint_{\partial V} \overrightarrow{D} \cdot d\overrightarrow{A} = -\int_A \rho dV \qquad \oint_{\partial V} \overrightarrow{B} \cdot d\overrightarrow{A} = 0. \tag{3.3}$$

These equations are numerically solved by defining a finite calculation domain, which is split up into several small grid cells by creating a suitable mesh system. Generally, the simulations are done in Cartesian grids. In order to increase the accuracy in modelling of complex boundaries, a PBA (Perfect Boundary Approximation) technique is applied to the FITD algorithm, which maintains all the advantages of structured Cartesian grids and allows an accurate modelling of curved structures. Figure 3.8 shows the comparison of three geometric discretizations. One can see that the FIT model together with the PBA theory combines the advantages of the Finite Element Method (FEM) model and the FDTD/TLM model. It offers both an excellent geometric approximation and a high simulation speed, but without the segmentation of FE models or staircase approximation of FDTD codes.

Three different types solvers are available concerning high frequency electromag-

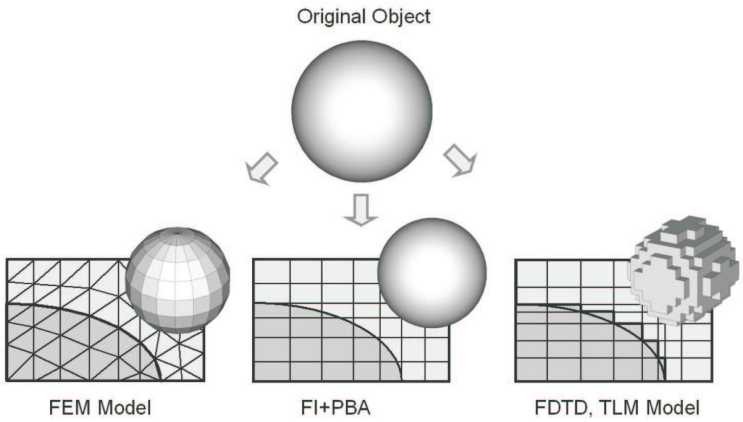

Figure 3.8: Geometry discretizations in numerical simulation by FEM, FI+PBA, and FDTD/TLM models.

netic field problems: transient, frequency domain, and eigenmode solver. In this work, the numerical simulations are done with transient solver, which allows for the simulation of the behavior of a structure in a wide frequency range in just a single computational run. In order to calculate the reflectance and transmittance of metallic nano-structures with the transient solver, we apply the 'waveguide' boundary condition, under which the tangential component of either the E-field or the H-field are set to zero at opposite boundaries, and additionally the polarization is defined. The single element of the metallic nano-structures is placed into this rectangular waveguide. In the propagation direction the waveguide has open boundary conditions and is terminated with input and output ports. The waveguide is excited with an eigenmode at the position of one port, and the amplitude and the phase of the transmitted and reflected part of the eigenmode are calculated after propagation through the waveguide. The permittivities of the composed materials of the nano-structure and the substrate are given individually. The results are the S-parameter amplitude and phase for transmittance and reflectance. Field distributions for E and H at fixed frequencies can be recorded during the S-parameter simulation process.

The simulations with the waveguide boundary condition show good agreement with the experimental measurements for periodically arranged nano-structures [10, 12, 58]. In order to obtain the optical properties of individual elements, the interaction between the neighbor units has to be considered. Moreover, for structures with periods comparable to the resonance wavelength, the waveguide boundary condition may introduce some artificial features.

3.4 Dielectric constants of metals in the optical regime

In order to calculate the optical properties of metallic nano-structures by the numerical simulation tools, physical models have to be applied to the dielectric constants of metals. In our simulations by the FITD algorithm, the frequency dependent dielectric functions of metals in the near infrared and visible range are described by the Drude model. It offers a good correspondence to the measured data over a broad spectral range. Table 3.1 shows the ω_p and γ by fitting the Drude model to the experimentally obtained data of Ref. [59].

Table 3.1: Plasma frequency and damping frequency of various metals [59]

Metal	Ag	Au	Cu	Al	W
Plasma frequency ($\times 2\pi$ THz)	2175	2175	1914	3570	1452
Damping frequency ($\times 2\pi$ THz)	4.35	6.5	8.34	19.4	12.99

4 Plasmonic resonances of split-ring resonators

When the dimensions of metallic nano-structures are smaller than the optical wavelength, plasmonic resonances can be excited by external light illumination. This makes these structures promising for chemical and biosensing applications, surface enhanced Raman spectroscopy applications, etc. [4] Recently it has been demonstrated that the resonance of metallic split ring resonators (SRRs) can be utilized in creating a magnetic response in metamaterials showing a negative permeability [10, 60]. In this chapter, we will first give a short introduction of split-ring resonator metamaterials and a model to describe their resonance behavior, namely a quasi-static LC circuit model. The thickness dependence of the resonances of SRRs will subsequently be demonstrated experimentally and numerically. In order to explain our observations, an equivalent cut-wire model is introduced based on the plasmonic explanation of the resonances of SRRs. In the final section, we analyze the resonance behavior of double split-ring resonators by combining a hybridization concept with the plasmonic model.

4.1 Introduction

The optical response of materials are generally described by two parameters: permittivity and permeability. For most naturally occurring materials, their optical properties are generally modelled by the Lorentz model, in which the electrons and ions of the matter were treated as simple harmonic oscillators, and the magnetic permeability is assumed to be unity [28, 61]. However, theoretical studies have indicated that materials with simultaneous negative permittivity and permeability may exhibit certain unique properties such as negative refraction [62] and subwavelength focusing [63]. In order to explore the fascinating properties, artificially created materials with the desired permittivity and permeability have been designed [64, 65]. These artificial materials, a collection of repeated building elements, can provide a

strong response to the applied electromagnetic fields. In the case that the size and spacing of the elements are much smaller than the electromagnetic wavelengths of interest, the material can be treated as a homogeneous medium described by effective material parameters ϵ and μ. This type of composite materials are named 'metamaterials', and their building elements, in analogy of the atoms in solids, are called 'artificial atoms'.

Based on the Drude-Lorentz model, metamaterials with negative permittivity can be achieved by designing the elements resonant to the electric field at desired frequencies. Typical negative permittivity metamaterials are composed of cut-wires or metallic nanoparticles, their effective permittivity has the form [64]

$$\epsilon(\omega) = 1 + \frac{\omega_{ep}^2}{(\omega_{e0}^2 - \omega^2) + i\gamma_e\omega}, \tag{4.1}$$

where ω_{ep} is the electric plasma frequency, ω_{e0} the resonance frequency, and γ_e the damping frequency of the material. In the frequency range $\omega_{e0} < \omega < \omega_{ep}$, the permittivity is negative. The resonance frequency ω_{e0} is mainly determined by the geometry of the metallic structures. By varying the designs, negative permittivity was achieved at frequencies ranging from a few Megahertz to optical frequencies.

The method for obtaining a magnetic response from conductors is somewhat different. With the basic definition of a magnetic dipole moment $m = 1/2 \int r \times j d^3r$ for the current density j, magnetic resonances can be obtained when local currents are driven to circulate in closed loops. Introducing a resonance into such an element may lead to a strong magnetic response, which can potentially result in a negative permeability. Following this principle, magnetic metamaterials were proposed and demonstrated in the microwave regime by using double split-ring resonators as shown schematically in Fig. 4.1(a), which consists of conduction loops with a gap [60, 65]. Such a split-ring resonator can be viewed as a miniature circuit. A time-varying magnetic field drives a circulating current within the conductor. The gap in the SRR introduces capacitance into the circuit and gives rise to a resonance at a frequency ω_0, which is set by the geometry of the SRR. Analogous to the Lorentz model for solids, one can view an SRR as the metamaterial equivalent of a magnetic atom. The magnetic response of the SRR medium can be described by the form

$$\mu(\omega) = 1 + \frac{\omega_{mp}^2}{(\omega_{m0}^2 - \omega^2) + i\gamma_m\omega}, \tag{4.2}$$

where ω_{mp} is the magnetic plasma frequency for the SRR medium, γ_m the damping frequency, and ω_{m0} the resonance frequency. Figure 4.1(b) shows the schematic

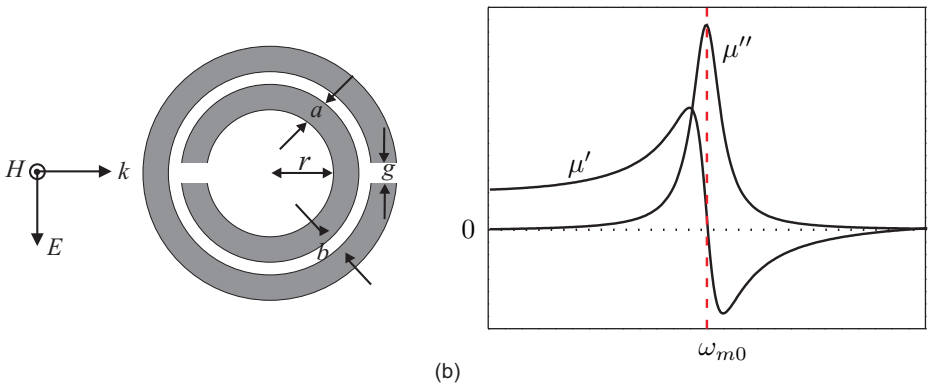

Figure 4.1: (a) Schematic of a split-ring resonator. (b) The permeability of the SRR medium near the resonance frequency ω_{m0}.

variation of μ' and μ'' with frequency for the SRR medium. In the frequency range $\omega_{m0} < \omega < \omega_{mp}$, the negative permeability is achieved.

By combining the metallic wires and split-ring resonators, the first negative refractive index metamaterials were demonstrated in the microwave regime [60, 66]. Since negative permittivity can be achieved at multiple spectral positions ranging from the microwave frequency to the optical frequency, most efforts have been paid to design metamaterial elements with negative permeability at specific frequencies [10, 67, 68, 69].

4.2 Quasi-static LC circuit model of the SRR

The working principle of an SRR is often understood in terms of electrical engineering. The gap of the SRR can be viewed as a capacitance, and the ring as a single winding of an inductance loop. Both together constitute an LC-circuit, which can be coupled to an external light field. When the magnetic field of the incident light oscillates perpendicularly to the SRR plane as shown in Fig. 4.2(a), the LC oscillator resonates with the incident light around its eigenfrequency $\omega_0 = 1/\sqrt{LC}$. A resonance of the effective permeability can therefore be obtained [10, 60].

In optical frequencies, the LC resonance of an SRR is often driven by the electric field of the incident light, which is polarized parallel to the gap-bearing side of the SRR as shown in Fig 4.2(b) [70]. To probe the spectral position of this resonance, the SRR can be illuminated at normal incidence.

The schematic view of a metallic split-ring resonator and the analogy of a conventional LC circuit are shown in Fig. 4.3. Based on the geometrically idealized

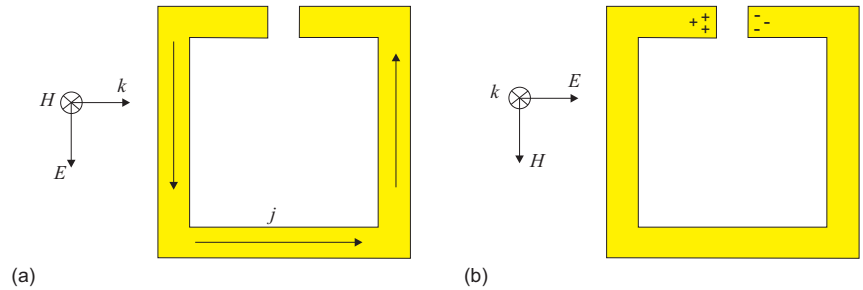

Figure 4.2: The LC resonance of an SRR can be excited when the magnetic field of the incident light is perpendicular to the SRR plane (a) or when the electric field of the incident light is parallel to the gap-bearing side of the SRR (b).

and quasi-static formulas for the capacitance of a parallel plate capacitor and the inductance of a solenoid, the capacitance and inductance of a single SRR can be estimated using the following equations [12]:

$$C = \varepsilon_0 \epsilon_{eff} \frac{wt}{d} \tag{4.3}$$

and

$$L = \mu_0 \frac{l_x l_y}{t}, \tag{4.4}$$

where ϵ_{eff} is the effective dielectric constant of the medium in the gap. ϵ_{eff} has a value between ϵ_{air} and ϵ_{sub}, since the electric field is not confined only to the gap space itself. Thus, one can estimate the resonance frequency of an SRR as follows:

$$\omega_{LC} = \frac{1}{\sqrt{LC}} = \frac{c}{\sqrt{\epsilon_{eff}}} \frac{1}{\sqrt{l_x l_y}} \sqrt{\frac{d}{w}} \propto \frac{1}{\sqrt{area}}. \tag{4.5}$$

The resonance wavelength of the LC resonance can be written as:

$$\lambda_{LC} = 2\pi \sqrt{\epsilon_{eff}} \sqrt{l_x l_y} \sqrt{\frac{w}{d}} \propto \sqrt{area}. \tag{4.6}$$

The quasi-static LC circuit model describes the size scaling-down effect as well as the gap size, the arm length, and the notch depth effect on the resonance frequencies of SRRs [58, 68, 71]. Following this approximation, it has been demonstrated that higher LC resonance frequencies of SRRs can be achieved by increasing the gap size, reducing the arm length, and reducing the notch depth [12]. However, this model suggests a independence of the resonance on the metal thickness. Metals are a high

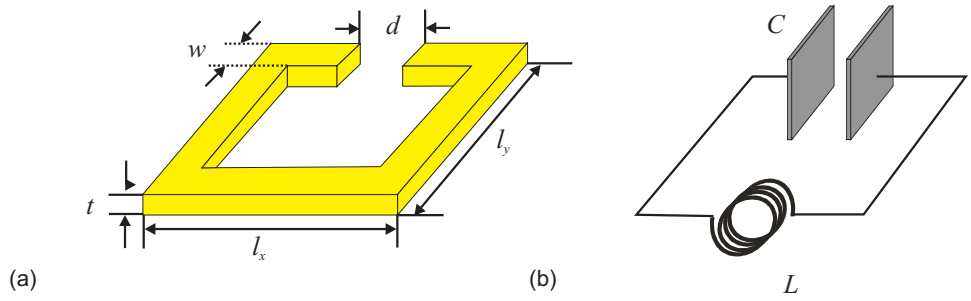

Figure 4.3: (a) Schematic diagram of an SRR. The geometry of the SRR is defined by the thickness of the SRR t, the gap size d, the width of the wire w, the length of the wire parallel to the gap bearing side l_x, and the length of the wire perpendicular to the gap bearing side l_y. (b) A conventional LC circuit.

absorptive medium in the optical regime, and the electromagnetic fields are only confined near the metal surface within several tens of nanometers [4]. Therefore, the metal thickness will play a role in determining the resonances of SRRs in the optical frequency range.

4.3 Experimental results

In order to investigate the thickness influence on the resonances of SRRs, the SRR arrays are fabricated on a quartz substrate with e-beam lithography and and subsequent ion beam etching. For easier fabrication, SRRs are U-shaped as schematically shown in Fig. 4.4, where the geometry of an SRR is defined by the thickness of gold t, the width of the gold wire w, the length of the wire parallel to the gap l_x (base-wire), and the length of the wire perpendicular to the gap l_y (arm-wire). Three samples with thicknesses of $t = 10$ nm, 40 nm, and 60 nm are fabricated. Figure 4.5 shows the scanning electron microscope (SEM) images of the SRR samples in top view. The SRRs have a geometry of $l_x = 410$ nm, $l_y = 350$ nm, $w = 100$ nm.

The measured transmission and reflection spectra of samples of the three different thicknesses are shown in Fig. 4.6. The numerical simulation results by the FITD algorithm are plotted in the same figure for comparison. Due to the additional scattering of electrons resulting from the metal surface in the thin gold film, the simulation used a damping frequency of gold at a value 3 times larger as in bulk [10]. This increases the absorption and leads to a better agreement with experimental data. The experimental results show a good agreement with the numerical

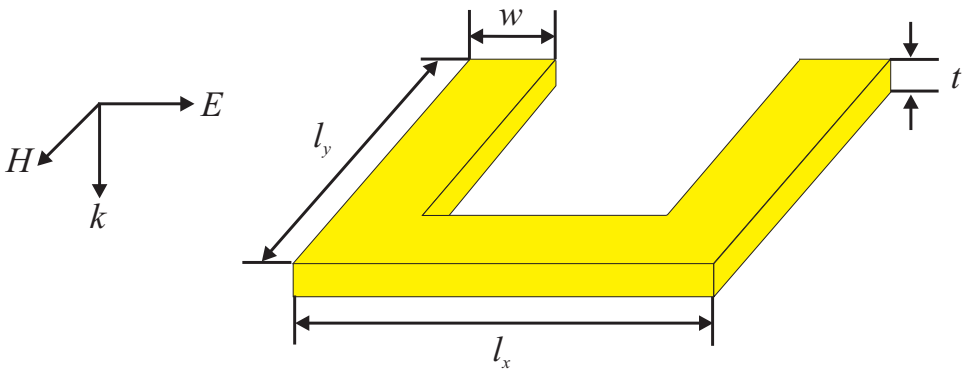

Figure 4.4: Schematic diagram of a U-shaped gold SRR. The SRR geometry is defined by the thickness of gold t, the width of the gold wire w, the length of the wire parallel to the gap l_x (base-wire), and the length of the wire perpendicular to the gap l_y (arm-wire).

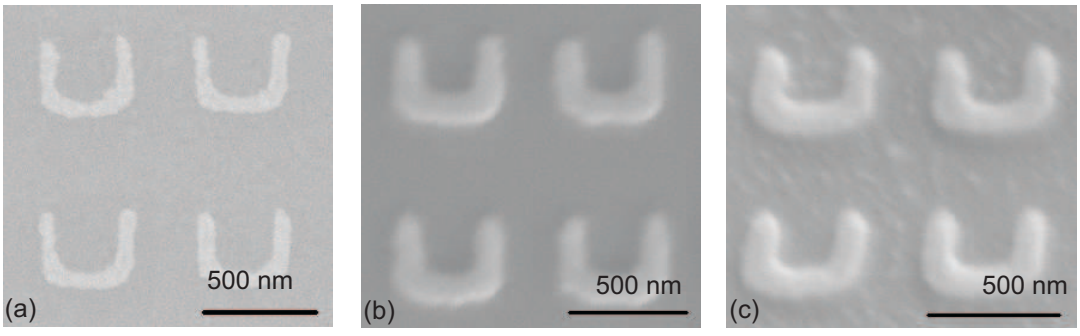

Figure 4.5: SEM images of gold SRR structures in various gold thicknesses. (a) $t =$ 10 nm. (b) $t = 40$ nm. (a) $t = 60$ nm.

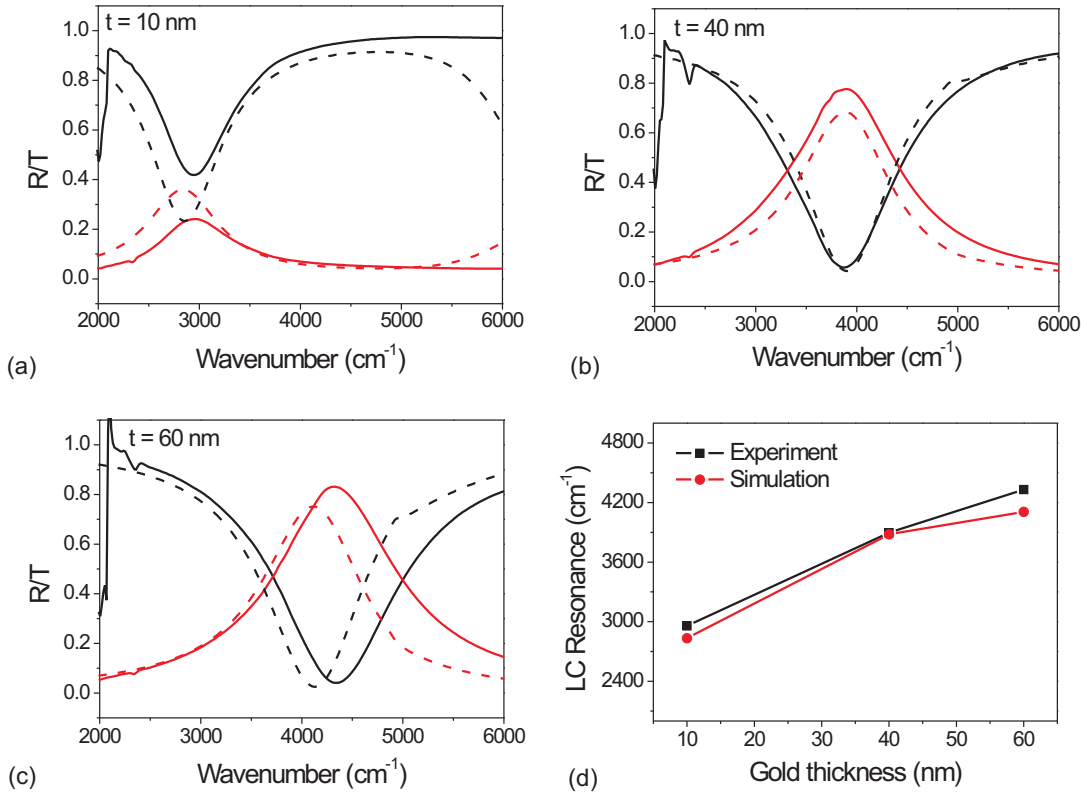

Figure 4.6: Measured (solid curves)and calculated (dashed curves) transmission (black) and reflection (red) spectra of SRRs with various gold thicknesses: (a) 10 nm, (b) 40 nm, and (c) 60 nm. (d) *LC* resonance frequency of SRRs as a function of the gold thickness. The increased gold thickness shifts the *LC* resonance to higher frequencies. Squares are experimental data and solid circles are simulation data.

simulations. The slight deviation between experiment and numerical simulation is from the non-perfect structure fabrication as shown in SEM images. Actually when the variations in wire width and arm length are taken into account in the numerical simulation, an even better agreement could be achieved. Considering that our investigations focus on the thickness influence on SRR resonance, only the thickness of gold was used as the tuning parameter for numerical simulation.

The *LC* resonance frequencies extracted from Fig. 4.6(a)-(c) are plotted as a function of gold thickness as shown in Fig. 4.6(d). Clearly, the increased gold thickness shifts the LC resonance of the SRR to a higher frequency. However, the thickness dependence of the resonance of the SRR has not been taken into account in the quasi-static LC circuit model.

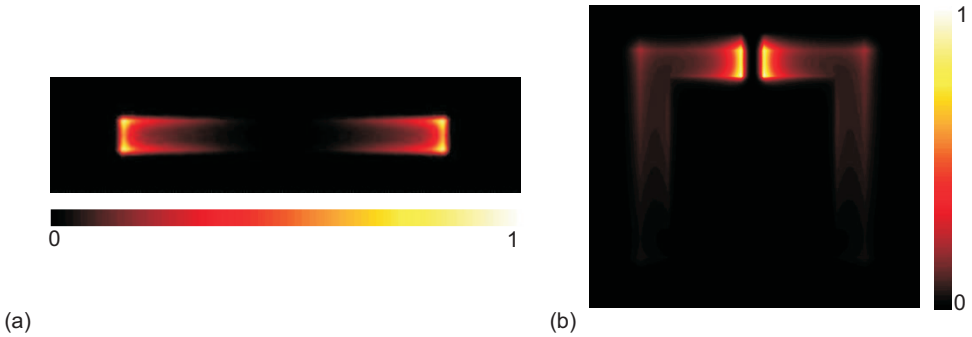

Figure 4.7: (a) Electric maximum peak field distribution of a metal cut-wire at resonance. (b) Electric maximum peak field distribution of an SRR at resonance.

4.4 Plasmonic model of the SRR

The resonances of metallic nano-structures are generally described as plasmonic resonances. Recently, a localized surface plasmon excitation picture has been applied to interpret the resonances of SRRs [72]. For a metallic cut-wire, a dipole-like charge distribution can be excited at the resonance frequency, which induces a standing surface wave along the wire. Figure 4.7(a) is the corresponding electric field distribution of a metallic cut-wire at resonance. From the plasmonic point of view, the resonance frequency of the cut-wire is determined by the restoring force between the induced surface charges [4].

At resonance, an SRR has the equivalent dipole charge distribution as a metallic cut-wire if one regards the SRR as a folded metal wire. Figure 4.7(b) shows the electric field distribution of an SRR, in which the charges with opposite signs are accumulated at the each end of the SRR. Under the excitation of a time-varying field, an oscillating current along the wire can be induced. In analogy, the LC resonances of SRRs can be understood as the plasmonic dipole resonances of metallic cut-wires.

4.4.1 Resonances of cut-wires and SRRs

In quasi-static regime, a cut-wire can be approximated as an ellipsoidal particle. The increase of the thickness in cut-wires is equivalent to an increase of the aspect ratio in ellipsoidal particles, which corresponds a blue shift of the resonance of the nano-particle [4, 73]. From the plasmonic point of view, the resonances of cut-wires shift to higher frequencies with increased metal thicknesses. Figure 4.8(a) shows the numerically calculated resonance frequencies of cut-wires as a function of the gold thickness, which shows a good agreement with the prediction from the

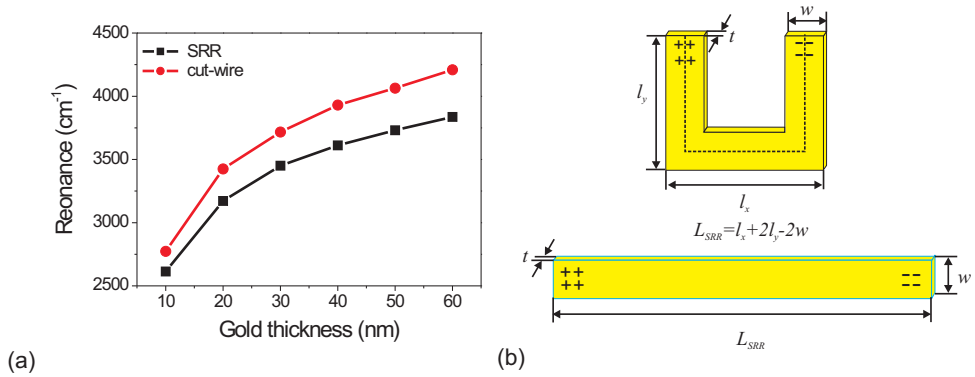

Figure 4.8: (a) Resonance frequencies of SRRs and cut-wires with the same total wire length as functions of the thickness of gold. The geometry of the SRR is defined as $l_x = 410$ nm, $l_y = 350$ nm, $w = 100$ nm.(b) Schematic diagrams showing the total wire length of the SRR and cut-wire.

plasmonic model. For comparison, the resonance frequencies of SRRs as function of the thickness are also plotted in Figure 4.8(a). The SRR and the cut-wire show a similar dependence on the thickness of the gold. In numerical simulations, the same lengths are taken for the SRR and the cut-wire as schematically shown in Fig. 4.8(b).

For each thickness, the resonance of the SRR appears at a lower frequency compared with that of a cut-wire with the same length as shown in Fig. 4.8(a). This can be understood from the plasmonic point of view as well. In the plasmonic model, the resonance frequency of a metallic nano-particle is determined by the restoring force due to the Coulomb interaction between the polarized charges. This restoring force is influenced by both the oscillation path length of the conduction electrons and the charge distribution. For the SRR and the cut-wire with the same total length, although they have the same oscillation path length of the conduction electrons, the folded arms in the SRR modify the charge distribution. This leads to a reduced restoring force as compared to the case of the cut-wire with the same total wire length, because of the attractive interaction between the charges in the arms of the SRR.

4.4.2 Cut-wire equivalents of SRRs

We have shown that SRRs showed a similar resonance dependence on the metal thickness as the cut-wires. In this section, we will show that the resonance frequency of an SRR can be quantitatively described by that of a cut-wire with an equivalent

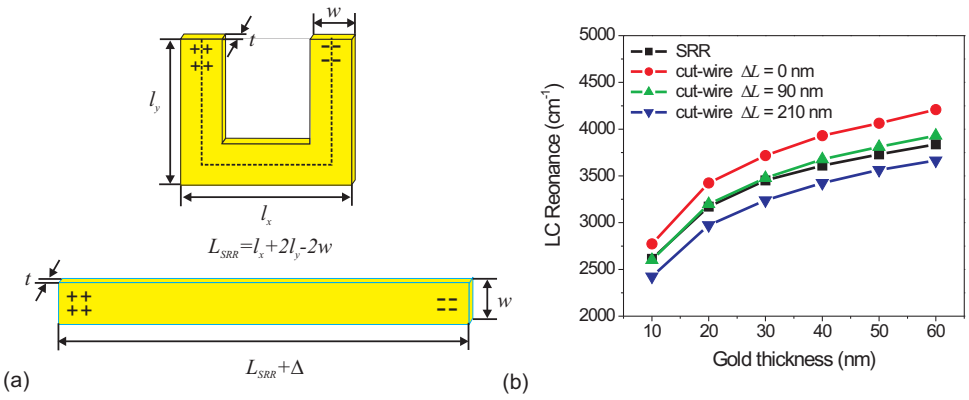

Figure 4.9: (a) Resonances of cut-wires with various correction lengths as function of the thickness. (b) Schematic of an SRR and its equivalent cut-wire.

geometry. Namely, the SRR with the total length L_{SRR} resonates at the same frequency as an cut-wire with an equivalent total wire length L_{wire}, and $L_{wire} = L_{SRR} + \Delta L$, as shown in Fig. 4.9(a). By introducing the correction length ΔL, the restoring force difference between the SRR and the cut-wire is compensated. As shown in Fig. 4.9, the resonance frequency of the cut-wire can be tuned by changing the correction length ΔL. The length of the cut-wire with ΔL= 210 nm corresponds to the outer peripheral length of the SRR as $L = l_x + 2l_y$. The resonances of the cut-wires with a length of L_{wire} = 1000 nm (ΔL = 90 nm) show a good agreement with the SRR for all the thicknesses.

To validate this equivalent cut-wire model, the resonance behavior of a series of SRRs with various arm-wire lengths is studied. The schematic diagrams of example structures are shown in Fig. 4.10. The geometry of the SRR in (a) is w = 100 nm, t = 20 nm, l_x = 400 nm, and l_y = 400 nm. Δ is the tuning length in arm-wire and base-wire as marked in Fig. 4.10(b). The marked dashed lines show the total structure length. ΔL is a correction length introduced during the SRR form change so that all SRRs resonate at the same frequency.

Fig. 4.11 (a) and (b) show the simulated resonances of the series of SRRs at various values of Δ with ΔL = 0 and ΔL = $\Delta/2$, respectively. With increased base-wire length (large Δ), the resonance frequencies of SRRs shift to the higher energy when they have the same total wire length. This is consistent with the plasmonic resonance interpretation if we consider the Coulomb interaction between arm charges of the SRR. In particular, the increased base-wire length weakens the Coulomb interaction, and increases the restoring force of the charge oscillation in

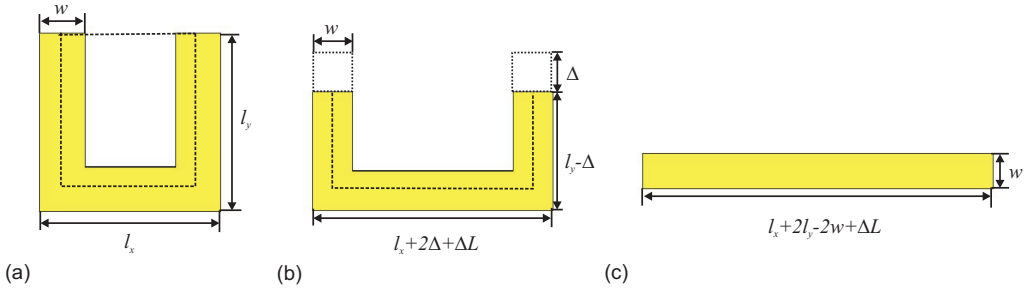

Figure 4.10: Series of SRR structures with the same total length $L = l_x + 2l_y - 2w + \Delta L$. Δ is the tuning length in arm-wire and base-wire and ΔL is the correction length. a), b), and c) represent SRRs for $\Delta L = 0$ nm, $\Delta = 0$, 100, and 300 nm, respectively.

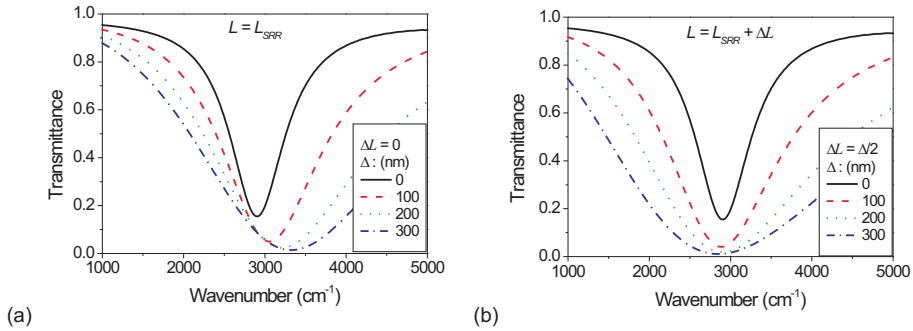

Figure 4.11: Simulated transmssion spectra for the series of the equivalent SRRs. a) All the SRRs have the same total length and with a tuning length of Δ from 0 to 300 nm at a step of 100 nm. b) Additionally to a), a correction length $\Delta L = \Delta/2$ is introduced to the total length of SRR.

an SRR. Therefore, the SRR with a long base-wire length (large Δ) resonates at a higher frequency. However, as shown in Fig. 4.11 (b), all the SRRs with various values of Δ oscillate at the same frequency if a proper correction value $\Delta L = \Delta/2$ is taken into account when changing the shape of the SRRs. This correction is between 0 and $2w$, which is reasonable considering that we use the marked dashed line as the total length of the SRR.

The linewidth broadening of the SRR resonances with increased Δ in Fig. 4.11 is due to a higher radiative loss in the SRR with a longer base-wire length. It is clear that a more elongated structure has a more dipole-like character. Therefore a long base-wire SRR (large Δ) exhibits a strong oscillator strength and hence a broader radiative linewidth when considering both a single dipole interacting with

the radiation field as well as dipole-dipole interaction.

4.5 Plasmon hybridization in double split-ring resonators

In the microwave regime, negative permeabilities have been achieved in double split ring resonators (DSRRs) near their resonances [60]. The role of the inner ring has been discussed as a reduction of the resonance frequency by increasing the gap capacitance of the outer ring [60, 74]. Recently, it has been demonstrated that the resonances of a DSRR in the near infrared regime are a linear superposition of those of its constitute outer ring and inner ring [75]. However, the role of the inner-ring in the DSRR is not clear yet. Our experimental and numerical results have shown that the plasmonic model describes well the resonance behavior of SRRs in the optical regime. With the equivalent cut-wire approximation, one can estimate the resonance wavelength with the total length of the SRR, which provides an intuitive picture for designing SRRs with specific resonance properties. In order to provide a guide for designing and optimizing metamaterials, we analyze the resonance properties of a DSRR with the plasmon hybridization method based on the plasmonic model.

4.5.1 Plasmon hybridization

The plasmon hybridization method, which is an electromagnetic analogy of molecular orbital theory, has been proposed to describe the optical responses of complex nano-structures [76]. Recently, this concept has been applied to explain the optical properties of stacked metamaterials [77]. A DSRR can be viewed as a complex metallic structure which is comparable to nanoshells [76] and nanorice [78]. Considering that the optical responses of individual SRRs can be regarded as fundamental plasmonic resonances of metallic nano-structures, the response of a DSRR can be analogously explained as a hybridization interaction between the plasmons of the constitute inner ring and outer ring. The concept is illustrated in Fig. 4.12 for a closely arranged DSRR. The resonances of the outer and inner rings alone are excited at the frequencies ω_1 and ω_2, which correspond to the plasmonic eigenmodes $|\omega_1\rangle$ and $|\omega_2\rangle$, respectively. The interaction between these plasmons results in a new coupled mode pair due to the plasmon hybridization. The modes at lower and higher energies correspond to an anti-symmetric plasmon mode $|\omega_-\rangle$ and a symmetric plasmon mode $|\omega_+\rangle$, respectively.

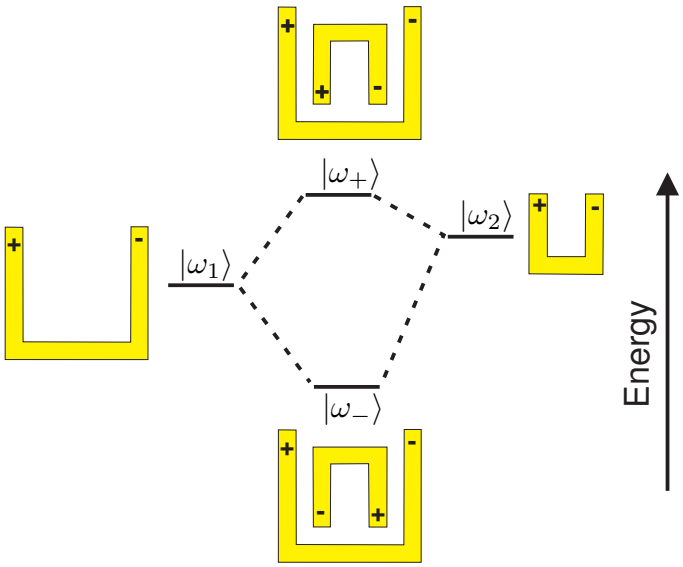

Figure 4.12: The energy diagram describes the plasmon hybridization in a DSRR. The interaction between the plasmonic modes ($|\omega_1\rangle$ and $|\omega_2\rangle$) of its constitute outer ring and inner rings results in a new coupled mode pair: an anti-symmetric mode $|\omega_-\rangle$ and a symmetric mode $|\omega_+\rangle$.

4.5.2 Coupling strength dependence on geometry

A schematic diagram of a DSRR is shown in Fig. 4.13. In order to investigate the interaction between the outer and inner rings in DSRRs, the outer-ring geometry is kept constant, whereas the geometry of the inner ring is varied. As the plasmonic eigenmode of an SRR depends strongly on its geometric length ($L = l_x + 2l_y - 2w$), the varied geometry of the inner ring leads to a resonant energy shift. A finite-integration time-domain algorithm (CST microwave studio) was used to simulate the resonant response of SRRs due to its ability to provide reliable results. The DSRRs are composed of gold and arranged in a square lattice on a quartz substrate ($n = 1.45$). The permittivity of the gold is described by a Drude model. The incident light with the polarization parallel to the gap-bearing side of the SRR is used to excite the plasmon eigenmodes of SRRs.

Figures 4.14(a)-(c) show the simulated reflectance spectra of DSRRs with various inner-ring geometries. The spectra of outer and inner rings alone are also given for comparison. In the spectra, only the resonances below 700 meV correspond to the fundamental plasmonic eigenmodes (namely, LC resonances) of SRRs, whereas the resonances above 700 meV correspond to the higher-order plasmonic modes of SRRs. In order to investigate the LC resonance properties of DSRRs, we focus our

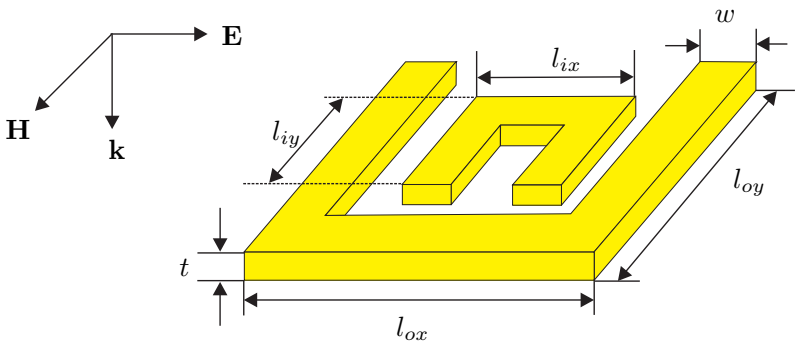

Figure 4.13: Schematic diagram of a DSRR. t denotes the thickness of the SRR, w the width of the wire, l_{ox} (l_{ix}) the length of the wire parallel to the gap bearing side in the outer (inner) ring, and l_{oy} (l_{iy}) the length of the wire perpendicular to the gap bearing side in the outer (inner) ring.

discussion on the resonance modes below 700 meV. For explanation of the simulation results, we use the following notation for our discussion: the plasmonic modes of the outer and inner rings alone are denoted by $|\omega_1\rangle$ and $|\omega_2\rangle$, respectively. Note that $|\omega_1\rangle$ is unchanged in each plot due to the fixed geometry, whereas $|\omega_2\rangle$ is shifted to higher energies with a decreased ring length. The new plasmonic eigenmodes of DSRRs at the lower and higher energies are denoted by $|\omega_-\rangle$ and $|\omega_+\rangle$, respectively.

In Fig. 4.14(a), the outer and inner rings are closely arranged in the DSRR and the spacing between them is small (20 nm). Since the total wire length difference between the outer and inner rings is 320 nm, the plasmonic eigenmodes of the outer and inner rings alone are closely spaced in the spectrum (at 123 meV distance). Due to the strong coupling between them, the plasmon hybridization induces a large plasmon energy shift of 83 meV (plasmon energy shift $\Delta E = ||\omega_+\rangle - |\omega_-\rangle| - ||\omega_2\rangle - |\omega_1\rangle|$). In this strong coupling regime, the strong interaction between the higher-order plasmonic modes of the outer and inner rings shifts the symmetric mode $|\omega_+\rangle$ to an energy level lower than $|\omega_2\rangle$. Fig. 4.14(b) shows the reflectance spectrum of a DSRR with reduced inner-ring size. The distance and total wire length difference between the outer and inner rings are increased to 50 nm and 500 nm, respectively. In this case, the plasmonic eigenmodes of the outer and inner rings alone are more detuned from one another (at 209 meV distance). Due to the weaker coupling, only a slight plasmon energy shift of 53 meV is observed. Fig. 4.14(c) shows the results for an even further reduced inner-ring size. The distance and total wire length difference between the outer and inner rings are increased to 80 nm and 680 nm, respectively. The resonances of the outer and inner rings alone

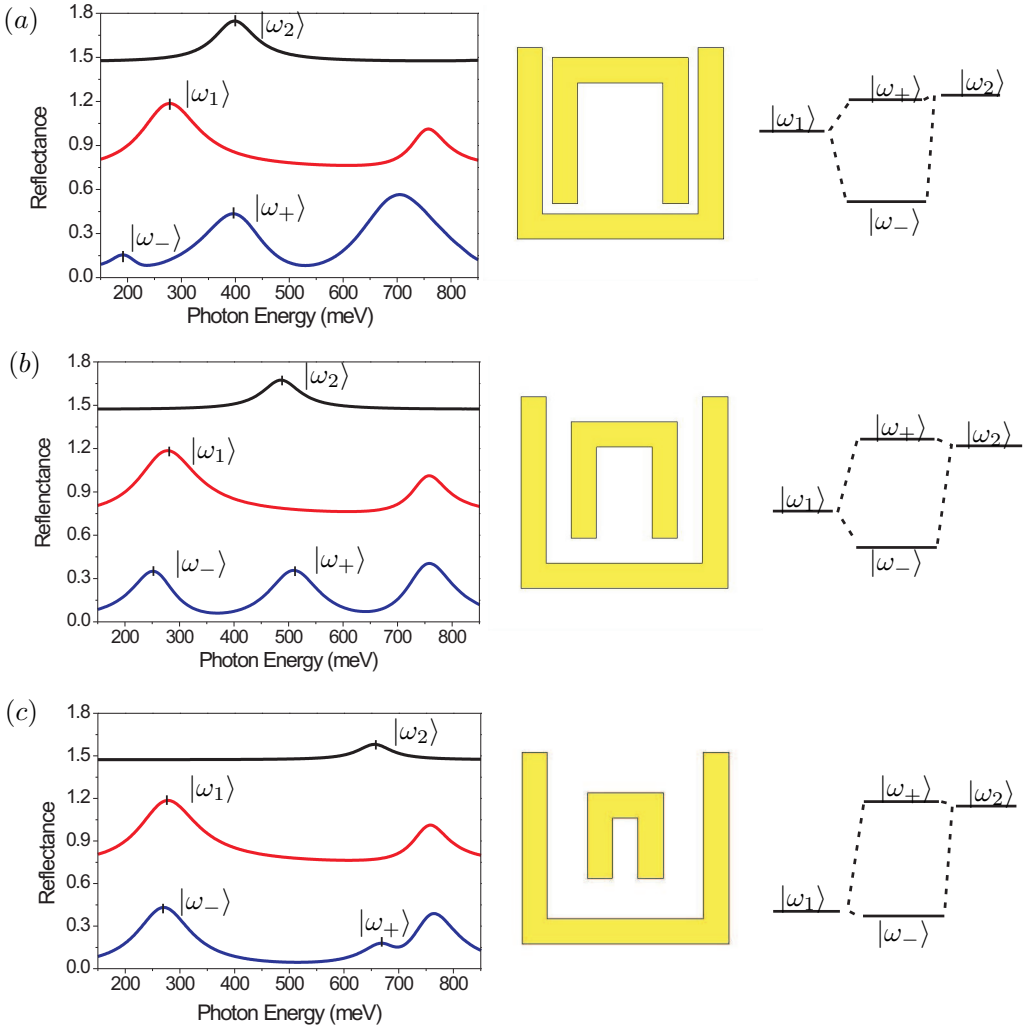

Figure 4.14: Simulated reflectance spectra for DSRR (blue curves) compared to the outer SRR alone (red curves) and the inner SRR alone (black curves) for various inner-ring sizes. $|\omega_1\rangle$ and $|\omega_2\rangle$ present the fundamental plasmonic eigenmodes of the outer and inner rings alone, respectively. For DSRRs, the lower energy anti-symmetric mode and higher energy symmetric modes are denoted as $|\omega_-\rangle$ and $|\omega_+\rangle$, respectively. In the simulations, the outer-ring size (l_{ox} = 410 nm, l_{oy} = 380 nm, w = 50 nm, t = 20 nm) and the array periods ($p_x = p_y$ = 550 nm) are kept constant. The inner-ring geometry is varied from (a) l_{ix} = 270 nm and l_{iy} = 290 nm; (b) l_{ix} = 210 nm and l_{iy} = 230 nm; and (c) l_{ix} = 150 nm and l_{iy} = 170 nm. The corresponding structure and plasmon hybridization diagrams are shown adjacent to the spectra. The individual spectra are shifted vertically for clarity.

are now strongly detuned (at 380 meV distance). Therefore, the coupling between them is strongly reduced and the induced plasmon energy shift is only 18 meV. The plasmonic modes of this DSRR can be regarded as a linear superposition of the plasmons of its constitute inner and outer rings alone. It is clear that the interaction strength between the plasmons is strongly influenced by the spatial distance and the resonant energy detuning between them. With the increased spacing and geometric length difference between the outer and inner rings, the plasmon energy shift is decreased. This corresponds to a decreased coupling strength.

The amplitudes of the DSRR resonances in the reflectance spectra are also influenced by the interaction between the outer and inner rings. For the symmetric mode $|\omega_+\rangle$ of the DSRR, the induced electric dipoles in the outer and inner rings oscillate in-phase; therefore the resonance amplitudes are increased. As for the anti-symmetric mode $|\omega_-\rangle$, the induced electric dipoles in both rings oscillate out-of-phase, which leads to an electric field of the DSRR similar to an electric quadrupole rather than an electric dipole. As the coupling efficiency of the external light field to this quadrupole is much weaker, the resonance amplitude is not as pronounced as that of the out ring alone. This is consistent with the observation in Fig. 4.14(a) and (b), where the amplitude of resonance $|\omega_-\rangle$ ($|\omega_+\rangle$) decreases (increases) relative to that of $|\omega_1\rangle$ ($|\omega_2\rangle$) in the coupling case.

4.5.3 Hybridization for various ring orientations

The picture of the plasmon hybridization also explains intuitively the influence of the orientation of the inner ring with respect to the outer ring on the DSRR resonance. Fig. 4.15 compares the simulated reflectance spectra for two orientations of the inner-ring. The geometry of the DSRRs used in the simulations are the same as those of Fig. 4.14(a). We denote the previously used orientation by configuration "A" and the inverted orientation by configuration "B". The resonances in configuration B at lower and higher energies are denoted by $|\omega_-^*\rangle$ and $|\omega_+^*\rangle$, respectively. In both cases, the introduction of an inner ring leads to two new eigenmodes when compared to the spectra of the outer and inner rings alone in Fig. 4.14(a). The calculated electric maximum peak field distributions of the resonances for both configurations are shown in Fig. 4.16. Out-of-phase charge oscillations are observed for both $|\omega_-\rangle$ and $|\omega_-^*\rangle$, whereas for $|\omega_+\rangle$ and $|\omega_+^*\rangle$, in-phase charge oscillation are observed. This is consistent with our analysis by the plasmon hybridization picture as indicated by the insets in Fig. 4.15.

Figure 4.17 shows the simulated magnetic maximum peak field distributions of

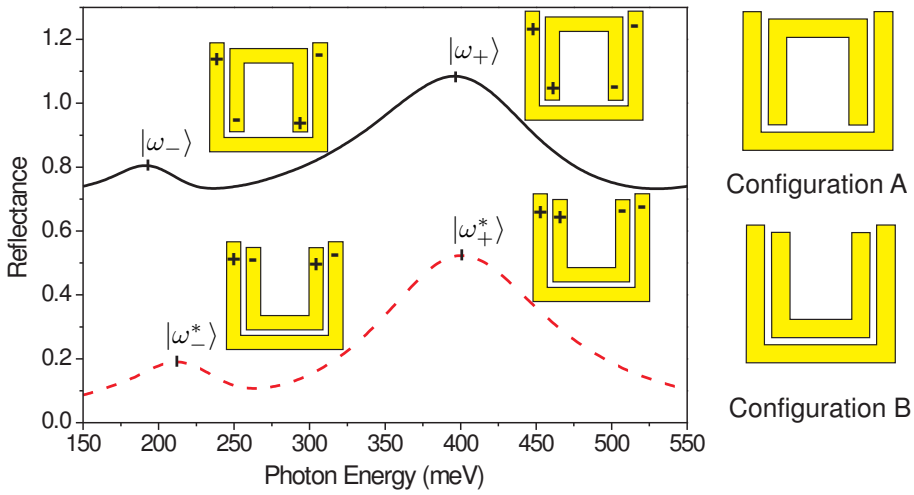

Figure 4.15: Calculated reflectance spectra of the DSRRs with two different inner-ring orientations: the gap bearing side of the outer and inner rings are in the opposite direction (configuration A) and in the same direction (configuration B). Resonances at lower and higher energies in configuration A (B) are denoted by $|\omega_-\rangle$ ($|\omega_-^*\rangle$) and $|\omega_+\rangle$ ($|\omega_+^*\rangle$), respectively. The insets show the dipole oscillations at the corresponding resonances by the plasmon hybridization analysis. The individual spectra are shifted upwards for clarity.

resonance modes $|\omega_-\rangle$ and $|\omega_-^*\rangle$, which correspond to the lower energy resonance peaks shown in Fig. 4.15. A strong magnetic field confinement is observed in both configurations. However, the magnetic field is confined in the center area of the DSRR in configuration A, but between the bottom arms of the inner and outer ring in configuration B. It is clear that the orientation of the inner ring with respect to the outer ring is not crucial for inducing the magnetic dipole in a DSRR.

4.6 Summary

We have demonstrated the thickness dependence of the optical resonance of SRRs in the optical regime both experimentally and numerically. It has been shown that the plasmonic model describes well the resonance behavior of SRRs in the optical regime. We have shown that the resonance properties of an SRR can be quantitatively described by an equivalent cut-wire, which has a similar total wire length as the SRR. By combining the plasmonic model with the hybridization concept, the optical properties of a DSRR in the optical regime have been well described. The interaction between the constitute inner and outer ring of a DSRR were interpreted intuitively.

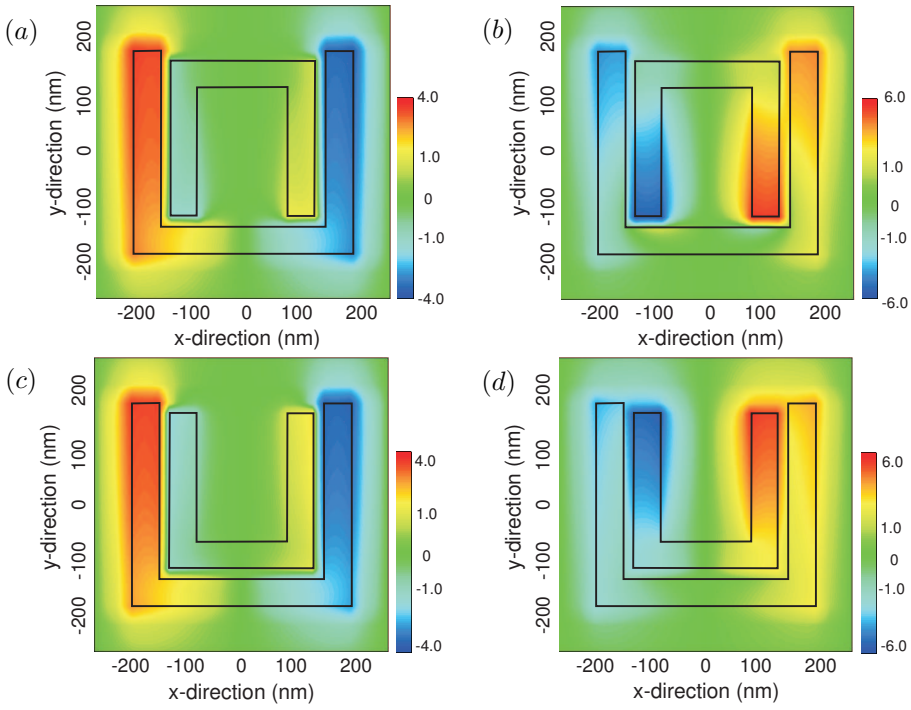

Figure 4.16: Simulated electric maximum peak field distribution of E_z in a plane 30 nm above the structure for resonant modes of: (a) $|\omega_-\rangle$, (b) $|\omega_+\rangle$, (c) $|\omega_-^*\rangle$, (d) $|\omega_+^*\rangle$, corresponding to the peaks shown in Fig. 4.15. The amplitudes are normalized to that of the incident light field.

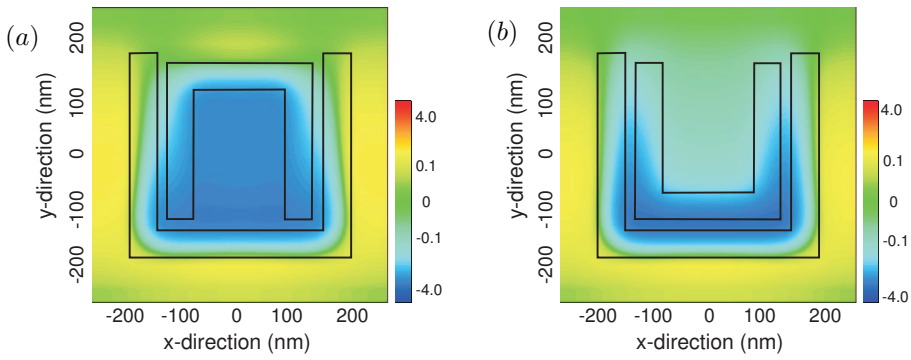

Figure 4.17: Simulated magnetic maximum peak field distributions of H_z in a plane 30nm above the structure for the resonant modes of (a) $|\omega_-\rangle$ and (b) $|\omega_-^*\rangle$ corresponding to the lower energy peaks shown in Fig. 4.15. The amplitudes are normalized to those of incident field.

The plasmonic model offers a simple picture to understand the optical responses of coupled systems in metamaterials and provides insight for the design of specific resonance properties.

5 Optical properties of bowtie slot antennas

Antennas are usually employed to manipulate electromagnetic radiation in radio frequencies, whereas mirrors and lenses are used to redirect the wavefronts of propagating radiation in the optical regime. However, due to the diffraction limit, lenses and mirrors can not concentrate the optical field into dimensions much smaller than the wavelength [79]. In order to overcome this obstacle, the concept of antennas is extended into the optical frequency range [17, 47]. In this chapter we investigate the optical properties of slot antennas, more specifically using the bow-tie slot antenna as an example. We demonstrate experimental results of bowtie slot antenna arrays in a thin metal film. Assisted by the numerical simulation tools, the resonance properties of bowtie slot antennas are discussed in the framework of geometry dependence. In the final part, the effect of metal properties on the resonances of bowtie slot antennas is discussed.

5.1 Introduction

Optical antennas have attracted considerable attention due to their potential in sub-diffraction resolution probing and providing light sources in the sub-wavelength range [13, 14, 51]. In contrast to simple wire types of antennas, slot antennas have the advantage of robustness, greater control of the radiation pattern [16]. Bowtie slot antennas are promising designs to obtain a particularly strong field enhancement due to their sharp edge design [52].

A bowtie slot antenna, which is composed of a bowtie shaped aperture in a metal film, is schematically shown in Fig. 5.1. Its geometry is defined by the thickness of the metal t, the outline lengths of the bowtie slot antenna a and b, the bowtie flare angle θ, and the gap size d. When the polarization of the incident light is perpendicular to the gap, the optical field is strongly confined in the gap area [44, 52].

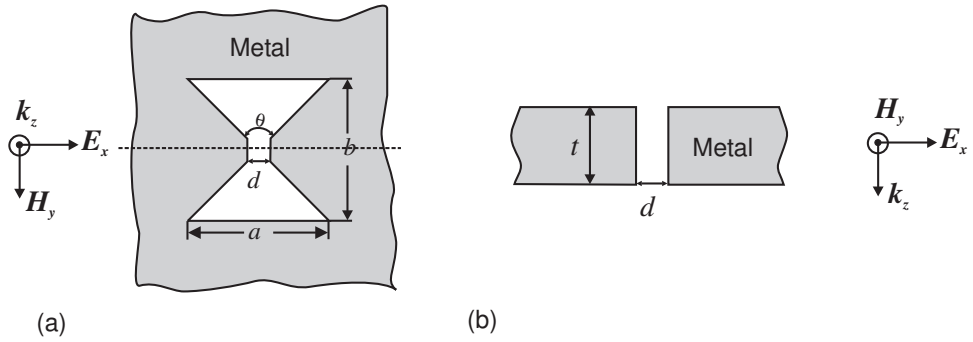

Figure 5.1: Schematic view of a bowtie slot antenna in a free-standing metal film. (a) Top view. (b) Cross sectional view at the location of the dashed line. The normally incident light is linearly polarized along the x direction.

The field confinement is generally determined by the small feature size of optical antennas, therefore, one can tune the near field spot size by varying the feature size of the antenna. It has been shown that bowtie slot antennas show a strong confinement of the light field when compared with the conventionally shaped slot antenna [46]. Figure 5.2 shows the near-field scanning optical microscope measurement of variously shaped slot antennas. It indicates that the bowtie slot antenna is able to provide a high resolution optical spot when the incident light is polarized across the bowtie gap. Although the rectangular slot antenna shows a greater transmission than that of the bowtie antenna, a smaller light spot size is achieved with the bowtie slot antenna.

Bowtie slot antennas have been applied in the near-field scanning optical microscopy [13] and contact nano-lithography [14] because of their capability to confine the incident light into sub-diffraction scale with strong field enhancement. Figure 5.3 shows one example where bowtie shaped nano-apertures were applied in contact nano-lithography. With the bowtie aperture masks in a 150 nm thick aluminum film, 70 nm holes in photoresist were achieved using 355 nm laser illumination [14].

As discussed in Chapter 2, the field enhancement and confinement of optical antennas are strongly resonance dependent. For bowtie slot antennas, although some primary experimental work has been demonstrated [44, 46, 80], the resonance behavior of bowtie slot antennas has not been clarified yet. In order to provide a guide for the designing and optimization of slot antennas for a variety of applications, we study the resonance properties of bowtie slot antennas based on experiment and numerical simulation.

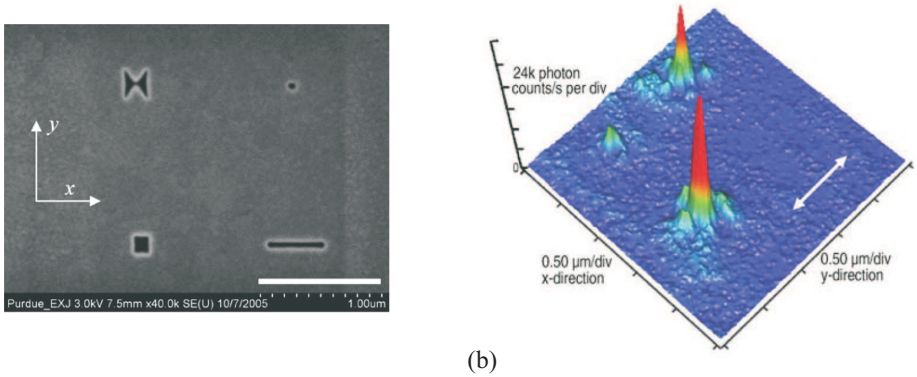

(a) (b)

Figure 5.2: (a) SEM pictures of the individual bowtie slot antenna and comparable square and rectangular slot antennas in a 160 nm thick gold film. (b) NSOM image of the slot antenna array in (a), which is 45° clockwise rotated with respect to the SEM image. The incident light is polarized along the y axis as shown by the arrow [46].

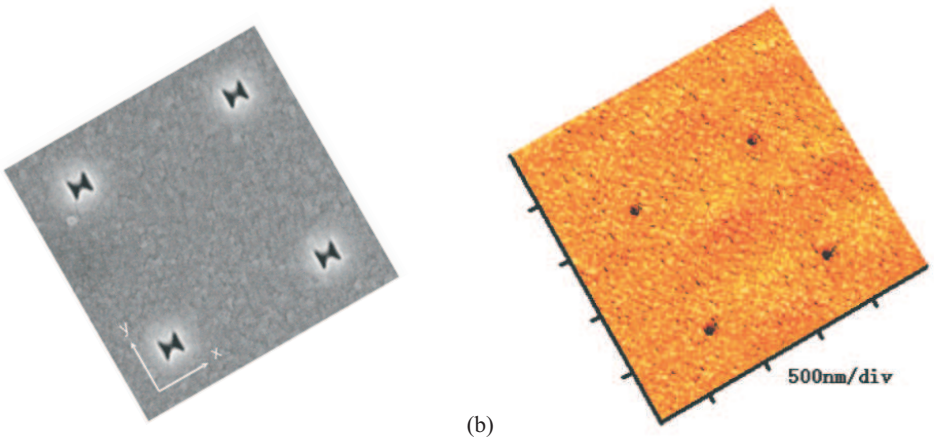

(a) (b)

Figure 5.3: (a) SEM picture of bowtie aperture array mask. (b) AFM topography image of hole arrays in photoresist with the mask in (a) using 355 nm laser illumination. The polarization of the light is along the y axis [14].

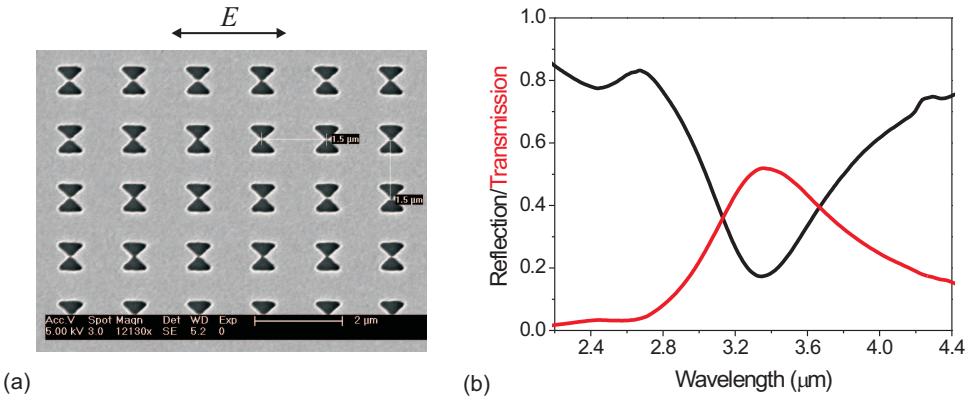

Figure 5.4: (a) SEM image of the bowtie slot antenna array. The antennas are arranged in a square lattice with a period of 1.5 μm. (b) Measured transmission and reflection spectra of the bowtie slot antenna array in a 20 nm thick gold film.

5.2 Experimental results

Experimentally, bowtie slot antenna arrays are fabricated in a 20 nm thick gold film which is deposited on a quartz substrate ($\epsilon_{quartz} = 2.1$) using electron beam lithography and subsequent ion beam etching. Figure 5.4 shows a scanning electron microscope (SEM) image of the bowtie slot antenna array. The antennas have a geometry of outline dimension $a = 600$ nm, $b = 700$ nm, gap size $d = 50$ nm, flare angle $\theta = 90°$. They are periodically arranged in the x and y directions with periods of $p_x = p_y = 1.5$ μm. Figure 5.4 shows the measured reflection and transmission spectra at normal incidence with a FTIR. As shown, they yield a transmission resonance near 3.3 μm.

The transmission and reflection spectra of the the slot antenna arrays are also simulated with the FITD algorithm. The period arrangement of the antennas and the incident light polarization are set by the waveguide boundary condition, which is equivalent to the periodic boundary condition. Figure 5.5 shows the simulated spectra of the bowtie slot antenna array corresponding to the experimental design. A good agreement is achieved between the experimental measurements and numerical simulations. Therefore, most further discussions are based on numerical simulations.

5.3 Substrate effect

In the infrared spectral range, slot antenna arrays are fabricated on dielectric substrates, which introduce a resonance frequency shift when compared to the antennas in free-standing metal films. It has been demonstrated that the influence of the di-

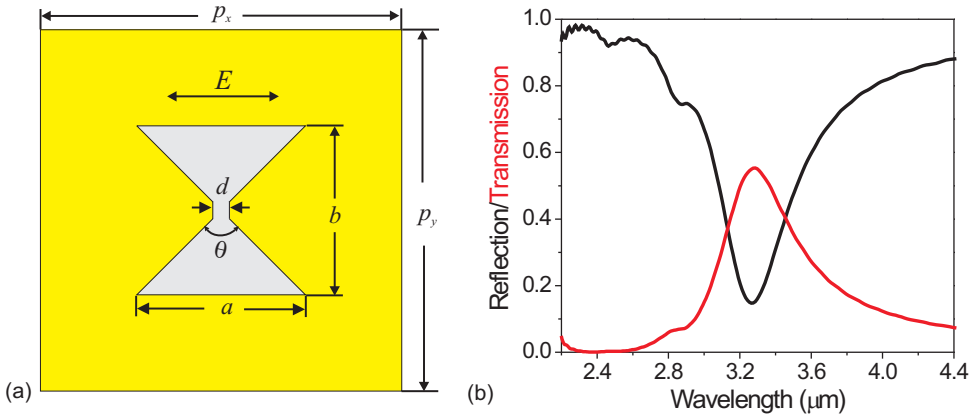

Figure 5.5: (a) Schematic of a bowtie slot antenna unit. (b) Simulated transmission and reflection spectra of the bowtie slot antenna array in a 20 nm thick gold film by using CST Microwave studio.

electric substrate can be described by an effective refractive index of the surrounding medium [81]. For antenna arrays in a very thin metal film which is deposited on a dielectric substrate, the resonance wavelengths can be estimated as

$$\lambda = n_{eff}\lambda_0 = \sqrt{\frac{\epsilon_{cov} + \epsilon_{sub}}{2}}\lambda_0, \tag{5.1}$$

where λ_0 is the resonance wavelength of the antenna array in a free-standing metal film and n_{eff} is the effective refractive index determined by the dielectric constants of the substrate ϵ_{sub} and the cover medium ϵ_{cov}. This approximation is valid in the optical regime for the rectangular slot antenna arrays in a thin metal film as well. Figure 5.6 shows the calculated resonance wavelength of the rectangular slot antenna arrays in a 20 nm thick gold film as a function of effective refractive index of the surrounding medium. Four different types of substrates MgF_2 ($\epsilon = 1.93$), SiO_2 ($\epsilon = 2.1$), SU-8 ($\epsilon = 2.5$), and ITO ($\epsilon = 3.61$) are used in our calculation. As shown in Fig. 5.6(b), the resonance wavelength of the antenna array linearly increases with the increasing effective refractive index as $\lambda_{res} = n_{eff}\lambda_0$, where n_{eff} is defined as $n_{eff} = \sqrt{(1 + \epsilon_{sub})/2}$.

For bowtie slot antennas, due to the field distribution variation, the effective refractive index is slightly different from the case of rectangular slot antennas. Figure 5.7(a) shows the schematic of a bowtie slot antenna unit in the antenna array. The resonance wavelength of the antenna array on various substrates is plotted as a function of the effective refractive index of the surrounding medium as shown in 5.7(b). The resonance wavelength of the antenna array increases linearly with the effective refractive index of the surrounding medium. However, for bowtie slot

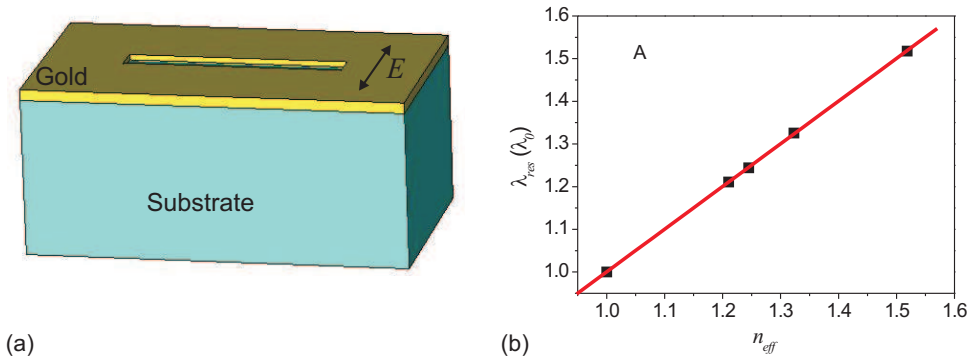

Figure 5.6: Effect of dielectric substrate on the resonances of rectangular slot antenna arrays. (a) Schematic of the rectangular slot antenna unit. (b) Resonance wavelength of the antenna array as a function of effective refractive index $n_{eff}$of the surrounding medium. n_{eff} can be defined as $\sqrt{(1+\epsilon_{sub})/2}$.

antenna arrays, n_{eff} is different from that defined in Eq. 5.1, one has to introduce a filling factor f to describe it as [4]

$$n_{eff} = \sqrt{f\epsilon_{cov} + (1-f)\epsilon_{sub}}, \tag{5.2}$$

where f is the filling factor of the cover medium. For bowtie slot antennas in a 20-nm thick metal film, the filling factor f is about 0.61. The filling factor increases with the increased thickness of the metal film.

Considering that the substrate effect on the resonance of the antenna array can be taken into account by introducing an effective refractive index, we consider the response of slot antenna arrays in a free standing metal film for a general discussion in the following sections.

5.4 Resonance dependence on geometry

Optical properties of antennas are strongly influenced by their geometry. For dipole antennas in the radio frequency range, the resonance wavelength can be estimated as $\lambda = 2l$, where l is the geometrical length [16]. In the optical frequency range, although the simple wavelength scaling breaks down [17, 47, 53], the resonance wavelength still varies like a linear function of the geometric length and the material parameters [49]. For complex geometry antennas such as bowtie slot antennas, design rules are urgently needed at optical frequencies. In this section, we will focus the discussion on the geometry effect on the resonances of bowtie slot antennas in gold films based on numerical simulations. The dielectric constant of gold is

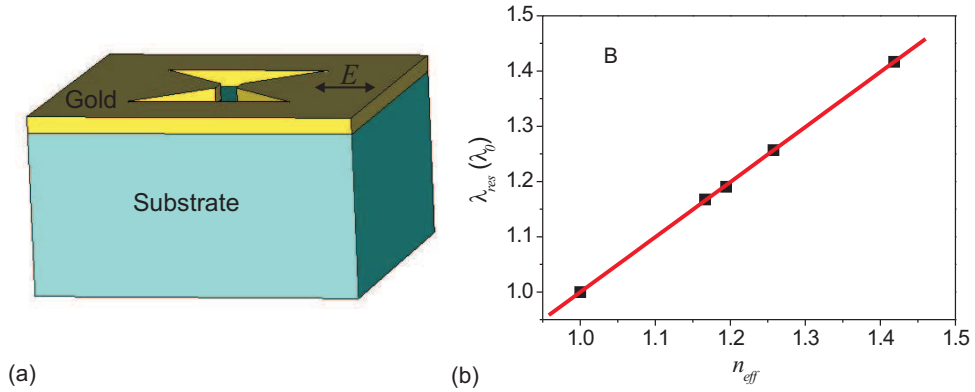

Figure 5.7: Effect of dielectric substrate on the resonance for bowtie slot antenna arrays. (a) Schematic of the bowtie slot antenna unit. (b) Resonance wavelengths of antenna arrays as a function of effective refractive index $n_{eff}$of the surrounding medium. n_{eff} can be defined as $\sqrt{f + (1-f)\epsilon_{sub}}$.

described by the Drude model.

5.4.1 Period effect

In order to easily characterize the optical properties of slot antennas, they are normally fabricated on a substrate with periodical arrangement. We have shown that the substrate effect can be taken into account with an effective refractive index of the surrounding medium. In order to make sure the response of the individual slot antennas can be described by the collective response of the antenna arrays, the period effect on the resonance of the antenna arrays is investigated.

Figure 5.8 shows the transmission spectra of bowtie slot antenna arrays for various periods. The periods of the antenna arrays are increased from 250 nm to 1.0 μm in steps of 150 nm. The geometry of the individual slot antenna is defined as a = 150 nm, b = 150 nm, d = 40 nm, and θ= 90°. For the antenna arrays with periods much smaller than resonance wavelength ($p_x = p_y$ = 250 nm, 400 nm, and 550 nm), only one clear transmission resonance is observed in the visible and near infrared spectral range. However, when the periods of the antenna array are comparable with the resonance wavelength ($p_x = p_y$ = 700 nm, 850 nm, and 1000 nm), several narrow peaks are observed in the transmission spectra.

Upon the excitation of by the external light field, each antenna can be regarded as a harmonic oscillator. When the period of the antenna array is smaller than the resonance wavelength ($p_x = p_y$ = 250 nm, 400 nm, and 550 nm) and illuminated from normal incidence, antennas resonate all in-phase, and the periodic arrangement

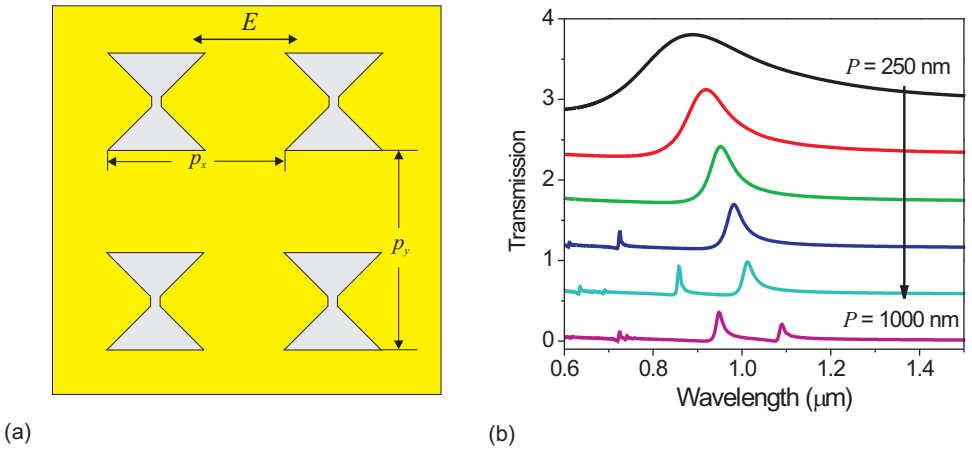

Figure 5.8: (a)Schematic of a bowtie slot antenna array. (b) The transmission spectra of bowtie slot antenna arrays for various periods. The period of the array ($p_x = p_y = P$) is varied from 250 nm to 1000 nm in steps of 150nm.

of the antennas has very little influence on this collective response. This is similar to the observation of the optical spectra of metamaterials in optical frequencies [10]. Namely, the resonance behavior of a single antenna can be described by the collective response of the antenna array.

When the period of the antenna array is comparable to the resonance wavelength, the periodic arrangement of the antenna acts as a grating coupler as well. When the momentum matching condition as shown in Eq. 2.17 is satisfied, surface plasmon modes that propagate along the dielectric/metal surface can be excited [3]. The variation of period can change the momentum matching condition, therefore the transmission properties of the slot antenna arrays are influenced strongly by the period of the array, which is the case for the arrays with larger periods ($p_x = p_y =$ 700 nm, 850 nm, and 1000 nm) in Fig. 5.8.

The enhanced transmission of nano-aperture arrays has been interpreted as surface plasmon excitation due to the periodic arrangement of the apertures [35]. Following this explanation, surface plasmon modes for the 850 nm period antenna array should appear at the wavelengths of 861 nm and 619 nm, which correspond to the indices $(1, 0)$ and $(1, 1)$ of Eq. 2.37, respectively. However, the transmission peaks are observed at 1.01 μm and 857 nm as shown in Fig. 5.8(b). In contrary, the calculated surface plasmon wavelengths are located in the minimum positions of the transmission spectra. Apparently, the surface plasmon excitation in the antenna array quenches the transmission of the individual slot antennas. Similar results have been obtained for circular hole arrays by a FDTD simulation [82].

In the case that the resonances of individual antennas dominate the transmission properties of the slot antenna arrays, the period variation also introduce a slight shift of the transmission peak position. As shown in Fig. 5.8, when the period of antenna array is increased from 250 nm to 550 nm, the resonance wavelength of the antenna array shifts slightly to a longer wavelength. This can be understood with the Babinet's principle by considering the interaction between the neighboring units in the antenna array.

Babinet's principle is a classic concept of the wave theory of light. It had originally been used to simplify the analysis of certain diffraction problems [79]. In scalar formulation, Babinet's principle yields a correspondence between an amplitude transmission mask and a complementary mask. As shown in Fig. 5.9, the specular transmission coefficient for one bowtie slot antenna array in an infinite thin perfect conductor film equals to the reflection coefficient of its complementary array when the polarization is rotated by 90°. Although metals behave different from perfect conductors, Babinet's principle still provides a good indication for the optical properties of complementary metallic nano-structures in the visible and near infrared regime [83]. Therefore, the interaction between neighboring slot antennas in Fig. 5.9(a) can be equivalently described by the dipole-dipole interaction of neighboring bowtie antennas in Fig. 5.9(b) with rotated light polarization.

Generally, the dipole-dipole interactions between the monomers in dimers are described in the framework of the exciton coupling theory [84, 85]. The excited-state levels of the monomers split into two levels due to the hybridization effect. The concept is shown in Fig. 5.10, the lower and the higher energy level relative to the excited state of the monomers correspond to two possible arrangements of the monomer transition dipoles in the dimer. Depending on the orientation of the monomers in the dimer, different configurations of symmetric and antisymmetric coupled states are obtained. Parallel dimers as shown in Fig. 5.10(a) correspond to the interaction of neighboring dipoles in the x direction as depicted in Fig. 5.10(b). In this configuration, the transition to the lower energy excited state is forbidden due to the cancellation of two dipole moments. Therefore, the interaction between the neighboring bowtie dipoles in the x direction shifts the resonance of dipole antenna arrays to a higher energy level relative to the excited state of a single dipole. Head-to-tail dimers as shown in Fig. 5.10(c) correspond to the interaction of neighboring dipoles in the y direction as indicated in Fig. 5.10(d). In this configuration, the transition to the high energy excited state is forbidden due to the cancellation of two dipole moments. Thus, the interaction between the neighboring bowtie dipoles

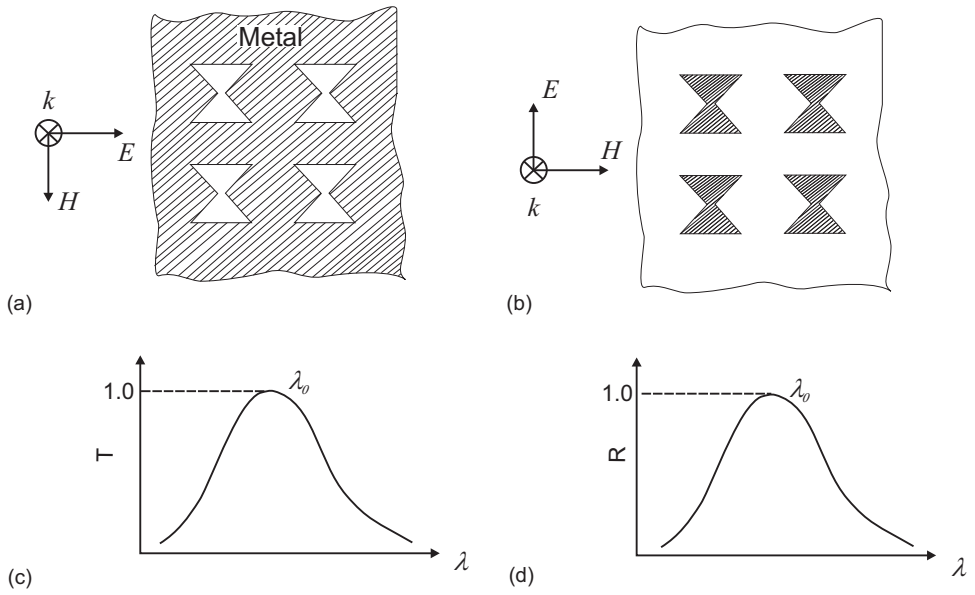

Figure 5.9: Schematic of one example of complementary arrays: the slot antenna arrays in (a) and dipole antenna arrays in (b). The transmission spectrum of the slot antenna array in (c) is just like the reflection spectrum of the dipole antenna array in (d).

in the y direction shifts the resonance of dipole antenna arrays to a lower energy level relative to the excited state of a single dipole.

Figures 5.11(a) and (b) show the transmission spectra of bowtie slot antenna arrays for various periods along the x and y direction, respectively. With Babinet's principle, the resonance behavior of slot antenna arrays can be described by that of the complementary structures with polarization rotated light illumination as shown in Fig. 5.10(b) and (d). The increased period along the x direction leads to a reduced coupling strength of the neighboring dipoles. Since the coupled state has a higher energy level than that of a single dipole antenna, weak coupling results in a lower energy level coupled state. Therefore, the transmission peak of the slot antenna array shifts to a longer wavelength with increased period. As for the y direction, the increased period weakens the coupling strength between the neighboring units as well. However, the coupled state is at a lower energy level than that of a single antenna. Thus, the weak coupling lifts the coupled state to a higher energy level. Therefore, the resonances of the antenna arrays shift to shorter wavelengths with increased period.

This electrostatic picture predicts the resonance shift of a dipole antenna array due to the interaction between the neighboring dipole antennas. Following this

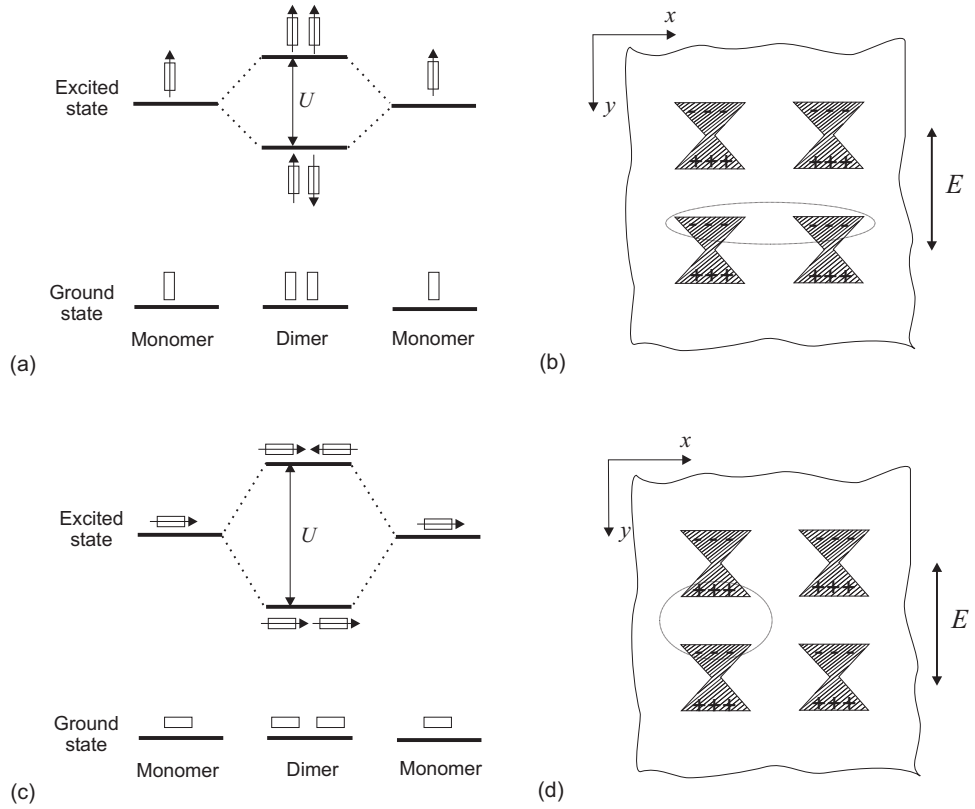

Figure 5.10: Schematic of energy level splitting resulting from the interaction of monomers in a dimer. (a) Parallel dimer arrangement induces a higher energy symmetric mode and lower energy anti-symmetric mode. (b) The charge distribution of dipole antennas in a antenna array. The two dipoles in the x direction correspond to a parallel dimer. (c) Head-to-tail dimer arrangement results in a higher energy anti-symmetric mode and lower energy symmetric mode. (d) The charge distribution of dipole antennas in a antenna array. The two dipoles in the y direction correspond to a head-to-tail dimer.

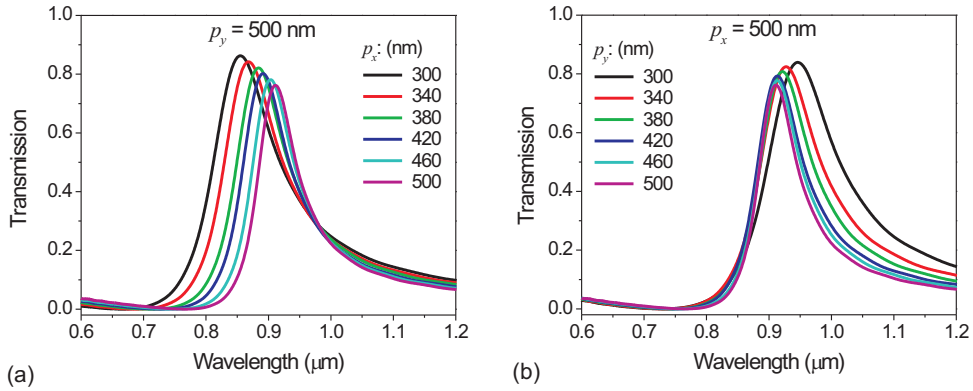

Figure 5.11: Transmission spectra of bowtie slot antenna arrays for various periods. The geometry of the antenna is defined as a = 150 nm, b = 150 nm, d = 40 nm, and θ= 90°. (a) The period in the y direction is constant as p_y = 500 nm, and The period in the x direction p_x is varied from 300 nm to 500 nm in steps of 40 nm. (b) The period in the x direction is constant as p_x = 500 nm, and the period in the y direction p_y is varied from 300 nm to 500 nm in steps of 40 nm.

approximation, the interaction strength between the parallel aligned dipole is one-half of that of the head-to-tail aligned dipole [32, 85]. The interaction along the y direction should dominate the resonance behavior of the antenna arrays. Thus, the resonance wavelength of the antenna array has a blue-shift with increased period in a square lattice. However, as shown in Fig. 5.8 for the antenna arrays with periods of $p_x = p_y$ = 250 nm, 400 nm, and 550nm, the resonance wavelength of the antenna array shifts to a longer wavelength with increased period. Apparently, the electrostatic dipole-dipole interaction can not fully interpret the resonance behavior of the antenna arrays.

As we mentioned in Chapter 2, the fields of a dipole antenna is only equivalent to that of an electrostatic dipole in the *near field* region, where $r_0 < \lambda/2\pi$ with r_0 being the distance from the antenna. In our case, the distance between antennas ($r_0 > \lambda/4$) is out of the *near field* region, the *radiative field* effect has to be considered. Intuitively, the stronger interaction of the x direction than the y direction can be attributed to the radiative field distribution. For dipole antennas, the radiative fields are concentrated in the direction perpendicular to the polarization of the dipole.

Moreover, the fields of an antenna are also modulated by the factor e^{ikr} as shown in Eq. 2.40 and Eq. 2.43, which can lead to a major change in the response of an antenna array relative to that predicted by the electrostatic approximation. In order to fully interpret the spectral behavior of antenna arrays, further studies are

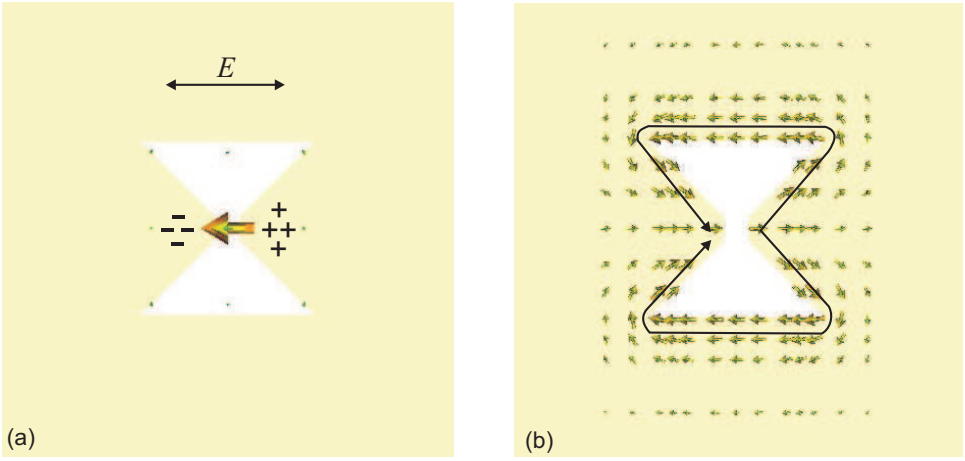

Figure 5.12: (a) Electric field distribution of the bowtie slot antenna at resonance. (b) Current density distribution of the bowtie slot antenna at resonance.

needed.

Based on above discussions, one can see that when the period of the antenna array is smaller than the resonance wavelength of the individual antennas, the resonance properties of the antenna array can represent the response of a single antenna. The period effect on the resonance of the antenna arrays can be neglected when taking the coupling effect of neighboring antennas into account.

5.4.2 Aperture perimeter effect

At radio frequencies, the resonance wavelength of an antenna is mainly determined by the electrical length of the antenna [16], which is equivalent to the oscillation path length of the conduction electrons of metallic nano-structures at resonance. For bowtie slot antennas, when the incident electric field is polarized perpendicular to the gap, surface polarization results in a charge accumulation at the gap edges as shown in Fig. 5.12 (a). This charge distribution leads to a current distribution as depicted in Fig. 5.12(b), where the oscillating current flows around the bowtie aperture edge.

Clearly, the oscillation path length of the conduction electrons in a bowtie slot antenna is determined by the aperture perimeter, which plays an important role for the resonance of the antenna. Figure 5.13(a) shows the family of curves of transmission spectra of bowtie slot antenna arrays in a 30 nm thick free-standing gold film. The gap size d and flare angle θ are kept constant as 40 nm and 90°, respectively. The aperture perimeter L is varied from 0.93 μm to 2.38 μm in steps of about 480 nm by adjusting the outline dimensions length of a and b. The periods

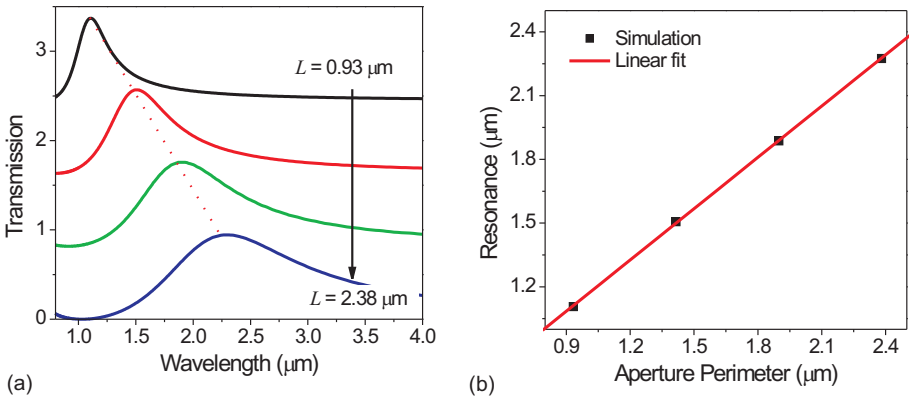

Figure 5.13: Family of curves showing the calculated transmission spectra of bowtie slot antennas in free-standing gold films for normal light incidence. The gap size, angle, and film thickness of slot antennas are kept constant (d = 40 nm, $\theta = 90°$, and t = 30 nm) and the aperture perimeter is varied from 0.93 μm to 2.38 μm in steps of about 480 nm by tuning the outline dimensions a and b. The period of the antenna arrays is increased from 350 nm to 650 nm in steps of 100 nm with the increased aperture perimeter. The individual spectra are shifted upwards for clarity. (b) Resonance wavelengths as a function of the aperture perimeter of slot antennas.

of the antenna arrays p_x and p_y are increased from 350 nm to 650 nm in steps of 100 nm, corresponding to the increased aperture perimeter. One can see that the resonance wavelengths of bowtie slot antennas shift to longer wavelengths with the increased aperture perimeter. Fig. 5.13(b) shows the resonance wavelengths as a function of aperture perimeter, and the resonance wavelength increases linearly with the aperture perimeter as

$$\lambda = a_1 L + a_2, \tag{5.3}$$

where L is the aperture perimeter of the slot antenna and a_1 and a_2 are linear coefficients determined by the geometry of the antenna and material properties.

Figure 5.14 shows resonance wavelengths of bowtie slot antennas as functions of aperture perimeter for various film thicknesses and gap sizes. Figure 5.15 shows resonance wavelengths of bowtie slot antennas as functions of aperture perimeter for different metals. The linear coefficient a_1 is nearly constant for all the film thicknesses, gap sizes and metal materials, whereas a_2 is strongly influenced by the geometry and the metal properties. Nevertheless, the linear dependence of the resonance wavelength on the aperture perimeter is valid for all the cases.

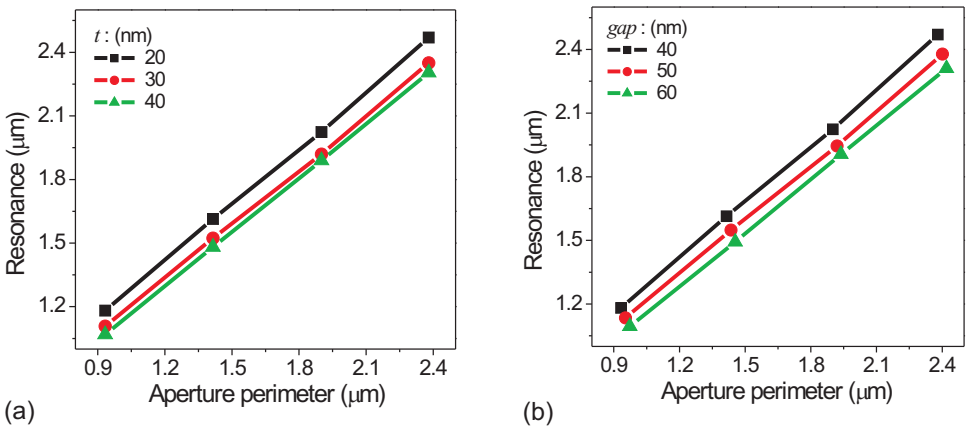

Figure 5.14: Resonance wavelengths of bowtie slot antennas as functions of aperture perimeter for various film thicknesses and gap sizes. (a) Antennas have fixed flare angle $\theta = 90°$ and gap size $d = 40$ nm. The thickness is varied from 20 nm to 40 nm in steps of 10 nm. (b) Antennas have fixed flare angle $\theta = 90°$ and film thickness $t = 20$ nm. The gap size is varied from 40 nm to 60 nm in steps of 10 nm. In both cases, the outline dimensions a and b are varied to tune the aperture perimeter.

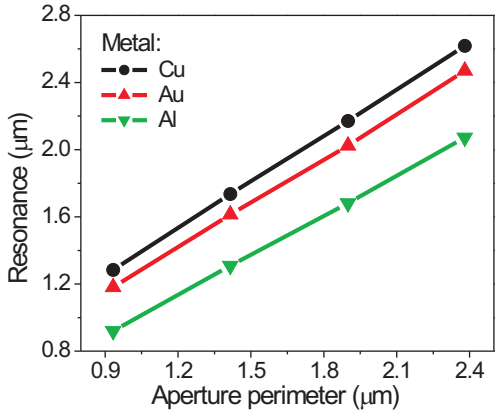

Figure 5.15: Resonance wavelength of bowtie slot antennas as functions of aperture perimeter for various metals. Antennas have fixed flare angle $\theta = 90°$, film thickness $t = 20$ nm, and gap size $d = 40$ nm. The outline dimensions a and b are varied to tune the aperture perimeter.

5.4.3 Outline dimension and aperture area effect

To confirm that the linear shifting of the resonance wavelength with the aperture perimeter is not solely from the increase of the outline dimension a or b in the aperture perimeter tuning, we keep the aperture perimeter constant, but a and b as variables to study the transmission properties of bowtie slot antennas. As shown by the schematic of the bowtie slot antenna in Fig.5.16(a), in order to keep L as constant, but vary a and b, the flare angle θ of the antenna has to be changed. Figure 5.16(c)-(f) show the geometry variation of constant perimeter bowtie slot antennas for various flare angles. The gap size of the antenna and the thickness of the gold film are $d = 40$ nm and $t = 30$ nm, respectively. The period is tuned as to keep the distance between the neighboring antennas as 150 nm. The squares in Fig. 5.16(b) show the resonance wavelengths of bowtie slot antennas with constant aperture perimeter for various flare angles. Although the shape of the antenna is changed, the resonance wavelength is nearly kept as constant. For comparison, the resonance wavelengths of the antennas with constant a and b for various flare angles are also shown in the same figure (solid circles and triangles, respectively). Clearly, only antennas with constant aperture perimeter are resonant at nearly the same resonance wavelength for various flare angles. In the case of constant a or b, the resonance wavelength shifts to either a longer or a shorter wavelength when the flare angle is changed.

At optical frequencies, the resonance properties of a loop antenna can also be described by a quasi-static LC circuit. As shown in Chapter 4, the resonance frequency of a split-ring resonator is approximately to

$$\omega_{LC} = \frac{1}{\sqrt{LC}} = \frac{1}{\sqrt{l_x l_y}} \frac{c_0}{\sqrt{\epsilon_{eff}}} \sqrt{\frac{d}{w}} \propto \frac{1}{\sqrt{S}}. \tag{5.4}$$

This can be rewritten as

$$\lambda_{LC} = \frac{2\pi c}{\omega_{LC}} \propto \sqrt{S}. \tag{5.5}$$

where S is the area of the antenna. In this approximation, the area of the antenna determines the resonance wavelength of a loop antenna. One could argue that based on Babinet's principle, the aperture area plays an important role in determining the resonance wavelength of slot antennas. Therefore, we investigate the transmission properties of bowtie slot antennas with constant areas. Figure 5.17 shows the resonance wavelengths of the bowtie slot antennas as a function of flare angle. The film thickness and gap size of the antennas are kept constant. One can see that the resonance wavelength of the antenna shifts to a longer wavelength with increased

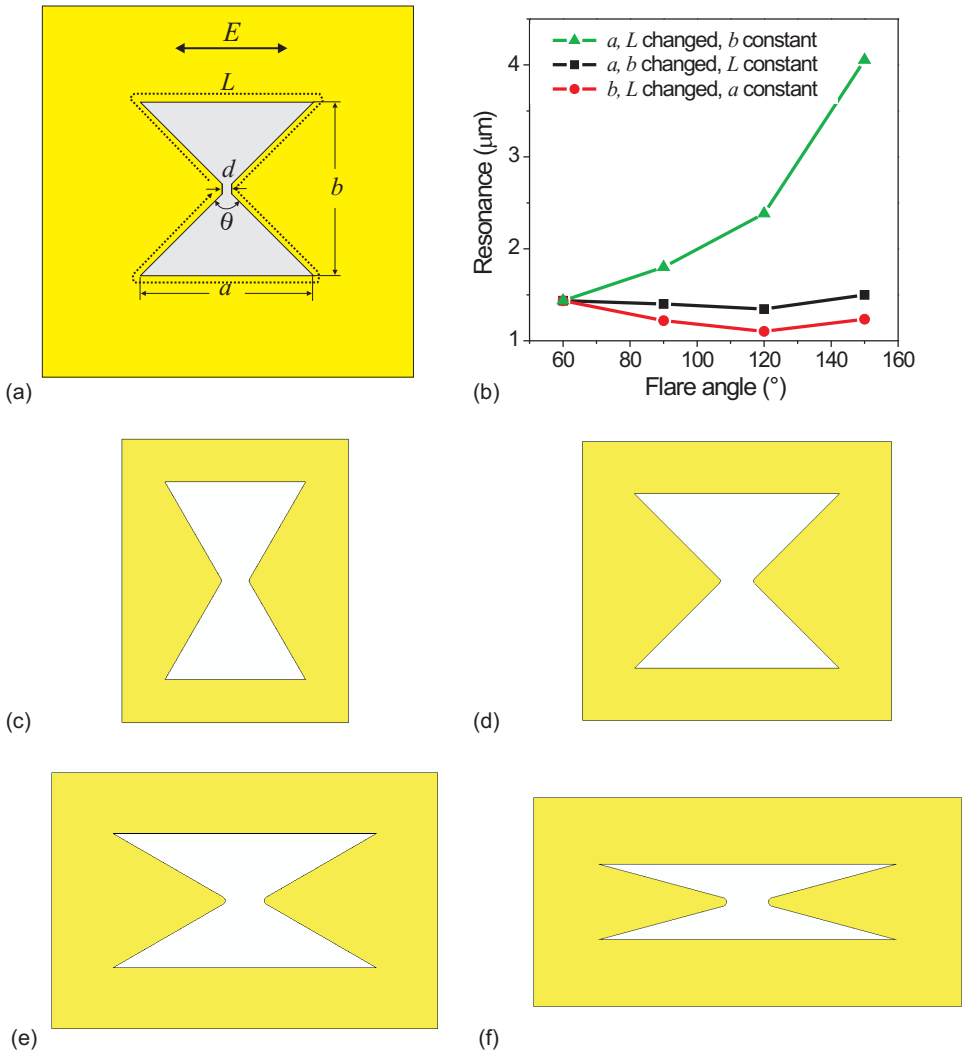

Figure 5.16: Flare angle dependence of the resonance of the bowtie slot antenna. (a) Schematic of the bowtie slot antenna. (b)Resonance wavelength as a function of flare angle of the antenna. (c)-(f) Schematic of bowtie slot antennas in various flare angles.

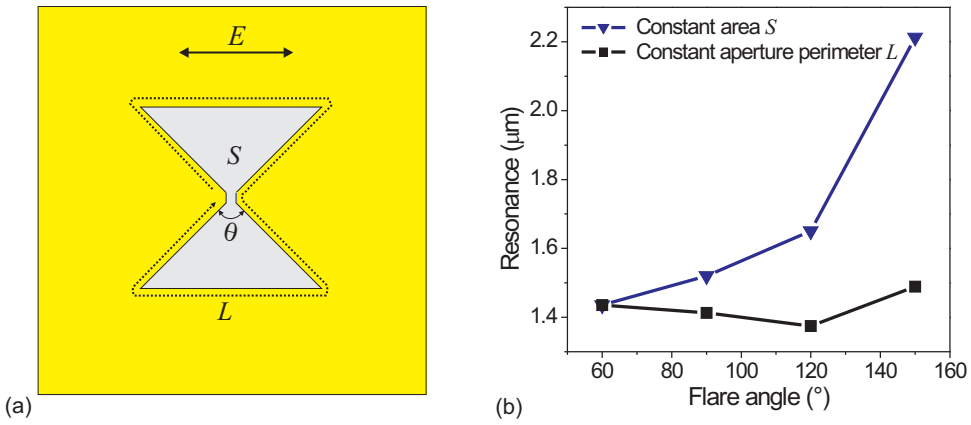

Figure 5.17: Flare angle dependence of the resonance of the bowtie slot antenna with constant aperture area. (a) Schematic of the bowtie slot antenna. (b) Resonance wavelength as a function of antenna flare angle.

flare angle when the aperture area is kept constant. The resonance wavelengths of antennas with the constant aperture perimeter with various flare angles are given in the same figure for comparison. This offers further evidence that the aperture perimeter plays an important role in determining the resonance wavelength of slot antennas.

5.4.4 Gap size effect

The gap size of the bowtie slot antenna determines the resolution of the near field. It influences the resonance properties of bowtie slot antennas as well because the restoring force between the polarized charges varies with the gap size. Figure 5.18 shows the transmission spectra of bowtie slot antennas with various gap sizes. The outline dimension of the antenna is fixed as $a = b = 300$ nm, the period of the antenna array is $p_x = p_y = 450$ nm, the thickness of gold film is 30 nm, and the flare angle is about 90°. With increased gap size, the resonance wavelength of the antenna shifts to a shorter wavelength. From the plasmonic point of view, a larger gap size reduces the Coulomb force between negative and positive charges in the gap area, which leads to a stronger restoring force along the oscillation path length of the conduction electrons. Therefore, the resonance wavelength of the antenna exhibits a blue shift with increased gap size.

5.4.5 Thickness effect

In this section, the thickness influence on the resonance properties of bowtie slot antennas in free-standing gold films is investigated. The constant geometry of the

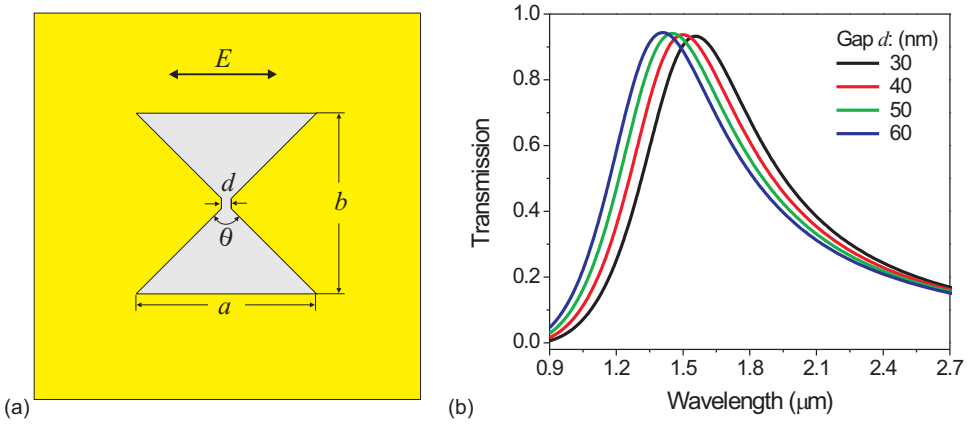

Figure 5.18: Gap size influence on the resonance properties of bowtie slot antennas. (a) The schematic of a bowtie slot antenna. (b) Transmission spectra of bowtie slot antennas in various gap sizes.

antennas has the outline dimensions $a = b = 300$ nm, a flare angle $\theta = 90°$, and a gap size $d = 40$ nm. Figure 5.19(a) shows the transmission spectra of bowtie slot antennas in various film thicknesses. With increased thickness of the metal film, in addition to the resonance (A) at the longer wavelength range, which we have discussed in the above sections, another resonance (B) appears at the shorter wavelength range in the thicker metal film cases. This resonance shows a different dependence on the thickness of the metal film. As depicted in Fig. 5.19(b), the wavelength of resonance A is nearly independent on the film thickness, especially in the cases of thicker metal films. For resonance B, the resonance wavelength increases nearly linearly with the film thickness.

In order to gain physical insight into these resonances, the electric field and current distributions at the resonance wavelengths are calculated and shown in Fig. 5.20(a)-(d). The resonance A has a dipole-like charge distribution at the sharp edges of the gap area, which leads to an induced current flow around the aperture edge as depicted in Fig. 5.20(a). The corresponding electric field distribution along the z axis in the gap area is shown in Fig. 5.20(b). The electric field is distributed nearly homogeneously in the gap area along the z axis.

As shown, the wavelength of resonance A of the bowtie slot antenna is mainly determined by the oscillation path length of the conduction electrons, which is not influenced by the metal thickness. In principle, the resonance A of the antenna is thickness independent. However, the resonance wavelength depends not only on the aperture perimeter of the slot antenna, but also the refractive index of the surrounding medium, which influences the coefficients a_1 and a_2 of Eq. 5.3. This

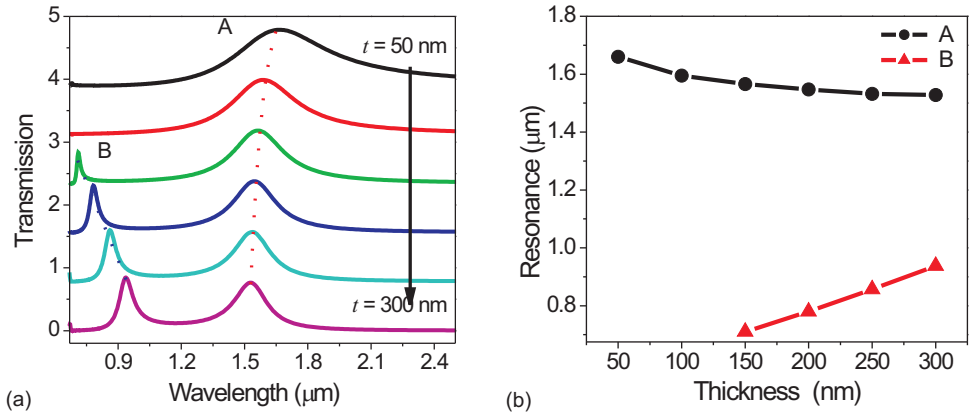

Figure 5.19: (a) Family of curves showing the calculated transmission spectra of bowtie slot antenna arrays in various thickness of the gold film. The outline dimension, gap size, and angle of slot antennas are kept constant ($a = b = 300$ nm, $d = 40$ nm, $\theta = 90°$, and $p_x = p_y = 450$ nm). The thickness of gold film t is varied from 50 nm to 300 nm in steps of 50 nm. The individual spectra are shifted upwards for clarity. (b) The resonance wavelengths are plotted as functions of the gold film thickness.

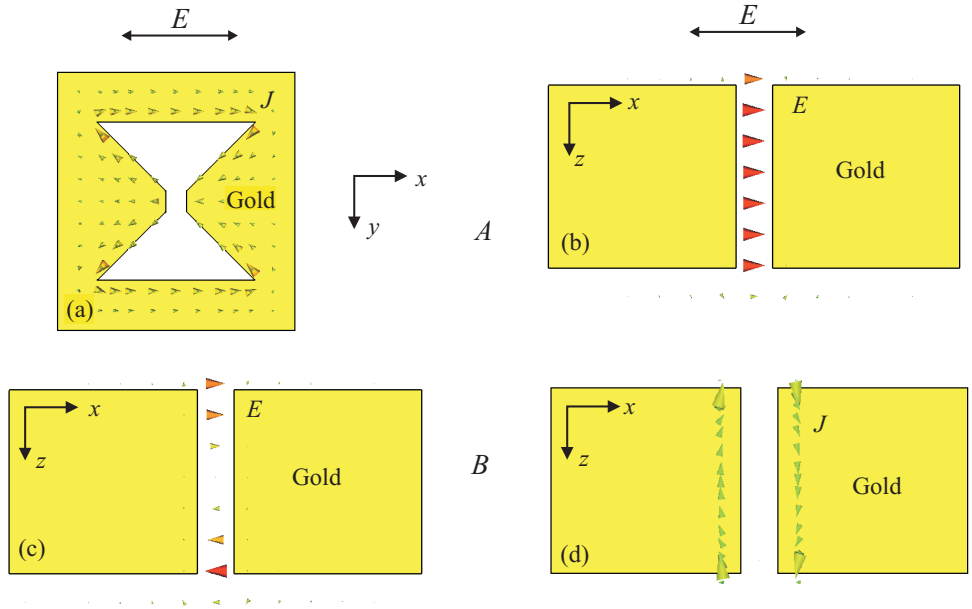

Figure 5.20: (a) Distribution of electric field of resonance A. (b) Current density distribution of resonance A. (c) Electric field distribution of resonance B. (d) Current density distribution of resonance B. The polarization of the incident light is perpendicular to the gap as shown.

phenomena is similar to the case of diameter variation of nanorod antennas [49], where the resonance wavelength shifts to a shorter wavelength with an increase of the radius of the rod.

In contrast to resonance A, the field distribution of resonance B shows that charges are accumulated at the upper and lower interface of the aperture gap area. The electric field in the gap along the z axis has the profile of a standing wave with antinodes at each interface as shown in Fig. 5.20(c). The corresponding induced current distribution is shown in Fig. 5.20(d). This behavior is analogous to the that of a Fabry-Pérot cavity at resonance, where a standing wave is excited in the cavity at the resonance wavelength. The resonance wavelength of the cavity is determined by the geometric length l of the cavity [79]. In the case of bowtie slot antennas, the thickness of the metal film is analogous to the length of the Fabry-Pérot cavity. Therefore, the wavelength of resonance B increases nearly linearly with the film thickness.

In order to distinguish the different characteristics of resonances A and B, we refer to resonance A as dipole-like resonance (labelled DP resonance) due to its dipole-like charge oscillation characteristic. As for resonance B, we name it Fabry-Pérot-like resonance (labelled FP resonance), since the electric field distribution has a standing wave profile just like a Fabry-Pérot cavity.

FP resonances have been observed in metallic gratings with sub-wavelength slits as well as in other types of apertures [44, 86, 87, 88, 89]. Commonly, the wavelength of the resonance is determined by the Fabry-Pérot resonance condition as

$$\lambda = 2n_{eff}t/m, \tag{5.6}$$

where n_{eff} is the effective refractive index, and m an integer. n_{eff} is normally determined by numerical calculations [87]. Figure 5.21 shows a general overview of the resonances of bowtie slot antennass as functions of the thickness of the gold film. Higher order FP resonances are excited in the shorter wavelength range with increased film thickness. When the thickness of the metal film is smaller than one-half of the aperture perimeter, the resonance wavelengths of FP resonances increase linearly with the thickness of the metal film. In contrast, when the thickness of the metal film is comparable with the aperture perimeter, the linear increase of the resonance wavelength of FP resonance with the film thickness is no longer valid and the DP resonance wavelength behaves just like the cut-off wavelength of the FP resonance.

The complex dependence of FP resonances of bowtie slot antennas on the thickness

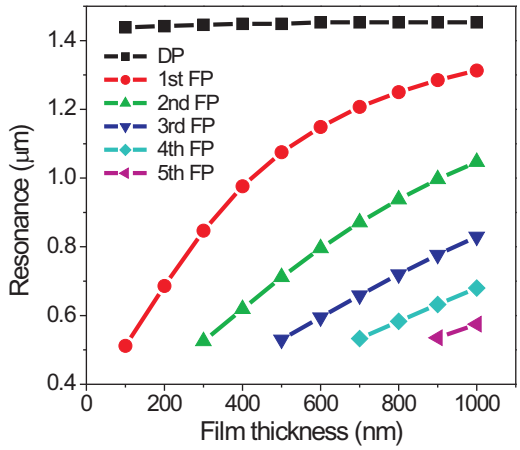

Figure 5.21: (Dependence of resonance of bowtie slot antenna on the thickness of gold film. The geometry of the antenna is defined as $a = b = 300$ nm, $d = 40$ nm, $\theta = 90°$, and $p_x = p_y = 450$ nm.

of the metal film is observed for all kinds of metals. Figures 5.22(a) and (b) show the resonance wavelengths of bowtie slot antennas as functions of the thickness of the metal for silver and a perfect electric conductor (PEC), respectively. The values for gold and silver are actually superimposed on each other. The similar resonance dependence on thickness is observed for gold, silver, and the PEC.

5.4.6 Aperture perimeter effect on FP resonances

Figure 5.23(a) shows the calculated transmission spectra of bowtie slot antennas in a 200 nm thick free-standing gold film with various aperture perimeters. The gap size d and flare angle θ are kept constant as 40 nm and 90°, respectively. The aperture perimeter L is varied from 0.93 μm to 2.38 μm in steps of about 480 nm by adjusting the outline dimensions length of a and b. The periods of the antenna arrays p_x and p_y are increased from 350 nm to 650 nm in steps of 100 nm, corresponding to the increased aperture perimeter. One can see that both DP and FP resonances are excited in the visible and near infrared range for all the antennas. Figure 5.23(b) shows the resonance wavelengths of DP and FP resonances as functions of the aperture perimeter.

For the DP resonance, the resonance wavelength shifts linearly to a longer wavelength with increased aperture perimeter, which is the same as the case of antennas in thinner metal films. However, for the FP resonance, the resonance wavelength is nearly independent on the aperture perimeter. In contrast to the film thickness, the aperture perimeter has a comparatively smaller influence on the spectral position of

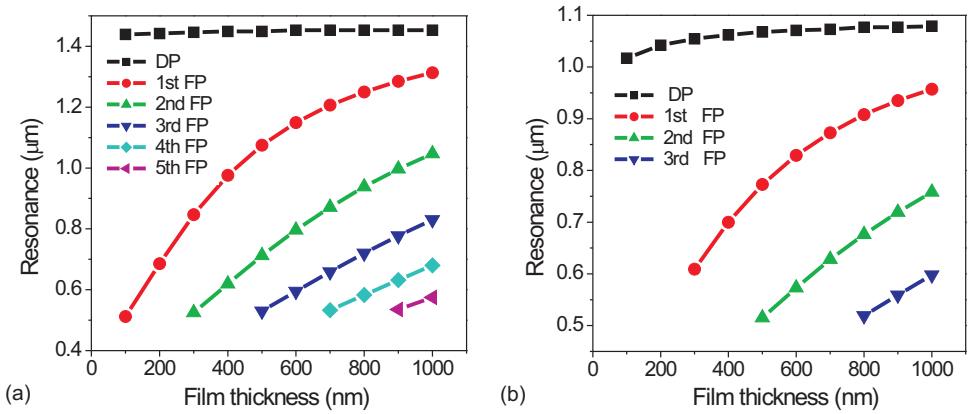

Figure 5.22: Dependence of resonances of bowtie slot antennas on the thickness of the metal. (a) Bowtie antennas in silver films. (b) Bowtie slot antennas in PEC films.

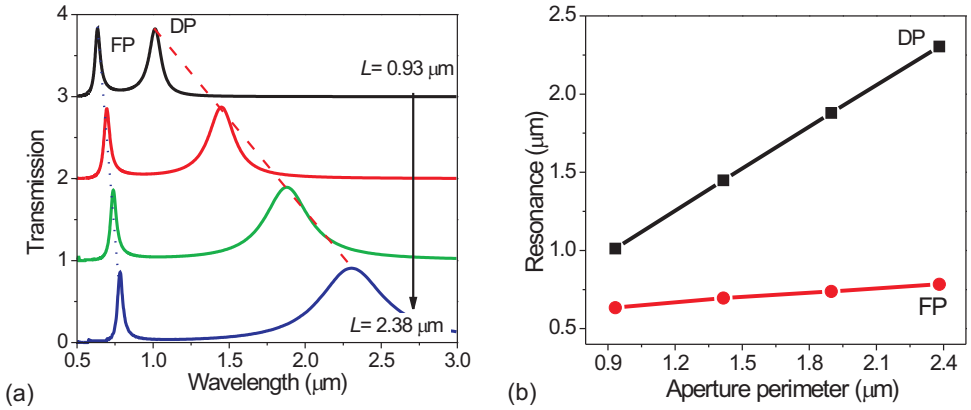

Figure 5.23: (a) Family of curves showing the calculated transmission spectra of bowtie slot antenna arrays in free-standing gold films for normal light incidence. The outline dimension, gap size, and angle of slot antennas are kept constant (L =1.41 μm, d = 40 nm, and θ = 90°, p_x = p_y = 450 nm), and the thickness of gold film t is varied from 150 nm to 300 nm in steps of 50 nm. The individual spectra are shifted upwards for clarity. (b) The wavelengths of dipole-like (DP) and Fabry-Pérot-like resonance (FP) resonances as function of the gold film thickness.

the FP resonance. The wavelength of the FP resonance shifts from 0.6 μm to 0.8 μm when the aperture perimeter is varied from 0.9 μm to 2.4 μm.

The field distributions in Fig. 5.20(c) and (d) indicate that the electric field distribution and current density distribution of the FP resonance are mainly film thickness dependent and nearly independent on the aperture perimeter. Therefore, the wavelength of the FP resonance is less influenced by the aperture perimeter.

5.5 General properties of slot antennas

Generally, both DP and FP resonances can be excited for slot antennas in an optically opaque metal film. The FP resonance appears at a shorter wavelength than the DP resonance. Current e-beam fabrication technology limits the realization of optical slot antennas in thin metal films to sizes of several tens nanometers, where only the DP resonance mode can be excited in the visible and near infrared range. Figure 5.24 shows the measured transmission spectra of bowtie slot antenna arrays in a 30-nm thin gold film with various aperture perimeters. The antenna arrays are fabricated on a quartz substrate. The fixed geometry of the antennas is $\theta = 90°$ and $d = 80$ nm. The aperture perimeter of the antennas are tuned from 1.46 μm to 3.6 μm in steps of about 500 nm by varying the outline dimensions of a and b. The periods of the arrays $p_x = p_y$ are increased from 600 nm to 1000 nm in steps of 100 nm, corresponding to the increased aperture perimeter. In the visible and near infrared spectra range, only the DP resonances are observed. The resonance wavelength is red shifted with the increased aperture perimeter. Figure 5.24(b) shows the resonance wavelength of the antenna as a function of aperture perimeter and a linear fit is obtained. The linear dependence of the resonance wavelength of the bowtie slot antenna on the aperture perimeter has therefore been proven experimentally.

This linear dependence of the wavelength of the DP resonance on the aperture perimeter is valid for the plasmonic resonances regardless of the type of nano-aperture. In rectangular apertures, for example, the resonance dependence on the so-called 'aspect ratio' [40, 90] is, in fact, a dependence on the aperture perimeter variation at the fixed length of the short axis. Figure 5.25 shows the measured transmission spectra of rectangular slot antenna arrays in a thin gold film with various length of the long axis. The antenna arrays are fabricated in a 30-nm-thick gold film on a quartz substrate. The short axis of the rectangular antenna is kept constant as $l_s = 130$ nm, and the aperture perimeter is varied from 1.06 μm to 2.26 μm in steps of 200 nm by tuning the length of the long axis l_l from 400 nm to 1000 nm. The

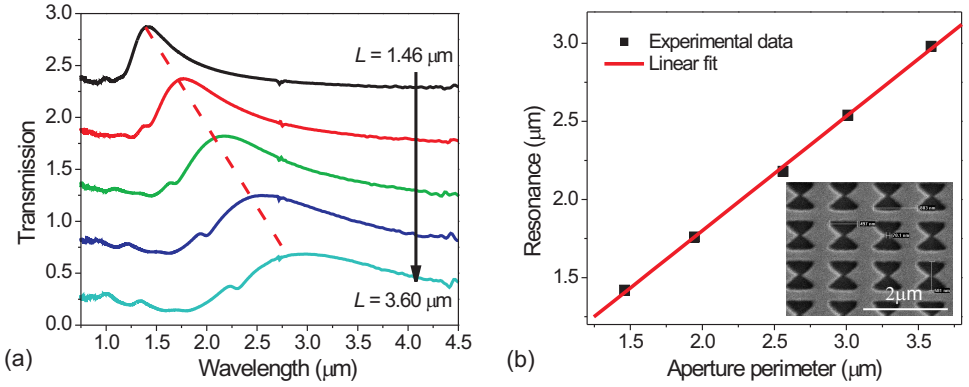

Figure 5.24: (a) Family of curves showing the measured transmission spectra of bowtie slot antennas in thin gold films deposited on quartz substrates for normal light incidence. The aperture perimeter of the antennas are tuned from 1.46 μm to 3.6 μm in steps of about 500 nm by varying the outline dimensions. The individual spectra are shifted upwards for clarity. (b) The resonance wavelength is a linear function of the aperture perimeter of bowtie slot antennas. The inset is an example SEM images of our sample.

period of the arrays p_x is fixed constant as 400 nm, and p_y is increased from 700 nm to 1300 nm in steps of 100 nm, corresponding to the increased length of the long axis. As shown in Fig. 5.25, the resonance wavelength of the rectangular antenna shifts linearly to a longer wavelength with the increased aperture perimeter as well.

Generally, sub-wavelength illumination and probing would be desirable in the visible spectral range. Considering that the wavelength of the FP resonance always appears at a shorter wavelength when compared to the DP resonance, most optical slot antennas have been designed to work near their FP resonances. Previously demonstrated applications of the bowtie slot antennas in NSOM and contact nano-lithography have utilized the FP resonances of the antennas [13, 14].

The transmission efficiency of sub-wavelength apertures is determined by their resonance. Variously shaped apertures may support resonances in different spectral ranges. When taking the resonance effect into account, it is clear that differently shaped apertures provide different transmission efficiency, even though they have the same open area [45, 46].

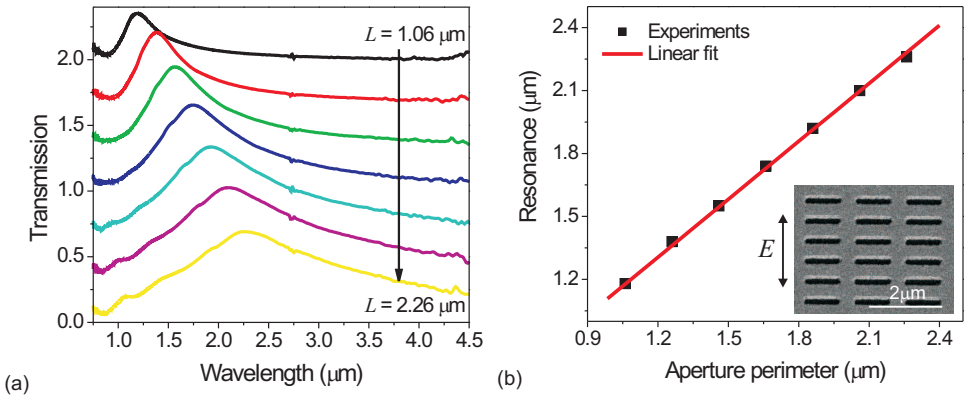

Figure 5.25: (a) Family of curves showing the measured transmission spectra of rectangular slot antennas in thin gold films deposited on quartz substrates for normal light incidence. The aperture perimeter is varied from 1.06 μm to 2.26 μm in steps of 200 nm by tuning the length of the long axis. The individual spectra are shifted upwards for clarity. (b) Aperture perimeter dependence of the resonance wavelengths of the rectangular slot antennas. The inset is an example SEM image of antenna arrays.

5.6 Field enhancement and confinement

For bowtie slot antennas, when the polarization of the incident light is perpendicular to the gap, the optical field is strongly confined in the gap area. Figure 5.26(a) shows the electric field distribution 20 nm above the antenna at the resonance. The calculation is performed using the FITD algorithm. The incident light field is mainly confined in the gap region. The gap size strongly influences the near field enhancement. As shown in Figure 5.26(b), the field enhancement factor is plotted as a function of gap size at the resonance wavelength. A small increase of the gap size results in a large decrease of the intensity of the localized electric field. Therefore, in most of our studies, we have fixed the gap size as constant at a reasonable value.

The field enhancement factor of optical antennas is very sensitive to the distance from antenna surface. As shown in the Fig. 5.27(a), the field enhancement factor decreases dramatically with increased distance from the antenna. Actually, this is not specific for optical antennas. As shown in Eq. 2.43, the electric field of radio frequency antennas varies as $1/r^3$ in the range of $0 < r \ll \lambda/2\pi$. This is called the near field regime of the antenna.

The field enhancement of optical antennas is also as strongly resonance dependent as the antennas at radio frequencies, where non-zero intrinsic reactance out of the resonance induces energy losses. Figure 5.27(b) shows the normalized electric near-

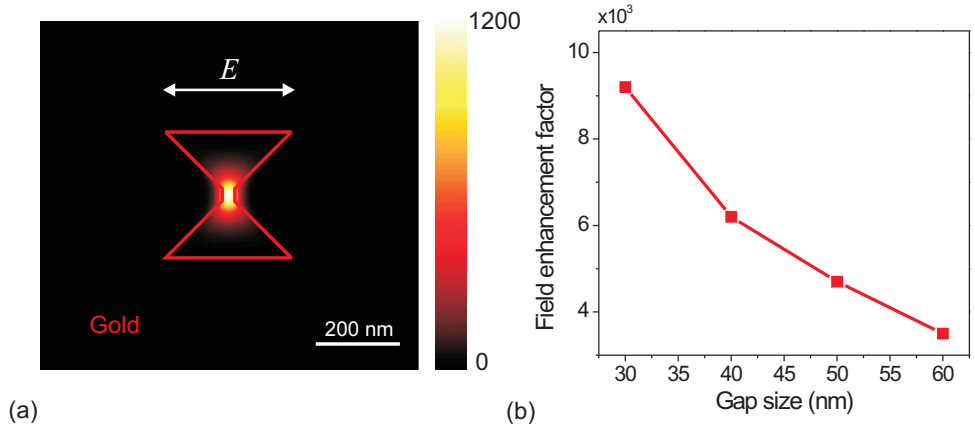

Figure 5.26: Gap size influence on the near field enhancement of bowtie slot antennas. (a) Electric field distribution of bowtie slot antennas at resonance. (b) Near field enhancement factor ($|E_{antenna}|^2/|E_{incident}|^2$)as a function of gap size.

field intensity of a bowtie slot antenna in various wavelengths. The corresponding transmission spectra of the antenna is given in the same figure for comparison. The field enhancement factor is proportional to the antenna transmission efficiency. In order to obtain maximum field enhancement, optical antennas have to be designed at the resonance frequency.

Optical antennas are also characterized by their field confinement. Figure 5.28 shows the near field spot size (spatial full width of half maximum amplitude) as a function of the distance from the antenna at the resonance frequency. The near field spot size increases with the increased distance from the antenna. This is consistent to the fact that the field enhancement factor decreases as the increased distance from the antenna, because the total energy is conserved. However, the near field spot size is independent of the resonance frequency. As shown in Fig. 5.28(b), at a fixed distance from the antenna surface the near field spot size is constant for all the frequencies and independent of the transmission efficiency. This can be understood from the field pattern of the antenna. The near field spot size is determined by the field pattern, which depends mainly on the current density distribution induced by the external light field.

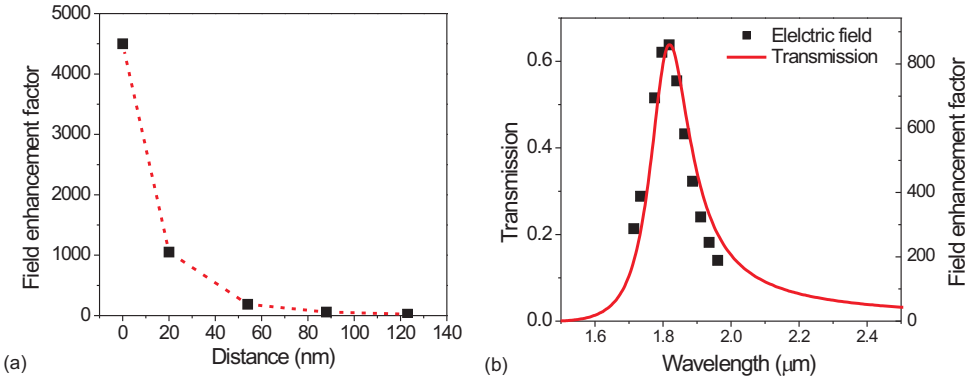

Figure 5.27: (a) Near field enhancement factor of the optical bowtie slot antenna calculated with the FITD algorithm as a function of distance from the antenna surface. The dashed line is a guide to the eye. (b) Near field enhancement factor of optical bowtie slot antennas and their corresponding transmission properties. The solid curve is the wavelength dependent transmission efficiency of the antenna. The solid squares are the field enhancement factor of the antenna for various wavelengths.

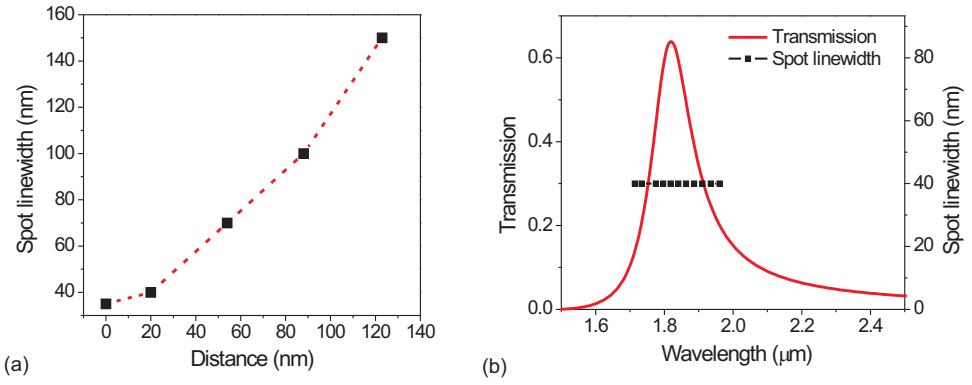

Figure 5.28: (a) Near field spot size as a function of the distance from the antenna. The dashed line is a guide for the eyes. (a) Near field spot size as a function of incident wavelength. The transmission spectrum of the antenna is given in the same figure for comparison.

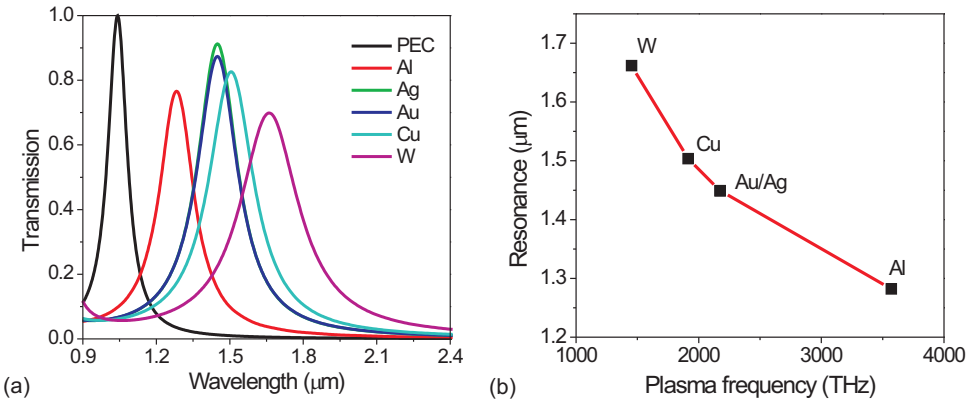

Figure 5.29: (a) Family of curves showing the transmission spectra of bowtie slot antennas in various metal films. The structure geometry is identical for each case as $d = 40$ nm, $\theta = 90°$, and $t = 30$ nm, $a = b = 300$ nm, and $p_x = p_y = 450$ nm. (b) The resonance wavelength dependence on the plasma frequencies of metals. The red line is a guide to the eye.

5.7 Metal dependence and RLC model of DP resonances

The dependence of the DP resonances on the metal has also been numerically studied for a fixed structure geometry. The plasma frequency and damping frequency of Table 3.1 are employed to describe the optical properties of various metals. Figure 5.29(a) shows the transmission spectra of bowtie slot antennas for various metals. The geometry of the antennas is identical for each metal with $d = 40$ nm, $\theta = 90°$, and $t = 30$ nm, $a = b = 300$ nm, and $p_x = p_y = 450$ nm. The resonance positions and amplitudes differ for the various metals. In order to study the metal influence on the antenna properties, these dependencies are discussed in terms of conductivity and skin depth, which are derived from the Drude model.

5.7.1 Resonance positions

As shown in Fig. 5.29(b), the resonance wavelength decreases inversely with the increasing plasma frequency of the metal. The physical origin of this effect can be understood by considering the effective path length of the induced current flow around the aperture edge due the skin depth of the metal in the visible and near-infrared regime. As shown in Chapter 2, the skin depth of the metal is

$$\delta = \lambda/2\pi\kappa, \tag{5.7}$$

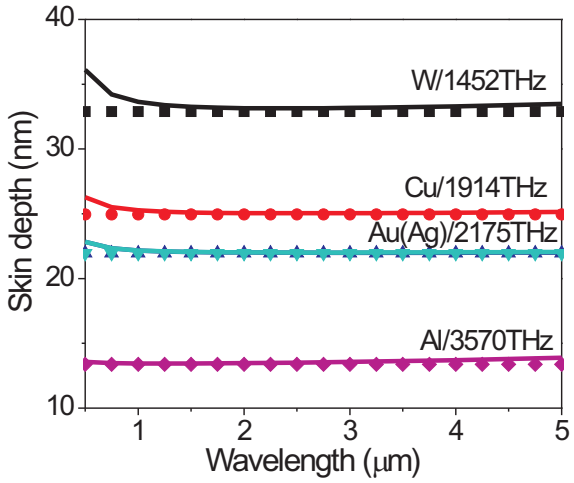

Figure 5.30: The skin depth of various metals in the visible and near infrared regime. The lines are derived from calculations based on the Eq. 5.7, and the scattered curves are from the approximation in Eq. 5.9. The plasma frequency of each metal in the Drude model is given with the corresponding curve.

where κ is absorption coefficient of the metal, and κ can be derived as

$$\kappa = \sqrt{-\frac{\epsilon'}{2} + \frac{1}{2}\sqrt{\epsilon'^2 + \epsilon''^2}}, \tag{5.8}$$

where ϵ' and ϵ'' are the real part and imaginary part of the dielectric function of the metal, respectively. The wavelength dependent skin depths of various metals are calculated and shown in Fig. 5.30 by solid lines. However, since the approximation $\gamma \ll \omega \ll \omega_p$ is only valid in the visible and near infrared regime, the skin depth can be expressed by the approximation

$$\delta = \frac{c}{\omega_p}, \tag{5.9}$$

where c is the velocity of the light in vacuum, and ω_p is the plasma frequency of the metal in the Drude model. The scattered curves in Fig. 5.30 show the skin depth of various metals as a function of wavelength by the approximation using Eq. 5.9. The approximation shows good agreement for each metal in the spectral range from 1 μm to 5 μm.

As mentioned in the previous section, the DP resonance wavelength of bowtie slot antennas shows a linear dependence on the aperture perimeter. The skin depth determines how localized the current distribution is to the inside edge of the aperture. Therefore the effective oscillation path length of the conduction electrons is skin depth dependent, as shown in Fig. 5.31(a). For a larger skin depth, for instance, the

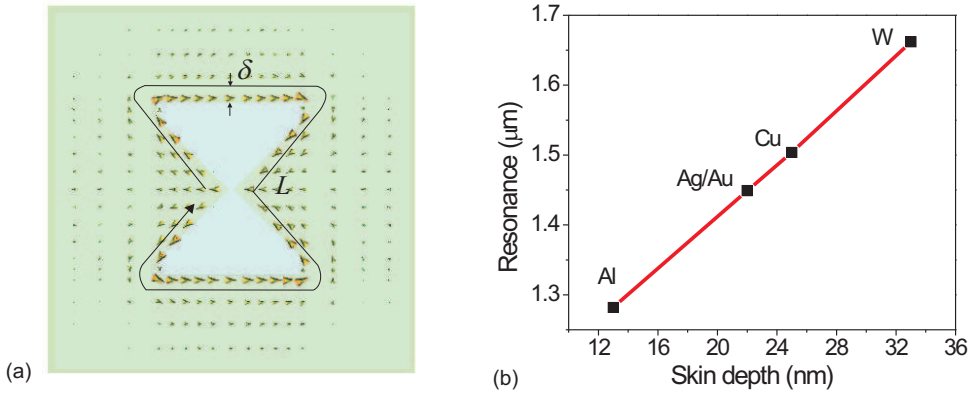

Figure 5.31: (a) Skin depth changes the effective oscillation path length of the conduction electrons. (b) The wavelength of the plasmonic resonance of bowtie slot antennas shows a linear dependence on the skin depth of the metals.

current density is less localized to the aperture edge, and the conduction electrons experience a longer effective path length. Figure 5.31(b) shows the wavelength of the DP resonance of bowtie slot antennas as a function of skin depth. The resonance wavelength increases nearly linearly with increasing skin depth due to this increase in the effective path length.

Intuitively, one can understand the resonance behavior of slot antennas in the following way. When the antennas are in perfectly conducting films, the resonance wavelength of the optical slot antennas can be described a function of electric path as $\lambda = a_1 L$ as in the radio frequency, where a_1 is the coefficient determined by the shape of the aperture and the thickness of the film, and L is the aperture perimeter. For real metals in the optical frequency range, however, the skin depth δ results in an additional length of the electrical path. Therefore, the resonance wavelength is approximately described by

$$\lambda = a_1(L + a_3\delta) = a_1 L + a_1 a_3 \delta, \tag{5.10}$$

where a_3 is a constant determined by the shape form of the slot antenna. With Eq. 5.3, one can obtain $a_2 = a_1 a_3 \delta$. Clearly, a_2 is more sensitive to the geometric and metal properties. This is consistent to the observations shown in Fig. 5.14 and Fig. 5.15.

5.7.2 Transmission efficiencies

The metal properties influence not only the resonance wavelength, but also the transmission efficiency. The field enhancement is associated with the resonance

amplitude of the antennas, therefore, it is important to investigate the physical origin of these properties. A model for these antennas is a distributed resistor-inductor-capacitor (RLC) circuit as shown in Fig. 5.32(a), in which the losses are due to both ohmic and radiative resistances. For a bowtie slot antenna, the ohmic resistance is determined by the resistivity and skin depth of the metal as well as by the geometry of the antenna. In the Drude model, electrical resistivity ρ is defined as the inverse of the conductivity σ as [18]

$$\rho(\omega) = \frac{1}{\sigma} = \frac{1 - i\omega\tau}{\sigma_0}, \tag{5.11}$$

where $\sigma_0 = \epsilon_0\omega_p^2\tau$ is the DC conductivity and $\tau = 1/\gamma$ is the Drude relaxation constant. The DC resistivity can be written as

$$\rho_0 = \frac{1}{\sigma_0} = \frac{\gamma}{\epsilon_0\omega_p^2}. \tag{5.12}$$

Considering that the geometry of bowtie slot antennas is identical for each metal, we ignore the aperture perimeter and film thickness influence and define the surface resistance R_s of antennas as

$$R_s = \frac{\rho_0}{\delta} = \frac{\gamma}{\delta\epsilon_0\omega_p^2}. \tag{5.13}$$

With the approximation in Eq. 5.9, the surface resistance of bowtie slot antennas for each metal can be estimated as $R_s = \gamma/(c\epsilon_0\omega_p)$. Figure 5.32(b) shows the resonance amplitude [or transmission efficiency that is extracted from Fig. 5.29(a)] as a function of surface resistance of metals normalized to that of the perfect electric conductor (PEC). In real metals, the resonance amplitude decreases with the increased surface resistance of metal as a function of $R_0/(R_0 + R_s)$. When compared with Eq. 2.58, one can find that R_0 corresponds to the radiative resistance of the antennas in a PEC film.

By comparing the transmission efficiencies of bowtie slot antennas in various metal films with that in a PEC film, one can see that optical antennas have exactly the same dependence behavior on the Ohmic losses of the metal. In principle, all the properties of antennas in the radio frequency can be transferred to optical frequencies by additionally taking the losses into account. It has been demonstrated experimentally and numerically that spontaneous emission can be enhanced by optical antennas [15, 91]. Recently, even redirection of the emission of single molecules with optical dipole antennas has been demonstrated [92, 93].

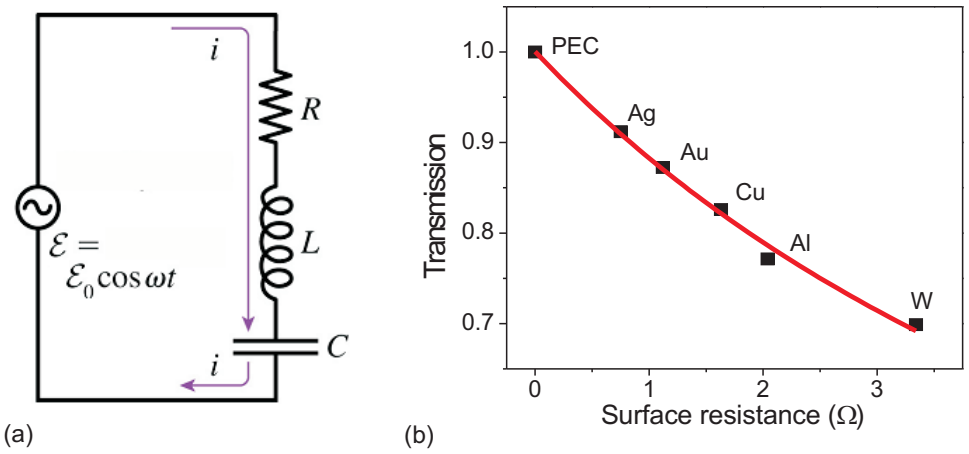

Figure 5.32: (a) The schematic diagram of a RLC circuit. (b) The resonance amplitude decreases with the increased metal surface resistance. The solid squares are extracted from Fig. 5.29(a), the solid line is fitted with $R_0/(R_0 + R_s)$, where R_0 is a fitting parameter.

5.8 Summary

In conclusion, we have studied the resonance dependence of bowtie slot antennas on geometry and metal properties. Two types of resonances, namely dipole-like resonances and Fabry-Pérot-like resonances, can be supported by slot antennas in the near infrared and visible spectral range, and they show a complementary behavior with respect to geometry dependence. Dipole-like resonances in the near-infrared regime, show a linear dependence on the aperture perimeter and nearly independence on the film thickness. In contrast, Fabry-Pérot-like resonances are mainly determined by the film thickness and appear at shorter wavelengths as compared to DP resonances. Depending on the wavelength range, one can effectively tune the antenna-operating wavelength by varying aperture perimeter or film thickness. The field enhancement and confinement are discussed as functions of the resonance wavelength and the distance from the antenna surface.

The influence of skin depth and resistivity of metals on the dipole-like resonance of slot antennas has been investigated. The resonance wavelength of the antenna shows a linear increase with increasing skin depth of the metal. The higher ohmic resistivity leads to a lower resonance amplitude and lower field enhancement at the resonance. This study can guide the design and optimization of slot antennas for specific resonance frequencies and characteristics. Such designs can be optimized by choice of geometries and materials and may therefore be directly used for a variety

of applications where concentration of light to sub-wavelength spots is desired.

6 Summary

In this thesis, the optical properties of two variants of metallic nano-structures, namely metallic split-ring resonators and bowtie slot antennas, have been investigated both experimentally and theoretically. Split-ring resonators are promising building blocks for negative permeability metamaterials. We have shown that in the optical regime, one can obtain higher resonance frequency SRRs by increasing the thickness of the metal experimentally. In order to interpret our observations, an equivalent cut-wire model based on the plasmonic explanation was proposed to analyze the resonance behavior of SRRs in the optical regime. It was shown that the resonance wavelength of an SRR can be quantitatively described by that of a cut-wire with a similar total wire length. Furthermore, the resonance behavior of double split-ring resonators has been investigated by combining the plasmonic model and hybridization concept. The interaction between localized surface plasmons of the constitute inner and outer ring of a DSRR was discussed based on the variation of the inner-ring geometry. The influence of the inner-ring orientation on DSRR resonances has been analyzed based on the plasmon hybridization of the inner and outer ring as well. From the simulated spectra and near field distributions, it appears that the orientation of the inner ring is not crucial for inducing the magnetic dipole in a DSRR at normal incidence.

The main part of this thesis deals with a detailed investigation of the optical properties of bowtie slot antennas. An optical bowtie slot antenna is composed of a bowtie shaped aperture in a thin metal film. Due to the sharp edge design and the small gap size, the light field can be confined strongly in the gap area when the electric field is perpendicular to the gap of the antenna. Considering that the optical properties of bowtie slot antennas were characterized in periodic arrays, we investigated the period influence on the resonances of individual antennas. When the periods of the antenna arrays are smaller than the resonance wavelengths of the individual antennas, the resonance properties of the antenna arrays are dominated by the local resonances of individual antennas. We have analyzed the coupling effect between the neighboring antennas in a slot antenna array based on Babinet's

principle and the plasmon hybridization method. When the periods of the antenna arrays are comparable with the resonance wavelengths of the individual antennas, surface plasmon excitation in periodically modulated metal surface will dominate the resonance spectra of the antenna arrays. The transmission of individual antennas is quenched by the surface plasmon excitation.

For individual antennas, the resonance properties are strongly influenced by their geometric and metal properties. Two types of resonances, namely dipole-like resonances and Fabry-Pérot-like resonances, can be supported by slot antennas in the near infrared and visible spectral range and they show a complementary behavior with respect to geometry dependence. Dipole-like resonances in the near-infrared regime, show a linear dependence on the aperture perimeter and nearly independence of the film thickness. In contrast, Fabry-Pérot-like resonances are mainly determined by the film thickness and appear at shorter wavelengths as compared to the dipole-like resonances. Depending on the wavelength range, one can effectively tune the antenna-operating wavelength by varying aperture perimeter or film thickness. The influence of skin depth and resistivity of metals on the dipole-like resonance of slot antennas has been investigated. The resonance wavelength shows a linear increase with increasing skin depth of the metal. The higher ohmic resistivity leads to a lower resonance amplitude and lower field enhancement at resonance.

The samples investigated in the thesis were fabricated by electron beam lithography and a subsequent dry etching step. In order to achieve a sub-100-nm resolution of the structures, thinner layer photoresist films have been applied during the lithography process. The transmission and reflection spectra of the samples were measured with a Fourier transform infrared spectrometer at the normal incidence.

Our studies indicate that metallic nanostructures can be regarded as resonant antennas. They have the same characteristics as those of antennas at radio frequencies when the skin depth and the surface resistance of the metal are taken into account. As an outlook, it would be interesting to address the following issues in the further studies:

- Fundamentally, the antenna concept can be applied in the interpretation of optical behavior of metallic nano-structures, such as enhanced transmission of subwavelength hole arrays, negative refractive index of metamaterials. This might provide insight for the design of optical metamaterials.

- The discussions of optical antennas within this work have been restricted to planar antenna arrays. However, the interaction between neighboring antennas

also introduces an influence on the resonance properties of the antennas. It was shown that in the radiative field region, the electrostatic dipole-dipole interaction model is no longer valid. It would be useful to investigate the coupling between the antennas in an antenna array and the optical properties of single antennas.

- Antennas are widely used to redirecting electromagnetic radiation at radio frequencies. Redirecting the light emission of single molecule or quantum dot with a single antenna or an antenna array such as a Yagi-Uda antenna might also be interesting. This also would involves the coupling between antennas and emitters, as well as non-ideality of antennas in the optical regime.

Bibliography

[1] G. Mie, *Beiträge zur Optik trüber Medien, speziell kolloidaler Metallösungen,* Ann. d. Phys. **25,** 377 (1908). 1, 2, 13, 14

[2] R. H. Ritchie, *Plasma losses by fast electrons in thin films,* Phys. Rev. **106,** 874 (1957). 1, 9

[3] H. Raether, *Surface plasmons on smooth and rough surfaces and on gratings* (Springer-Verlag, Berlin, 1988). 1, 9, 11, 12, 74

[4] U. Kreibig, M. Vollmer, *Optical properties of metal clusters* (Springer, Berlin, 1995). 1, 5, 7, 9, 14, 15, 16, 23, 47, 51, 54, 72

[5] W. Barnes, A. Dereux, and T. W. Ebbesen, *Surface plasmon subwavelength optics,* Nature **424,** 824 (2003). 1, 9

[6] R. K. Chang and T. Furtak, eds., *Surface enhanced raman scattering* (Plenum, New York, 1981). 1, 18

[7] K. Kneipp, Y. Wang, H. Kneipp, L. T. Perelman, I. Itzkan, R. R. Dasari, and M. S. Feld, *Single molecule detection using surface-enhanced Raman scattering (SERS),* Phys. Rev. Lett. **78,** 1667 (1997). 1, 18

[8] S. M. Nie and S. R. Emery, *Probing single molecules and single nanoparticles by surface-enhanced Raman scattering,* Science **275,** 1102 (1997). 1, 18

[9] J. Homola, S. S. Yee, and G. Gauglitz, *Surface plasmon resonance sensors: review,* Sensors Actuat. B **54,** 3 (1999). 1

[10] S. Linden, C. Enkrich, M. Wegener, J. F. Zhou, T. Koschny, and C.M. Soukoulis, *Magnetic response of metamaterials at 100 Terahertz,* Science **306,** 1351 (2004). 1, 44, 47, 49, 51, 74

[11] N. Fang, H. Lee, C. Sun, X. Zhang, *Sub-Diffraction-Limited optical imaging with a silver superlens,* Science **308,** 534 (2005). 1

[12] C. Enkrich, *Magnetic metamaterials for photonics,* Ph.D. thesis, Universität Karlsruhe (Shaker Verlag GmbH, Germany, 2006) 2, 44, 50

[13] L. Wang and X. Xu, *High transmission nanoscale bowtie-shaped aperture probe for near-field optical imaging,* Appl. Phys. Lett. **90,** 261105 (2007). 2, 30, 67, 68, 91

[14] L. Wang, S. M. Uppuluri, E. X. Jin, and X. Xu, *Nanolithography using high transmission nanoscale bowtie apertures,* Nano Lett. **6,** 361 (2006). 2, 30, 67, 68, 69, 91

[15] J. N. Farahani, D. W. Pohl, H. J. Eisler, and B. Hecht, *Single quantum dot coupled to a scanning optical antenna: a tunable superemitter,* Phys. Rev. Lett. **95,** 017402 (2005) 2, 30, 98

[16] W. L. Stutzman, A. A. Thiele, *Antenna theory and design* (John Wiley & Sons, New York, 1996). 3, 24, 31, 67, 72, 79

[17] P. Mühlschlegel, H. J. Eisler, O. J. F. Martin, B. Hecht, and D. W. Pohl, *Resonant optical antennas,* Science **308,** 1607 (2005). 3, 30, 31, 32, 67, 72

[18] C. Kittel, *Introduction to solid state physics* (John Wiley & Sons, New York, 1996). 5, 98

[19] P. B. Johnson and R. W. Christy, *Optical constants of the noble metals,* Phys. Rev. B **6,** 4370 (1972). 6, 7, 14

[20] H. Ehrenreich and H. R. Philipp, Phys. Rev. **128,** 1622 (1962). 7

[21] F. Bassani and G. P. Parravicini, *Electronic States and Optical Transitions in Solids* (Pergamon, London, 1975). 7

[22] E. A. Stern and R. A. Ferrell, *Surface plasma oscillations of a degenerate electron gas,* Phys. Rev. **120**, 130 (1960). 9

[23] D. Sarid, *Long-Range surface-plasma waves on very thin metal films,* Phys. Rev. Lett. **47,** 1927 (1981). 11

[24] J. J. Burke, G. I. Stegeman, and T. Tamir, *Surface-polariton-like waves guided by thin, lossy metal films,* Phys. Rev. B **33,** 5186 (1986). 11

[25] Fuzi Yang, J. R. Sambles, and G. W. Bradberry, *Long-range surface modes supported by thin films,* Phys. Rev. B **44,** 5855 (1991). 11

[26] A. Otto, *Excitation of nonradiative surface plasma waves in silver by method of frustrated total reflection,* Z. Phys. **216,** 398 (1968). 12

[27] E. Kretschmann, *Determination of optical constants of metals by excitation of surface plasmons,* Z. Phys. **241,** 313 (1971). 12

[28] C. F. Bohren and D. R. Hufman, *Absorption and scattering of light by small particles* (John Wiley & Sons, New York, 1983). 13, 14, 16, 18, 47

[29] P. M. Hansen, V. K. Bhatia, N. Harrit, and L. Oddershede, *Expanding the optical trapping range of gold nanoparticles,* Nano Lett. **5,** 1937 (2005). 14, 15

[30] U. Kreibig, P. Zacharias, *Surface plasma resonances in small spherical silver and gold particles,* Z. Phys. **231,** 128 (1970). 14

[31] U. Kreibig, B. Schmitz, H. D. Breuer, *Separation of plasmon-polariton modes of small metal particles,* Phys. Rev. B **36,** 5027 (1987). 14

[32] J. D. Jackson, *Classical electrodynamics* (Wiely, New York 1975). 15, 78

[33] J. Gersten and A. Nitzan, *Spectroscopic properties of molecules interacting with small dielectric particles,* J. Chem. Phys. **75,** 1139 (1981). 18

[34] G. Raschke, S. Kowarik, T. Franzl, C. Sönnichsen, T. A. Klar, and J. Feldmann, A. Nichtl and K. Kürzinger, *Biomolecular recognition based on single gold nanoparticle light scattering,* Nano Lett. **3,** 935 (2003). 18

[35] T. W. Ebbesen, H. J. Lezec, H. F. Ghaemi, T. Thio, and P. A. Wolff, *Extraordinary optical transmission through sub-wavelength hole arrays,* Nature (London) **391,** 667 (1998). 19, 20, 74

[36] K.J. Klein Koerkamp, S. Enoch, F.B. Segerink, N.F. van Hulst, L. Kuipers, *Strong influence of hole shape on extraordinary transmission through periodic arrays,* Phys. Rev. Lett. **92,** 183901 (2004). 19, 21

[37] X. Shi, L. Hesselink, R. L. Thornton, *Ultrahigh light transmission through a C-shaped nanoaperture,* Opt. Lett. **28,** 1320 (2003). 19, 21

[38] T. Matsui, A. Agrawal, A. Nahata, and Z. V. Vardeny, *Transmission resonances through aperiodic arrays of subwavelength apertures,* Nature **446,** 517 (2007). 19, 20

[39] H. F. Ghaemi, T. Thio, D. E. Grupp, T. W. Ebbesen, and H. J. Lezec, *Surface plasmons enhance optical transmission through subwavelength holes,* Phys. Rev. B **58** 6779 (1998). 19

[40] K. L. van der Molen, K. J. Klein Koerkamp, S. Enoch, F. B. Segerink, N. F. van Hulst, and L. Kuipers, *Role of shape and localized resonances in extraordinary transmission through periodic arrays of subwavelength holes: Experiment and theory,* Phys. Rev. B **72,** 045421 (2005). 19, 20, 90

[41] A. Degiron , T. W. Ebbesen, *The role of localized surface plasmon modes in the enhanced transmission of periodic subwavelength apertures,* J. Opt. A: Pure Appl. Opt. **7,** S90 (2005). 20, 21

[42] Z. C. Ruan, M. Qiu, *Enhanced transmission through periodic arrays of subwavelength holes: The role of localized waveguide resonances,* Phys. Rev. Lett. **96,** 233901 (2006). 20

[43] C. Rockstuhl, F. Lederer, T. Zentgraf, and H. Giessen, *Enhanced transmission of periodic, quasi-periodic, and random nanoaperture arrays,* Appl. Phys. Lett. **91,** 151109 (2007). 20

[44] E. X. Jin and X. Xu, *Finit-Difference Time-Domain studies on optical transmission through planar nano-apertures in a Metal film,* Jpn. J. Appl. Phys. **43,** 407 (2004). 21, 67, 68, 87

[45] J. A. Matteo, D. P. Fromm, Y. Yuen, P. J. Schuck, W. E. Moerner, and L. Hesselink, *Spectral analysis of strongly enhanced visible light transmission through single C-shaped nanoapertures,* Appl. Phys. Lett. **85,** 648 (2004). 21, 22, 91

[46] E. X. Jin and X. Xu, *Plasmonic effects in near-filed optical transmission enhancement through a single bowtie-shaped aperture,* Appl. Phys. B. **84,** 3 (2006). 21, 68, 69, 91

[47] K. B. Crozier, A. Sundaramurthy, G. S. Kino, and C. F. Quate, *Optical antennas: Resonators for local field enhancement,* J. Appl. Phys. **94,** 4632 (2003). 23, 30, 32, 67, 72

[48] D. P. Fromm, A. Sundaramurthy, P. J. Schuck, G. Kino, and W. E. Moerner, *Gap-Dependent optical coupling of single "bowtie" nanoantennas resonant in the visible,* Nano Lett. **4,** 957 (2004). 30

[49] L. Novotny, *Effective wavelength scaling for optical antennas,* Phys. Rev. Lett. **98,** 266802 (2007). 30, 32, 33, 72, 85

[50] P. J. Schuck, D. P. Fromm, A. Sundaramurthy, G. S. Kino, and W. E. Moerner, *Improving the mismatch between light and nanoscale objects with gold bowtie nanoantennas,* Phys. Rev. Lett. **94,** 017402 (2005). 30

[51] 1. R. D. Grober, R. J. Schoelkopf, and D. E. Prober, *Optical antenna: Towards a unity efficiency near-field optical probe,* Appl. Phys. Lett. **70,** 1354 (1997). 31, 67

[52] K. Sendur and W. Challener, *Near-field radiation of bow-tie antennas and apertures at optical frequencies,* J. Microsc. **210,** 279 (2002). 31, 67

[53] E. Cubukcu, E. A. Kort, K. B. Crozier, and F. Capasso, *Plasmonic laser antenna,* Appl. Phys. Lett. **89,** 093120 (2006) 32, 72

[54] Bharat Bhushan (ed.), *Springer handbook of nanotechnology* (Springer-Verlag, Berlin, 2004). 35

[55] D. F. Kyser, N. S. Viswanathan, *Monte Carlo simulation of spatial distributed beams in electron-beam lithography,* J. Vac. Sci. Technol. **12,** 1305 (1975). 41

[56] M. Rooks, N. Belic, E. Kratschmer, and R. Viswanathan, *Experimental optimization of the electron-beam proximity effect forward scattering parameter,* J. Vac. Sci. Technol. B **23,** 2769 (2005). 41

[57] CST GmbH, Germany. www.cst.de. 43

[58] C. Enkrich, F. Pérez-Willard, D. Gerthsen, J. F. Zhou, C.M. Soukoulis, M. Wegener, and S. Linden, *Focused-Ion-Beam nanofabrication of near-infrared magnetic metamaterials*, Adv. Mater. **17,** 2547 (2005). 44, 50

[59] M. A. Ordal, L. L. Long, R. J. Bell, S. E. Bell, R. R. Bell, R. W. Alexander, Jr., and C. A. Ward, *Optical properties of the metals Al, Co, Cu, Au, Fe, Pb, Ni, Pd, Pt, Ag, Ti, and W in the infrared and far infrared,* Appl. Opt. **22,** 1099 (1983). 45

[60] D.R. Smith, W. J. Padilla, D. C. Vier, S. C. Nemat-Nasser, and S. Schultz, *Composite medium with simultaneously negative permeability and permittivity,* Phys. Rev. Lett. **84,** 4184 (2000). 47, 48, 49, 58

[61] D. J. Griffiths, *Introduction to electrodynamics* (3rd Ed. Benjamin Cummings, San Francisco, 2008). 47

[62] V. G. Veselago, *The electrodynamics of substances with simultaneously negative values of ϵ and μ,* Sov. Phys. Usp. **10,** 509 (1968). 47

[63] J. B. Pendry, *Negative refraction makes a perfect lens,* Phys. Rev. Lett. **85,** 3966 (2000). 47

[64] J. B. Pendry, A. J. Holden, W. J. Stewart, and I. Youngs, *Extremely low frequency plasmons in metallic mesostructures,* Phys. Rev. Lett.**76,** 4773 (1996). 47, 48

[65] B. Pendry, A. J. Holden, D. J. Robbins, and W. J. Stewart, *Magnetism from conductors and enhanced nonlinear phenomena,* IEEE Trans. Microw. Theory Tech. **47,** 2075 (1999). 47, 48

[66] R.A. Shelby, D.R. Smith, and S. Schultz, *Experimental verification of a negative index of refraction,* Science 292, **77,** (2001). 49

[67] T. J. Yen, W. J. Padilla, N. Fang, D. C. Vier, D. R. Smith, J. B. Pendry, D.N. Basov, and X. Zhang, *Terahertz magnetic response from artificial materials,* Science **303,** 1494 (2004). 49

[68] J. F. Zhou, Th. Koschny, M. Kafesaki, E.N. Economou, J. B. Pendry, and C.M. Soukoulis, *Saturation of the magnetic response of split-ring resonators at optical frequencies,* Phys. Rev. Lett. **95,** 223902 (2005). 49, 50

[69] A. Ishikawa, T. Tanaka, and S. Kawata, *Negative magnetic permeability in the visible light region,* Phys. Rev. Lett. **95,** 237401 (2005). 49

[70] N. Katsarakis, T. Koschny, M. Kafesaki, E.N. Economou, and C.M. Soukoulis, *Electric coupling to the magnetic resonance of split ring resonators,* Appl. Phys. Lett. **84,** 2943 (2004). 49

[71] C. Rockstuhl, T. Zentgraf, H. Guo, N. Liu, C. Etrich, I. Loa, K. Syassen, J. Kuhl, F. Lederer, and H. Giessen, *Resonances of split-ring resonator metamaterials in the near infrared,* Appl. Phys. B **84,** 219 (2006). 50

[72] C. Rockstuhl, F. Lederer, C. Etrich, T. Zentgraf, J. Kuhl, and H. Giessen, *On the reinterpretation of resonances in split-ring-resonators at normal incidence,* Opt. Express **14,** 8827 (2006). 54

[73] A. Christ, *Optical properties of metallic photonic crystal structures,* Ph.D. thesis, Philipps-Universität Marburg (2005). 54

[74] M. Kafesaki, T. Koschny, R. S. Penciu, T. F. Gundogdu, E. N. Economou, and C. M. Soukoulis, *Left-handed metamaterials: detailed numerical studies of the transmission properties,* J. Opt. A **7,** S12 (2005). 58

[75] N. Liu, H. C. Guo, L. Fu, H. Schweizer, S. Kaiser, and H. Giessen, *Electromagnetic resonances in single and double split-ring resonator metamaterials in the near infrared,* phys. stat. sol. (b) **244,** 1251 (2007). 58

[76] E. Prodan, C. Radloff, N. J. Halas, P. Nordlander, *A hybridization model for the plasmon response of complex nanostructures,* Science **302,** 419 (2003). 58

[77] N. Liu, H. C. Guo, L. Fu, H. Schweizer, S. Kaiser, and H. Giessen, *Plasmon hybridization in stacked cut-wire metamaterials,* Adv. Mat. **19,** 3628 (2007). 58

[78] H. Wang, D. W. Brandl, F. Le, P. Nordlander, and N. J. Halas, *Nanorice: A hybrid plasmonic nanostructure,* Nano Lett. **6,** 827 (2006). 58

[79] M. Born and E. Wolf, *Principles of optics* (Cambridge University Press, 2002). 67, 75, 87

[80] L. Wang and X. Xu, *Spectral resonance of nanoscale bowtie apertures in visible wavelength,* App. Phys. A **89,** 293 (2007). 68

[81] B.A. Munk, *Frequency selective surfaces: Theory and Design* (John Wiley & Sons, New York, 2000). 71

[82] S. H. Chang, S. K. Gray, and G. C. Schatz, *Surface plasmon generation and light transmission by isolated nanoholes and arrays of nanoholes in thin metal films,* Opt. Express **13,** 3150 (2005). 74

[83] T. Zentgraf, T. P. Meyrath, A. Seidel, S. Kaiser, H. Giessen, C. Rockstuhl, F. Lederer, *Babinet's principle for optical frequency metamaterials and nanoantennas,* Phys. Rev. B **76,** 033407 (2007). 75

[84] P. Nordlander, C. Oubre, E. Prodan, K. Li, and M. I. Stockman, *Plasmon hybridization in nanoparticle dimers,* Nano Lett. **4,** 899 (2004). 75

[85] P. K. Jain, S. Eustis, and M. A. El-Sayed, *Plasmon coupling in nanorod assemblies: Optical absorption, discrete dipole approximation simulation, and exciton-coupling model,* J. Phys. Chem. B, **110,** 18243 (2006). 75, 78

[86] J. A. Porto, F. J. Garcia-Vidal, and J. B. Pendry, *Transmission resonances on metallic gratings with very narrow slits,* Phys. Rev. Lett. **83,** 2845 (1999). 87

[87] S. Astilean, Ph. Lalanne, and M. Palamaru, *Light transmission through metallic channels much smaller than the wavelength,* Opt. Commun. **175,** 265 (2000). 87

[88] J. Lindberg, K. Lindfors, T. Setälä, and A. T. Friberg, *Spectral analysis of resonant transmission of light through a single sub-wavelength slit,* Opt. Express **12,** 623 (2004). 87

[89] L. Sun and L. Hesselink, *Low-loss subwavelength metal C-aperture waveguide,* Opt. Lett. **31,** 3606 (2006). 87

[90] F. J. Garcia-Vidal, E. Moreno, J. A. Porto, and L. Martin-Moreno, *Transmission of light through a single rectangular hole,* Phys. Rev. Lett. **95,** 103901 (2005). 90

[91] L. Rogobete, F. Kaminski, M. Agio, and V. Sandoghdar, *Design of plasmonic nanoantennae for enhancing spontaneous emission,* Opt. Lett. **32,** 1623 (2007) 98

[92] T. H. Taminiau, F. B. Segerink, R. J. Moerland, L. Kuipers, and N. F. Hulst, *Near-field driving of a optical monopole antenna,* J. Opt. A: Pure Appl. Opt. **9,** S315 (2007). 98

[93] T. H. Taminiau, F. D. Stefani, F. B. Segerink and N. F. van Hulst, *Optical antennas direct single-molecule emission,* Nature Photonics **2,** 234 (2008). 98

List of Figures

Acknowledgements

I would like to thank all the people who helped me in research and life during my Ph.D studies in Germany. Many thanks go to:

- Prof. Dr. Harald Giessen for supervising me and support my research over five years, for guiding me into different topics, for the freedom he gave me during my research work, and for the stimulating scientific discussions.
- Prof. Dr. Martin Dressel for kindly concerning to be my second Gutachter.
- Dr. Todd Meyrath, Dr. Liwei Fu, Dr. Thomas Zentgraf, Na Liu, and Prof. Heiz Schweizer, and Dr. Albert Heberle for fruitful discussions.
- Stefan Kaiser from 1st Physics Institute for helping with FTIR measurements.
- Mawuli Ametowobla and Fran Renate Zapf-Gottwick from Institute of Physical Electronics for helping with SEM measurements.
- Frau Hedi Gräbeldinger, Frau Monika Ubl, Herr Emmerich Frank, and Herr Erich Kohler for technical support in the MSL.
- Frau Gabi Feurle, Dr. Christine von Rekowski, Dr. Wolf Wölfel, and Frau Christa Nagel for their support in administrative stuffs.
- Herr Kamella and colleagues in the mechanic workshop, Herr Quack in the glass workshop, and Herr Kern and colleagues in the electronic workshop for their technique support.
- my colleagues in 4th Physics Institute in Stuttgart (in alphabetical order): Ralf Ameling, Thomas Baluktsian, Christina Bauer, Thomas Bublat, Zhaolu Diao, Tolga Ergin, Michael Geiselmann, Dr. Albert Gröning, Cornelius Grossmann, Felix Hoos, Dr. Michael Jetter, Georg Kobiela, Daniel Kunert, Sai Li, Dr. Markus Lippitz, Regina Orzekowsky, Markus Pfeiffer, Sebastian Pricking, Dr. Robert Rossbach, Andreas Seidel, Dr. Tilman Höner zu Siederdissen, Richard

Taubert, Tobias Utikal, Marius Vieweg, Thomas Weiss, Christian Wolpert, for the friendly working atmosphere and nice help in my research and daily life.

- my colleagues in the former group in Bonn: Dr. Dietmar Nau, André Radke, Anja Schönhardt,Dr. Jörn Teipel, Dr. Diana Türke, Dr. Xiulun Yang, Dr. Rui Zhang, and Dr. Xinping Zhang for the good starting time in my Ph.D study.

- last, but not least, my wife Yan Zhou and my parents for always being my side and supporting me.

Resume

03/24/1978	Born in Cangzhou, Hebei, China
09/1984 - 08/1990	Primary school in Nanwangzhuang, Hebei, China
09/1990 - 08/1993	Middle school in Qiqiao, Hebei, China
09/1993 - 08/1996	High school in Botou, Hebei, China
09/1996 - 08/2000	Bachelor in Science, Physics Department, Nankai Univsersity, Tianjin, China
09/2000 - 08/2003	Master in Science, Physics Department, Peking University, Beijing, China
09/2003 - 8/2005	Ph.D Student, Institute of Applied Physics, University of Bonn, Bonn, Germany
09/2005 - 09/2008	Ph.D student, 4th Physics Institute, University of Stuttgart, Germany